Flow Simulation and Sensitivity Analysis of Paleokarst Carbonate Reservoirs

Master Thesis

Mustaqim Balyesiima

Department of Earth Science
University of Bergen
09 June 2020

Abstract

A paleokarst reservoir is a product of deactivation and degradation of karst by collapse and infill during burial. Paleokarst reservoirs contribute to about 30% of the world's carbonate oil and gas reserves. However, a multiscale of heterogeneities that exist in paleokarst reservoir influence fluid flow behaviour resulting into production and forecasting challenges. This thesis presents a workflow to address these challenges by studying fluid flow sensitivities using synthetic paleokarst models with varying geometries, petrophysical properties, and well patterns using synthetic paleokarst models. Upscaling is also done to understand the extent of preservation of flow properties, and production forecast. Finally, the possibility of using 4D seismic (Time-lapse) paleokarst models to map changes in dynamic properties (saturation, and pressure) of the reservoir through its production lifetime is also tested.

The test simulations were performed using two generic fine scale base models measuring 614x100x30 m^3 and with cells of 2x2x2 m^3. The base models represent an infilled cave system but are different from each other by the number of interconnected branches, loops of varying sizes, and complexity. Passage-diameters for both cases range from 2-18 m. On flow simulation, non-cave facies of permeability less or equal to 0.1 mD produced a flow pattern mainly through the cave geometry resulting into a relatively early water breakthrough. When the non-cave facies permeability is increased to 20 mD or more, the entire reservoir pay zone is uniformly swept with no preferential flow along the paleokarst structure. But non-cave facies of permeability as low as 5 mD had a better recovery comparable to the one from the cave region. In instances where the cave sections consisted of a combination of sand infill at the base and collapse breccia at the top inside the collapsed cave system, the recovery factor was observed to be high in less permeable sand infill than in the collapse breccia. This is only in section of 10-18 m diameter, but in cave sections with a diameter less than 10 m, the sweep is uniform, and the flow pattern is non-selective.

Static and dynamic properties from flow simulation, and paleokarst rock physics models were used to produce synthetic seismic models at different production time-steps (4D seismic). Using the 4D seismic models, mapping of changes in saturation, and pressure changes in cave structures as a function of change in amplitude. Cave structures and the fluid flow path were captured when the fine grid paleokarst models were upscaled to 6 m, and 10 m grid scale, but further upscaling to 15 m, and 30 m grid smoothened most of the cave structures and the original fluid flow path. Future work should involve extending the results from this thesis and integrating them with real life paleokarst reservoir data for validation and to test if they can also be applied to other fields like geotechnical engineering, karst hydrogeology, geothermal energy, and to forecast geohazards in areas with karst carbonates.

Acknowledgement

The Master thesis is a partial fulfilment of the requirement of a master's degree in Earth Science at the Department of Earth Science (University of Bergen). The work in this thesis involves a collaboration with Norwegian Research Centre AS (NORCE) under the FOPAK research group ("Forecasting of architecture, seismic characteristics and flow behaviour in paleokarst reservoirs) funded by the Research Council of Norway under contract 267634 (PETROMAKS 2).

The work in this master thesis was supervised by Isabelle Lecomte (main supervisor) from the Department of Earth Science at University of Bergen (UiB), Øystein Pettersen (co-supervisor) and Jan Tveranger (co-supervisor) from the Norwegian Research Centre (NORCE).

With utmost gratitude I would like to thank my main supervisor Isabelle Lecomte for offering help and advice to fit in a new environment when I had just started my master's degree, guidance with synthetic seismic modelling, and for keeping track of my progress through the weekly status meetings that we held. Øystein Pettersen offered excellent guidance and discussions with reservoir simulation using Eclipse and motivated my interest in reservoir engineering. Jan Tveranger was very pivotal in guiding me with carbonates and karst geology, reservoir modelling, and upscaling using RMS software. More thanks to my all supervisors for providing guidance in writing two abstracts that got accepted for poster, and oral presentation at the 34th Nordic Geological Forum, and the 82nd EAGE Annual conference (Reservoir Simulation session) respectively, and suggesting that I publish of a full paper of my thesis in a journal.

I further extend my thanks to NORCE through the FOPAK project for sponsoring me to field courses in karst hydrogeology (Mo i Rana, Norway), and applied reservoir geophysics (Pyrenees, Spain), for sending me to attend the NGF Winter Conference (Bergen, 2019), to present a poster at the 34th Nordic Geological Forum winter meeting in Oslo, and to publish a full paper of my thesis in a journal after my graduation.

Many thanks to DT EP Consulting AG for offering a study grant to cover my entire master's degree period.

Finally, special gratitude to ROXAR Emerson, NORSAR Innovation AS, The Open Porous Media initiative and Schlumberger for providing academic licenses for RMS, SeisRox, ResInsight and Eclipse, respectively.

Table of Contents

1 INTRODUCTION 1
  1.1 Motivation 1
  1.2 Research objective 3
  1.3 Carbonates 5
    1.3.1 Formation and composition 5
    1.3.2 Limestone 5
    1.3.3 Dolomite 6
    1.3.4 Marble 6
    1.3.5 Evaporites 7
    1.3.7 Classification of carbonate rocks 9
  1.4 Paleokarst 11
    1.4.1 Burial and diagenesis of paleokarst deposits 15
    1.4.2 Major paleokarst reservoirs in the world 20
    1.4.3 Production and engineering challenges of paleokarst reservoirs 22
  1.5 Reservoir modelling and Simulation of Paleokarst reservoirs 23
    1.5.1 Flow Simulation Equations 24
    1.5.3 Upscaling of paleokarst reservoir properties 25
    1.6 Previous work 28
2 METHODOLOGY 29
  2.1 Workflow 29
  2.2 Grid Construction 30
    2.2.1 2D Paleokarst skeleton 30
  2.3 Geomodelling 31
    2.3.1 Construction of 3D paleokarst geomodels 31
    2.3.2 Petrophysical and rock model 34
    2.3.3 Upscaling strategy for fluid flow simulation 35
    2.3.4 Flow based simulation using Eclipse 35
    2.3.5 Defining Regions of Interest 37
    2.3.6 Reducing simulation run time 38
  2.4 NOTEPAD++ 40
  2.5 Visualizations of simulation outputs 40
  2.6 Fracture Modelling 40
  2.7 4D seismic modelling 43
3 RESULTS AND DISCUSION 44

- 3.1 Sensitivities of Paleokarst 44
  - 3.1.1 Sensitivity to varying cave geometries 44
  - 3.1.2 Sensitivity to varying cave sizes 46
  - 3.1.3 Sensitivity to increasing matrix permeability 48
  - 3.1.4 Sensitivity to cave-matrix flux invasion 59
  - 3.1.5 Sensitivity to inflow and outflow geometry 63
  - 3.1.6 Sensitivity to varying infill composition 64
  - 3.1.7 Sensitivity to well patterns 68
- 3.2 Upscaling 76
  - 3.2.1 Introduction 76
  - 3.2.3 Upscaling of generic paleokarst reservoir models 77
- 3.3 4D Seismic 85
  - 3.3.1 Rock physics modelling 85
  - 3.3.2 Seismic modelling 90
  - 3.3.3 Seismic modelling of the simple generic paleokarst model 92
  - 3.3 4 4D Seismic as a function of depth 97
- 3.4 Fracture modelling 100
  - 3.4.1 Modelling scenario 1: fracture sensitivity to fluid flow patterns in a complex karst system 101
  - 3.4.2 Modelling scenario 2: fracture sensitivity to fluid flow patterns in a complex karst system 102

4 CONCLUSIONS 104
- 4.1 Main Conclusions 104
- 4.2 Recommendations for further work 106

5 REFERENCES 107

6 APPENDICES 112
- Appendix 1 112
- Appendix 2 113
- Appendix 3 114

List of Figures

Figure 1.2-1: *Workflow used in the thesis for flow simulation and seismic modelling. 4*
Figure 1.3.1: *River Glomåga cuts through marble to form the Marmorslottet castles in Mo I Rana (Photo credit: Mustaqim Balyesiima). 7*
Figure 1.3-2: The different diagenetic realms of carbonate rocks (Choquette & James, 1987). 8
Figure 1.3-3*: Folk's and Dunham's classification of carbonate rocks, adapted from (R. Folk & Dunham, 1962). 10*
Figure 1.3-4*: Classification of porosity types (C. Moore, 2001)...10*
Figure 1.4-1*: Engineering classification of karst (Waltham & Fookes, 2005)......................12*
Figure 1.4.2*: Types of paleokarst (Klimchouk, 1996)...13*
Figure 1.4-3*: Classification of near surface cave geometries and passages (from Loucks,1999)...14*
Figure 1.4-4*: Paleocave collapse and compaction stages (R. G. Loucks, 1999)...................16*
Figure 1.4-5: *Description of facies in a buried karst (R. G. Loucks, 1999). 17*
Figure 1.4-6*: Classification of cave infills (Loucks,1999)..18*
Figure 1.5-1*: Integration from different disciplines to form a reservoir model (Haldorsen & Damsleth, 1993)...23*
Figure 2.1-1*: Workflow for methodology used to construct of generic paleokarst models....29*
Figure 2.2-1: *2D cave geometry (orange) constructed in excel based on conceptual models. 30*
Figure 2.3-1*: a comparison of cave geometries (a) an ideal circular cave geometry (orange) a uniform diameter perfectly inscribed by the grid (blue) (b) a conceptual model of what a real cave may look like (orange) inscribed by a regular grid (blue)......................................31*
Figure 2.3-2: *a comparison of cave geometries (a) complex generic karst model (b) simple generic karst model..33*
Figure 2.3-3*: Comparison between CPR linear Solver (Magenta) and the default Eclipse linear solver (Blue) based on number of Newton iterations achieved during flow simulation of a complex generic paleokarst model...38*
Figure 2.3-4*: Comparison between CPR linear Solver (Magenta) and the default Eclipse linear solver (Blue) based on number of Newton iterations achieved per time-step during flow simulation of the simple generic paleokarst model...39*
Figure 2.6-1: *Fractures sets in the central layer generated stochastically. The green lines are the vertical fracture sets (Frac_vertical) while the red lines (Frac_horizontal) are mainly horizontal fractures...41*
Figure 3.1-1: *Oil saturation plots of paleokarst models with varying geometries displaying (a) flow patterns and waterflood front (blue) in the central layer of a complex cave geometry and the (b) corresponding 3D planar view (c) flow patterns and waterflood front (blue) in the central layer of the simple cave geometry, and the (d) corresponding 3D planar view....45*
Figure 3.1-2*: Streamline simulations (in pink) on cave models displaying (a) flow patterns across the entire complex cave geometry (b) flow patterns across the entire simple cave geometry..46*
Figure 3.1-3*: Oil saturation plots (left) and saturation plots (right) showing (a) 6 metre cave (b) 10 metre cave (c) 18 metre cave..47*
Figure 3.1-4*: A horizontal section of the complex paleokarst flow simulation model showing oil saturation at 0.1 mD matrix permeability of the (a) top-most layer of the cave system (b) central layer of the cave system (c) bottom-most layer of the cave system. 49*

Figure 3.1-5: *A horizontal section of the complex paleokarst flow simulation model showing oil saturation at 10 mD matrix permeability of the (a) top-most layer of the cave system (b) central layer of the cave system (c) bottom-most layer of the cave system. 50*
Figure 3.1-6*: A horizontal section of the simple paleokarst flow simulation model showing oil saturation at 10 mD matrix permeability of the (a) top-most layer of the cave system (b) central layer of the cave system (c) bottom-most layer of the cave system. 50*
Figure 3.1-7: *A horizontal section of the complex paleokarst flow simulation model showing oil saturation at 20 mD matrix permeability of the (a) top-most layer of the cave system (b) central layer of the cave system (c) bottom-most layer of the cave system. 51*
Figure 3.1-8*: A horizontal section of the simple paleokarst flow simulation model showing oil saturation at 20 mD matrix permeability of the (a) top-most layer of the cave system (b) central layer of the cave system (c) bottom-most layer of the cave system. 52*
Figure 3.1-9*: A horizontal section of the complex paleokarst flow simulation model showing oil saturation at 30 mD matrix permeability of the (a) top-most layer of the cave system (b) central layer of the cave system (c) bottom-most layer of the cave system. 53*
Figure 3.1-10*: A horizontal section of the simple paleokarst flow simulation model showing oil saturation at 30 mD matrix permeability of the (a) top-most layer of the cave system (b) central layer of the cave system (c) bottom-most layer of the cave system. 53*
Figure 3.1-11*: A horizontal section of the simple paleokarst flow simulation model showing oil saturation at 40 mD matrix permeability of the (a) top-most layer of the cave system (b) central layer of the cave system (c) bottom-most layer of the cave system. 54*
Figure 3.1-12*: A horizontal section of the simple paleokarst flow simulation model showing oil saturation at 40 mD matrix permeability of the (a) top-most layer of the cave system (b) central layer of the cave system (c) bottom-most layer of the cave system. 55*
Figure 3.1-13*: Streamline simulation results at 40 mD background matrix permeability of (a) Complex simulation (b) complex paleokarst model (c) simple paleokarst model. 55*
Figure 3.1-14*: 3D sections of the complex paleokarst flow simulation model showing the waterflood front at matrix permeabilities of (a) 10 mD (b) 20 mD (c) 30 mD (d) 40 mD. 56*
Figure 3.1-15*: 3D sections of the simple paleokarst flow simulation model showing the waterflood front at matrix permeabilities of (a) 10 mD (b) 20 mD (c) 30 mD (d) 40 mD. 57*
Figure 3.1-16*: A plot showing the regional oil efficiency of increasing non-cave permeability in the complex paleokarst model. The regional oil efficiency represents the fraction of original oil recovered from the cave facies (bold lines) and the non-cave facies. 58*
Figure 3.1-17*: A plot showing the field oil efficiency of an increasing non-cave permeability in the simple paleokarst model. The field oil efficiency is indistinguishable for all the non-cave permeability cases. 58*
Figure 3.1-19*: A vertical cross section of saturation contrast (Left) in a long vertical cave region (in white rectangle) (a) 0.1 mD matrix permeability (b) 10 mD matrix permeability. (Right) A plot of flux from cave to matrix of increasing permeability....................................61*
Figure 3.1-20*: A vertical cross section showing saturation contrasts (Left) in a short horizontal cave facies region (in white rectangle) (a) 0.1 mD matrix permeability (b) 10 mD matrix permeability. (Right) A plot of flux from cave with increasing non facies permeability. 62*
Figure 3.1-21: A vertical cross-section showing saturation contrasts (Left) of a long horizontal cave passage near a producer (in white rectangle) (a) 0.1 mD matrix permeability (b) 10 mD matrix permeability. A plot of flux from cave with increasing non-cave facies permeability (Right). 62
Figure 3.1-22*: Oil saturation plot of different karst geometry (a) A vertical cross section of an 10 m inflow and 18 m out flow karst cavities and (c) the corresponding top view of*

outflow karst conduit (b) A vertical cross section of a 18 m inflow and a 18 m out flow karst cavities and (d) the corresponding top view of outflow karst conduit....................................*63*

Figure 3.1-23*: core section of karst infills from Tarim basin (a) conglomerate (b) sandstone (c) laminated mudstone (d) calcite (e) host rock (f) log section (g) overview of all the core section.* *64*

Figure 3.1-24*: Comparison of production from averaged and relative composition of cave infills.* *65*

Figure 3.1-26*: Saturation changes related to flow in different cave sections during water injection phases (a) 5 years of injection (b) 10 years of injection (c) 15 years of injection (d) 20 years of injection.*..*67*

Figure 3.1-27: A plot of cumulative oil produced from karsts with varying karst infill compositions. *68*

Figure 3.1-28*: Flow pattern in complex generic model with the horizontal wells outside the cave (top) oil saturation after 5 years of production (middle) oil saturation after 10 years of production (bottom) oil saturation after 20 years of production.*..*70*

Figure 3.1-29*: Flow pattern in complex generic model with the horizontal wells inside the cave (top) oil saturation after 5 years of production (middle) oil saturation after 10 years of production (bottom) oil saturation after 14.5 years of production. Production stops at 14.5 years because the reservoir pressure falls below the bubble point.* *71*

Figure 3:1-30*: Production plots of the simple generic model using horizontal well. (a) Oil recovery with wells in karsts only (bold lines) and matrix only (dashed lines) (b) cumulative oil produced from karsts only (bold lines) and matrix only (dashed lines).*...........................*72*

Figure 3.1-31*: Flow pattern in an inverted 5-spot box model showing wells located outside the cave (top) oil saturation after 5 years of production (middle) oil saturation after 10 years of production (bottom) oil saturation after 20 years of production.* *73*

Figure 3.1-32*: Flow pattern in an inverted 5-spot box model with the producer positioned inside the cave (top) oil saturation after 5 years of production (middle) oil saturation after 10 years of production (bottom) oil saturation after 20 years of production.*............................*73*

Figure 3.1-33*: Flow pattern in a 5-spot box model with injector wells positioned in cave (top) oil saturation after 5 years of production (middle) oil saturation after 10 years of production (bottom) oil saturation after 20 years of production.*..*74*

Figure 3.1-34*: Flow pattern in a 5-spot box model with injector wells outside after 5 years of production.*..*74*

Figure 3.1-35*: cumulative oil production from both karst (bold line) and matrix (dashed line) using different well patterns.*...*75*

Figure 3.1-36*: Oil efficiency for both karst (bold lines) and matrix (dashed) using different well patterns.*..*75*

Figure 3.2-1*: Workflow for the EDKM upscaling technique (M. Correia et al., 2019).* *76*

Figure 3.2-2*: workflow of upscaling methodology adopted in the thesis.* *77*

Figure 3.2-3*: Horizontal sections showing saturation contrasts of the complex paleokarst model at different scale of upscaling done at (a) 6 m grid cell diameter (b) 10 m grid diameter (c) 15 grid cell diameter (d) 30 m grid cell diameter. Note how the cave geometry is smoothened out as the grid diameter is increased.*..*79*

Figure 3.2-4*: Vertical sections showing saturation contrasts of the complex paleokarst model at different scale of upscaling done at (a) 2 m grid cell diameter (b) 6 m grid diameter (c) 10 m grid cell diameter (d) 15 m grid cell diameter (e) 30 m grid cell diameter.*........................*80*

Figure 3.2-5*: Horizontal sections showing saturation contrasts of the simple paleokarst model at different scale of upscaling done at (a) 6 m grid cell diameter (b) 10 m grid* *diameter (c) 15 m grid cell diameter (d) 30 m grid cell diameter. Note how the cave geometry is smoothened out as the grid diameter is increased...81*

Figure 3.2-6*: Vertical sections showing saturation contrasts of the complex paleokarst model at different scale of upscaling done at (a) 2 m grid cell diameter (b) 6 m grid diameter (c) 10 m grid cell diameter (d) 15 m grid cell diameter (e) 30 m grid cell diameter. Note how the cave geometry is smoothened out as the grid diameter is increased......................................82*

Figure 3.2-7*: Cumulative oil production comparing a fine grid complex paleokarst model and its respective upscaled versions...83*

Figure 3.2-8: *Cumulative oil production comparing a fine grid simple paleokarst model and its respective upscaled versions...83*

Figure 3.2-9*: A plot showing a comparison of watercut from fine grid and the courser grids of the complex paleokarst model...84*

Figure 3.2-10*: A plot showing a comparison of watercut from fine grid and the courser grids of the simple paleokarst model. 84*

Figure 3.3-6*: Workflow from flow simulation to seismic modelling of generic paleokarst carbonate reservoirs...90*

Figure 3.4-1*: workflow for fracture modelling for generic paleokarst models...................100*

Figure 3.4-2*: Flow pattern in a horizontal section of a fractured complex generic geometric karst model (a) after 5 years of production (b) after 10 years of production (c) after 15 years of production..101*

Figure 3.4-3*: Flow pattern in a horizontal section of a fractured simple generic paleokarst model. (a) after 5 years of production (b) after 10 years of production (c) after 15 years of production...102*

List of tables

Table 1.4-1: Description of paleokarst deposits...18
Table 1.5-1: Dimensions used for crucial volumes in multi-scale reservoir modelling (Ringrose & Bentley, 2015). 25
Table 2.3-1: Input parameters for generic paleokarst models. 32
Table 2.3-2: CPU times achieved with different linear solvers...39
Table 2.6-1: Input parameters to a fracture model used to populate the generic model with fractures...42
Table 3.3-1: Elastic moduli and densities of a two mineral component adopted in the rock..85
physics models (Johansen, 2018)....85
Table 3.3-2: An overview of different rock models used in the rock physics modelling (Johansen, 2018)....85
Table 3.3-3: Input parameters used for synthetic seismic modelling. 92

Nomenclature

Ø = Porosity (fraction/percentage)
K = Permeability (mD)
q = Fluid flow rate through medium (m^3/sec)
A = Area (m^2)
μ = Viscosity (cP)
L = Length (m)
m = Metre
mD =millidarcies
D =Darcy
K_{sat}= Saturated bulk modulus (GPa)
K_{dry}= Frame bulk modulus (GPa)
K_m= Matrix bulk modulus (GPa)
K_{fluid}=Fluid bulk modulus (Gpa)
$\boldsymbol{\Omega}$ **=** domain
$\boldsymbol{\Omega}^f$ **=**Domain in the free flow region
p^ε= fine scale pressure
ε= length scales of both fine and coarse scales.
$\boldsymbol{v}^\varepsilon$ = permeability tensor
S_w= Water saturation (Fraction/percentage)
PSF =Point Spread Function
RAM = Random Access Memory

1 INTRODUCTION

This section gives an overview of the thesis, carbonates, paleokarst reservoirs, flow simulation and previous work related to the study of paleokarsts.

1.1 Motivation

Carbonate reservoirs account for about 50-60% of the total conventional hydrocarbon reserves worldwide (Burchette, 2012). Fracture-cavity reservoirs account for more than 30 percent of these carbonate reservoirs and have been an important target for petroleum exploration and development (Kerans, 1988; J. Li et al., 2008; R. G. Loucks, 1999; Popov et al., 2009). Many larger carbonate reservoirs associated with paleokarstic features such as considerable dissolution and collapse are widely distributed all over the world. For example, the Rospo Mare Field in the Adriatic Sea (Fournillon et al., 2017), the Ghawar field in Saudi Arabia (Afifi & Discovery, 2005), the Yates field in West Texas, and Tahe oil field in China (Zhang, 1999). The Gohta and Alta Prospects discovered in the southern Barents Sea by Lundin Norway AS in 2013 and 2014, respectively, demonstrated the presence of paleokarst reservoirs on the Norwegian shelf. However, after field appraisal in 2017, poor reservoir quality was encountered in the Gohta appraisal well (7120/1-5) while the Alta appraisal proved a success with good reservoir properties, communication, and excellent production rates. Giant oil fields such as the Ghawar field in Saudi Arabia and the recently discovered Brazilian pre-salt reservoir in the Tupi area calls for new methodologies and application of techniques developed for paleokarst reservoirs. Heterogeneities in paleokarst reservoirs arise from the thin high permeability layers or horizontal fracture patterns (M. G. Correia et al., 2017). High permeability zones in Brazilian pre-salt such as the coquinas (lacustrine facies), microbial build-ups and travertines present high fluid flow rates (Boyd et al., 2015). Voelker and Caers (2004) classified the ‘‘super-k’’ zones as fractured, high permeability layers and high flow zones in the Ghawar Field. Most of the studies in paleokarst reservoirs are restricted to structural, stratigraphic and sedimentological aspects (R. G. Loucks, 1999; Tinker & Mruk, 1995). Moreover, detailed reservoir characterization and methods for realistically modelling cave features are limited (Henrion et al., 2008). Complex structure of the paleokarst facies are modelled by using high permeability streaks (Dogru et al., 2001), dual-porosity or dual-permeability formulations (Uba et al., 2007) in reservoir engineering applications. To capture and integrate geological features with numerical simulation, upscaling is employed. The process of upscaling is important because it aids in estimating large-scale flow properties from small scale reservoir properties. Emphasis is placed on traditional upscaling methods such as averaging and homogenization while advanced upscaling methods are disregarded because are beyond the scope of this work. Arithmetic averaging is used for porosity while geometric, harmonic, and diagonal tensor were used for permeability. These averaging methods yield nearly similar results on flow simulation and thus the choice of the averaging methodology was less significant. Other methods such as pseudo functions and flow-based numerical methods can be applied for upscaling paleokarst reservoirs. The advantage of flow-based numerical upscaling over pseudo functions based upscaling is that it is best suited for capturing permeability (Noetinger et al., 2004). Flow simulation in paleokarst can be modelled using a structured grid with matrix, karst features, and fracture media. The karst elements include different geometries and sizes. In this thesis, flow simulation is performed on generic paleokarst models with either fractures or without fractures in the grid domain. The concept addresses a simple methodology of modelling paleokarst reservoirs for flow pattern control studies and sensitivity analysis. A recent relatively robust method called Embedded Karst Model (EDKM) developed by (M. Correia et al., 2019) which is a continuation of a previous methodology (Embedded Discrete Fracture Model, EDKM) by (Moinfar, 2013) includes a volume that represents both karst geometries and features. This method greatly maintains resolution of the karstic elements in the coarser model and is reported to reduce the computing time by 95%. Previous studies on paleokarst reservoirs by the FOPAK project have dealt mainly with geomodelling and fluid simulation (Furnée, 2015; Ledsaak, 2016), seismic modelling (Johansen, 2018) and collapse (Målbakken, 2009). However, few studies have addressed capturing the geometric and upscaling aspect into geomodels by rendering. This thesis focuses mainly on flow sensitivities in cave geometries classified by R. G. Loucks (1999) and those described by (Skoglund et al., 2011) as network maze. Other topics included in this study are upscaling methods, cave infill effect on production, seismic modelling and time-lapse (4D seismic).

1.2 Research objective

The main objectives of this work are to

1. investigate sensitivity and upscaling effect on cave systems of varying size,
2. investigate to what extent simplified rendering of complex geometries can be employed when modelling and simulating paleokarst reservoirs,
3. study flow pattern controls and sweep efficiency in collapsed cave infill sediment,
4. compare flow simulation of paleokarst models with fractures or without fractures, and
5. Match flow simulation results with 4D seismic modelling results.

During my study, I preliminarily presented objective (1) at the NGF winter conference in Oslo (appendix 1) and an extended abstract on objectives (1) to (3) got accepted for an oral presentation at the 82nd EAGE annual conference (appendix 2). To analyse detailed flow controls integrated with upscaling procedures, a simple generic paleokarst model and complex generic paleokarst model constructed with the same grid size are compared. The simple generic paleokarst model consists of mainly large connected conduits constituting a simple network while the complex geometric model consists of cave conduits of varying sizes with a very complicated network system. The comparison addressed the following aspects:

- Flow behaviour in karst features of varying diameter and length,
- Flux per unit length in passages of the same length,
- Impact of karst geometry and size on sweep efficiency,
- To what extent are the flow properties of paleokarst features preserved during upscaling,
- Threshold background (matrix) permeability where there is tendency of uniform flow across the reservoir,
- Flow pressure response in connecting passages of varying diameter, and
- 4D seismic reservoir monitoring.

Identification of flux rate sensitivity to different aspects such as permeability and inflow and outflow geometries is done in three steps. The first is a direct comparison of simulated injection and production behaviour of the two model versions using a series of production scenarios. The second step depends on the results from the first, and can involve either (a) an iterative adjustment of the simplified model in order to investigate if a better match with the detailed model can be achieved, (b) an iterative simplification of the detailed model to establish at what point simulation results significantly deviate from the initial model(c) comparison of fluid substitution with the reservoir over a period of time with a base model using changes in seismic amplitude. This step is the 4D seismic modelling. The rock physics models used for the 4D seismic modelling were adopted from previous work by Martin Kyrkjebø Johansen (Johansen, 2018). He established a workflow for producing synthetic seismic models of paleokarst reservoirs using rock physics templates and seismic forward modelling. A summary of the thesis workflow is shown in Figure 1.2-1.

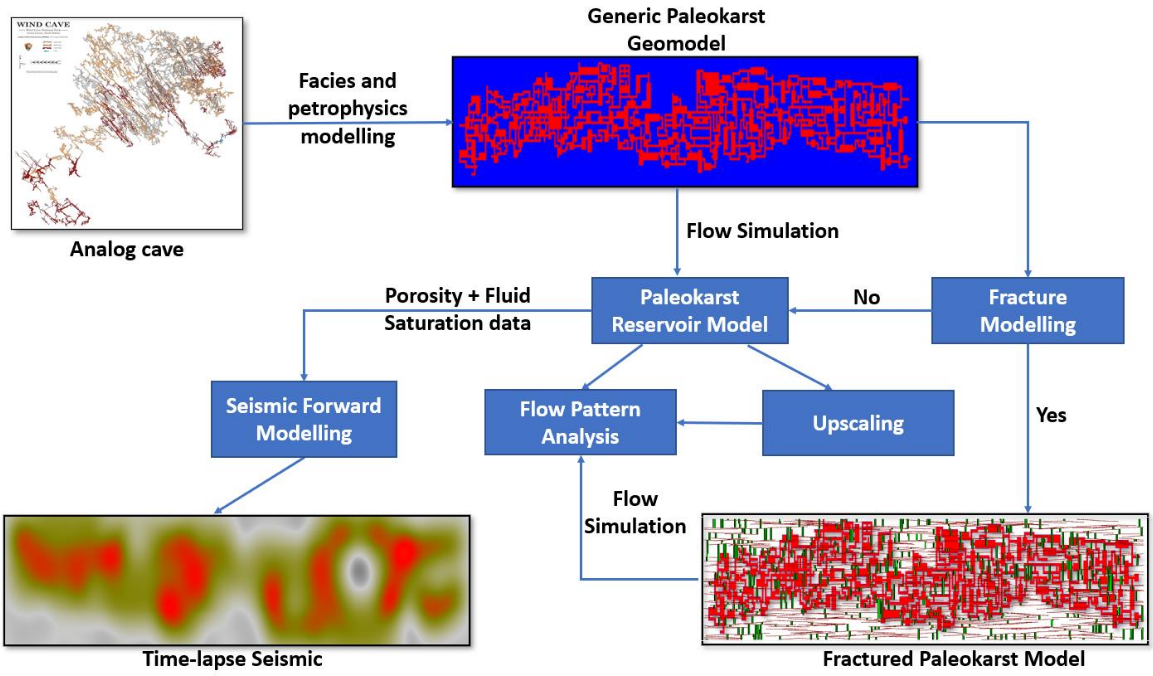

Figure 1.2-1: *Workflow used in the thesis for flow simulation and seismic modelling.*

1.3 Carbonates

1.3.1 Formation and composition

The origin of paleokarst reservoirs is not only from carbonate rocks but also from evaporitic rocks such as salt and gypsum, and metamorphic rocks like marble. In this section, emphasis will be put on processes that form carbonate rocks and their composition. Carbonate rocks are formed by both biological and chemical processes in areas of shallow, tropical to subtropical and high-altitude low temperature water shelves. In these areas, massive production of carbonates by direct precipitation from saturated sea water, chemical, and biological extraction occur. They are referred to as "carbonate factories" (Lucia, 2007). Carbonate sediments are composed of mainly bioclastic skeletal grains, ooids, peloids, fossil fragments, sub-rounded grains, intraclasts, carbonate mud and cement. It is important to note that sediments transported and deposited by physical processes during the formation of carbonates are identical to those that form siliciclastic rocks. After deposition, diagenetic processes that alter porosity and the rock chemistry follow. Other processes that form carbonate rocks are *in situ* growth of skeletal structures (e.g. corals) and grain-grain binding trapping by microbials. Primary and secondary structures such as lamination, crossbedding and bioturbation maybe preserved in carbonate rocks (e.g. growth laminations and clastic laminae). Bioerosion is another important process involving crushing, scrapping, and boring of shell material into small particles that serve as building blocks of carbonate sediments. The most common carbonate rocks are calcite ($CaCO_3$), limestone ($CaCO_3$) and dolomite ($Ca (Mg (CO_3)_2$). Limestone and dolomite are both carbonate rocks of sedimentary origin with at former having least 50% of its composition coming from calcite or aragonite while the later consists of at least 50% dolomite (Boggs Jr, 2014). Carbonates when subjected to high temperatures and pressure form metamorphic rocks for example marble. Marble is composed of mainly recrystallized limestone.

1.3.2 Limestone

Limestone comprises of a broad mineral spectrum with not only a general formula of $CaCO_3$ but also differing magnesium content and crystal structure. Limestone can manifest in three forms depending on the magnesium content i.e high magnesium calcite (>4% $MgCO_3$), low magnesium calcite (<4% $MgCO_3$), and aragonite. Aragonite represents limestone deposited in modern day oceans while low magnesium content calcite represents limestone produced in sea water during the early Paleozoic-mid Cenozoic geologic era. Aragonite is more soluble because it possesses a less stable crystal structure (orthorhombic) than calcite that possess the very stable rhombohedral crystal structure (Boggs Jr, 2014).

1.3.3 Dolomite

Dolomite is made up of 50% or more of calcium-magnesium (Ca (Mg $(CO_3)_2$) which is a product of ionic substitution of Ca^{2+} by Mg^{2+} in a solution state. This substitution process is called dolomitization. Dolomitization requires fluid flow for the introduction of Mg^{2+} ions in the system leading to the formation of dolomite. This is a reversible chemical reaction described by the equation (1):

$$2CaCO_3 + Mg^{2+} \longleftrightarrow CaMg(CO_3)_2 + Ca^{2+}. \qquad (1)$$

At near surface depth, dolomite possess a lower porosity than limestone. At greater burial depth however, the dolomite porosity is preserved and does not change significantly because dolomite possess higher degree of resistance to both chemical and mechanical compaction than limestone (Schmoker & Halley, 1982). The compressive strength of dolomite is attributed to its hexagonal crystal structure. The difference in porosity of dolomite and limestone at both shallow and deep depositional environment is regarded of greater importance when characterizing carbonate reservoir properties. Carbonates generally exhibit 40-70% porosity at deposition (Choquette & Pray, 1970) but on burial to greater depth, compaction reduce it rapidly except for dolomite.

1.3.4 Marble

Marble is metamorphic carbonate rock formed when limestone is subjected to conditions of high temperatures and pressures. Under these extreme conditions, the calcite in the limestone recrystalizes to form a very denser rock with equigranular calcite crystals. The colour of marble may vary from pink, dirty white or white depending on the amounts of impurities incorporated into the calcite during the metamorphism process. Marble form an important host rock for the formation of karsts especially when rivers flow through the marble formations at high velocities and scouring the surfaces into small scallops or bigger trenches for example the Marmorslottet marble castles in Mo i Rana in Northern Norway (Figure 1.3.1)

Figure 1.3.1: *River Glomåga cuts through marble to form the Marmorslottet castles in Mo I Rana (Photo credit: Mustaqim Balyesiima).*

1.3.5 Evaporites

Evaporites can be categorised as either marine or non-marine depending on depositional setting and the source of water (sea water, hydrothermal, volcanogenic, or diagenetic). Marine evaporites form by evaporation of a closed sea water basin and precipitation of chlorides, sulphates, carbonates, and borates in marginal salt pans, marine salinas, lagoons and relict sea (Stewart, 1963) while non-marine are derived are evaporation of water originating from hydrothermal, volcanogenic, diagenetic and mixed sources in non-terrestrial deposition setting (Hardie, 1984). It is important to acknowledge that a marine depositional environment is not a proof of evaporites forming entirely from sea water but rather a combination of other hydrologic sources (Hardie, 1984). From Cambrian to present, thick and continuous beds of evaporites and other sediments were laid in basins and shelf areas separated from oceans and seas by barriers of zones of either biogenic or tectonic origin (Stewart, 1963). The main elements in sea water are chlorine, sulphur, calcium, magnesium, and potassium. On evaporation, evaporites formed may consist of lateral or concentric layers of calcium carbonate ($CaCO_3$), gypsum ($CaSO_4$), sodium chlorides (NaCl) and salts of potassium and magnesium. The lateral extent and variation in mineral content of the evaporites is dependent on the proximity to the shoreline, water depth and thermal current while the vertical intercalations are dependent on the sea water flooding cyclicity and temperature (Stewart, 1963).

1.3.6 Diagenesis of carbonates

Diagenesis refers to physical and chemical processes that alter the composition and texture of sediments after deposition. According to Chilingar et al. (1967), there exists at least 30 diagenetic processes that may alter carbonate sediments depending on the locality of the deposition setting but the most common are lithification, dissolution, recrystallization and cementation. Lithification is a combination of physical, chemical, or biochemical processes that may compact or cements the carbonate sediment. Dissolution may trigger partial replacement of carbonate to form new carbonate rocks for example Dolomite (dolomitization) and silica cements (silicification). Recrystallization plays a major role in the development of the texture of carbonate rocks.

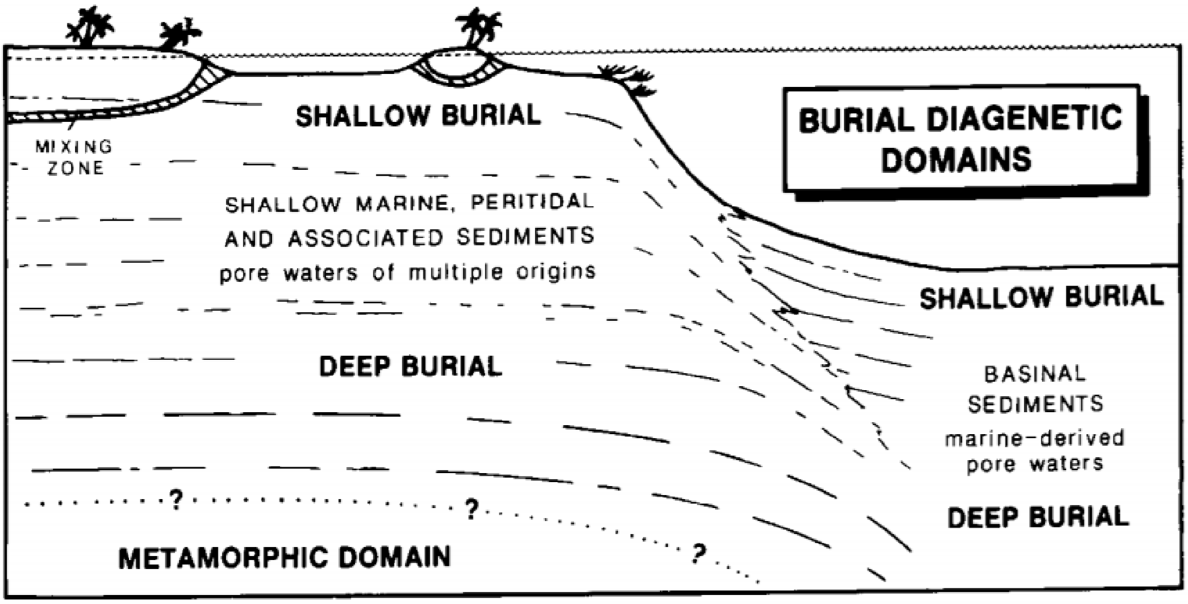

Figure 1.3-2: The different diagenetic realms of carbonate rocks (Choquette & James, 1987).

C. H. Moore (1989) described three main environments of diagenesis where porosity modification of carbonate sediments takes place (Figure 1.3-2). These are meteoric, marine, and subsurface. The meteoric environment lies mainly in the near surface and is characterized by subaerial exposure with moderately dilute hydrologic fluids with a multiscale of saturation degrees from undersaturated to the supersaturated. The undersaturated meteoric waters have low concentration of metastable carbonate species like aragonite and magnesian calcite while the supersaturated state consists of a solution of very stable carbonate minerals like calcite and dolomite (Bathurst, 1975). In the soil covering the vadose zone (above the water table) there is an abundance of carbon dioxide that greatly affect the saturation of the water in comparison to the neighbouring carbonate minerals. The high concentration of CO_2 may lead to porosity reduction by precipitating cements within the carbonate sediments while porosity enhancement may occur by percolation of fluids through the phreatic zone (Hanshaw & Back, 1979).

The marine environment in the carbonate diagenesis realms is characterized by modified pore fluids supersaturated with respect to a wide range of carbonate minerals (Bathurst, 1975).At moderate burial depth in the marine setting, porosity loss by cementation is extensive while the deep marine setting has high potential of formation of secondary porosity by dissolution (saturation reduces with depth). The extent of distribution of cements in carbonate sediment pores is governed by the flow rate of fluids and therefore influenced by prevailing depositional conditions, sedimentation rate, porosity, and permeability (C. H. Moore, 1989). Cementation is not limited to only marine environments but extends to other carbonate diagenetic realms such as shelf margin reef and the intertidal zone (C. H. Moore, 1989).

The subsurface environment consists of a mixture meteoric and marine waters, (R. L. Folk, 1974) and brine originating from pore water interaction exposed to condition of high temperatures and pressures (Scholle et al., 1983). The interaction of pore water elevates the saturations of very stable carbonate minerals for example calcite and dolomite but increase in temperature and pressure (with respect to depth) results into porosity destruction by pressure solution (Choquette & James, 1987). Pressure solution initiates cement precipitation filling majority of the pore system. In deeper subsurface however, cement precipitation occurs at a slower rate because movement of fluids is minimal.

1.3.7 Classification of carbonate rocks

There exist many ways of classifying carbonate rocks based on texture, depositional environment and very rarely on mineralogy. The most widely used classification criteria are described by Folk (1959) and Dunham (1962) in Figure 1.3-3 (R. Folk & Dunham, 1962); R. L. Folk (1959) presents a model for classifying carbonate rocks based on the relative abundance of three main components of carbonate rocks: sparry calcite cement (sparite), microcrystalline carbonate mud (micrite), and carbonate grains. Dunham (1962) classification describes the original depositional textures of carbonates. After Folk and Dunham, Embry and Klovan (1971) proposed a classification based on bio-carbonates while Riding (2002) classified microbial carbonates.

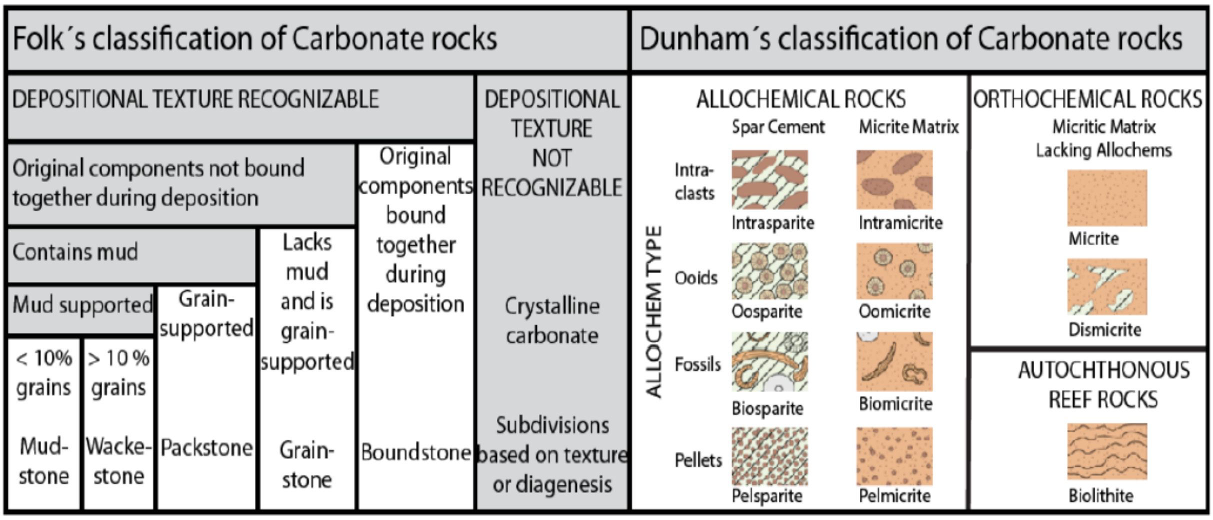

Figure 1.3-3: *Folk's and Dunham's classification of carbonate rocks, adapted from (R. Folk & Dunham, 1962).*

1.3.8 Porosity types in carbonate rocks

Porosity in carbonates is not a straightforward subject and is more complex than siliciclastic rocks mainly because of their organic origin and easy to physical and chemical alteration. The size and shape of the pores may vary depending on the extent of diagenetic processes involved in the formation of carbonate rocks resulting into different porosity types as described by C. Moore (2001) in Figure 1.3-4.

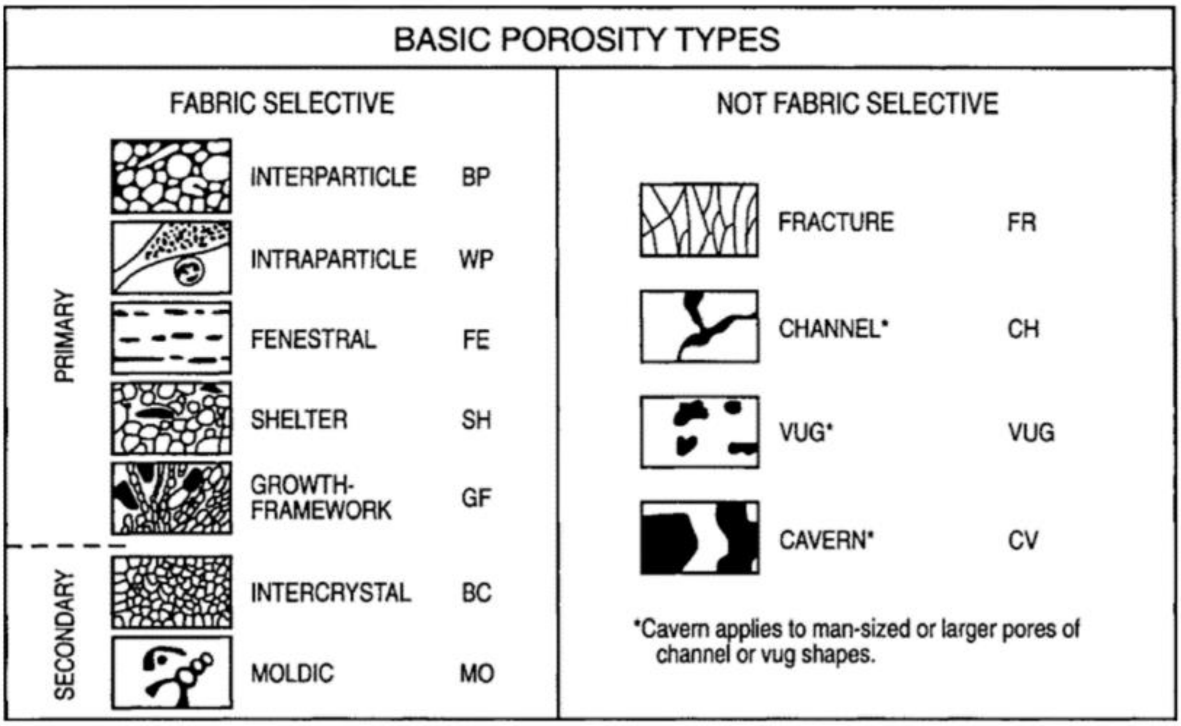

Figure 1.3-4: *Classification of porosity types (C. Moore, 2001).*

Three types of porosities exist in carbonate rock i.e primary, secondary porosity and structural. Primary porosity describes porosity at the onset of deposition of carbonate sediments. Secondary porosity develops after depositional processes. Structural porosity develops when carbonate reservoirs are subjected to episodes of tectonic events. C. Moore (2001), and (A. Lønøy, 2006) extended (Choquette & Pray, 1970) work on the classification of pore types by subdividing primary and secondary porosity. Pore types classified under primary porosity are interparticle, intercrystalline, growth framework, and shelter while pore types classified under secondary porosity are moldic, intercrystal, vuggy, solution and caverns. Interparticle, intraparticle and intercrystal porosity are characterized by the pore position in respect to pore size, shape, and the origin. Interparticle porosity refers to porosity originates from spaces between individual particles while intercrystalline porosity represents pore spaces between individual crystals. Fenestral porosity is a subclass of interparticle pores but are generally large. Porosity can also result from space existing within grains (intraparticle) or crystals (intracrystalline). Pore types of secondary origin are moldic, channel and cavern porosity. Moldic porosity is only defined based on origin and is developed by either partial or total dissolution (A. Lønøy, 2006). Vuggy and channel porosities develops in pores based on several attributes. Vuggy pores are large and penetrate through cements (non-fabric) transforming them into a more connective network (A. Lønøy, 2006) while channel pores are large pores develop by dissolution along fractures. Cavern pores differ from vuggy pores because they are very large in size. In very brittle carbonate rocks, porosity may occur due to high pressure and are called fracture pores (structural porosity).

1.4 Paleokarst

Paleokarst refers to ancient karst features formed over a long period of time and are no longer active (R. G. Loucks, 1999). The processes that contribute to the formation and modification of karst systems are chemical dissolution, precipitation, erosion, sedimentation, and collapse of landforms. Deactivation of a karst system may occur when one or more of these process decreases or halted. Paleokarst can be reactivated resulting into more than one phase of karstification. When the processes forming a karst ceases, infilling of the cavities by different sediments and cements occur. Paleokarst features exists in a wide range of permeable rocks and environments and are not restricted to only carbonates for example dolomites, marble, reef structures, gypsum, halite, and ice environments. The permeable pathways within the host rock are developed along depositional pore space, syn-sedimentary pores and tectonic fractures (Smart et al., 1988). The soluble host rock is dissolved by flowing streams, meteoric waters, magmatic fluids, hydrothermal fluids, and seawater to form different karst systems. The evolution and development of a karst (Figure 1.4-1) is dependent on the time, locality, and the geological condition of the exposed rock.

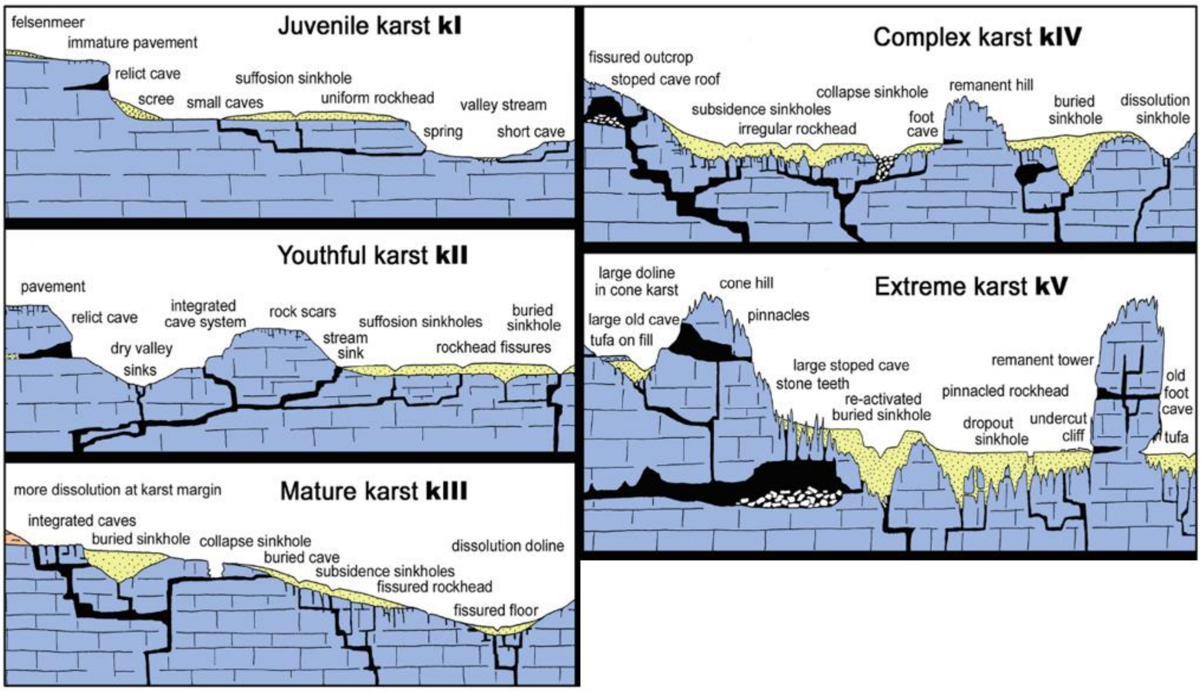

***Figure 1.4-1**: Engineering classification of karst (Waltham & Fookes, 2005).*

The processes that modify majority of the karsts can either by epigenetic or hypogenetic. Epigenetic processes are associated with surface run-off or meteoritic water percolation through the host rock while hypogenetic processes involve the corrosive action of acidic gases dissolved in hydrothermally driven ground water. A paleokarst is not a specific type of karst but rather a condition undergone by a karst such as fossilization. The types of paleokarst (Figure 1.4-2) are buried karst, relict karst, interstratal karst, intrastratal karst and subjacent karst (Klimchouk, 1996).

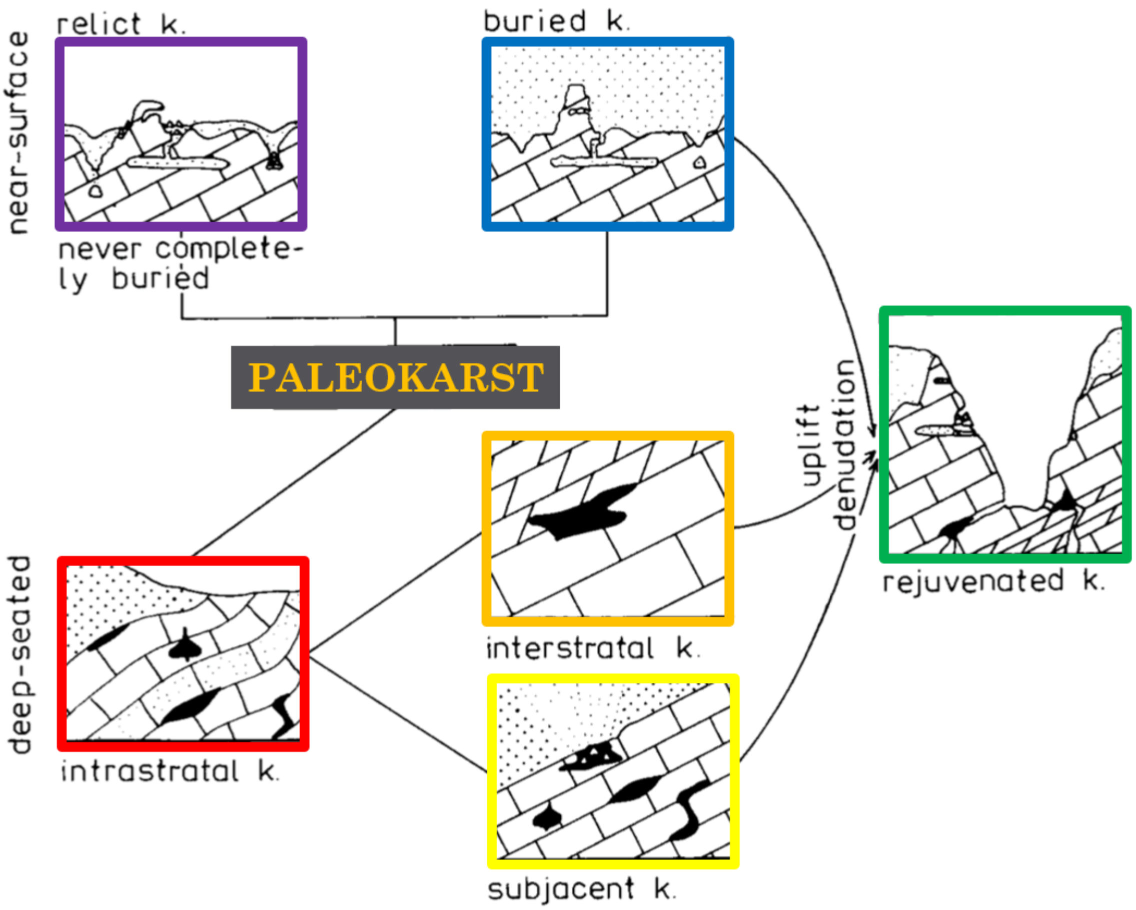

***Figure 1.4.2**: Types of paleokarst (Klimchouk, 1996).*

Buried karst

This is a type of paleokarst formed by processes that occur at the surface of the earth and later buried by rocks (Klimchouk, 1996). The karst formed is older than the surrounding strata manifesting as a disconformity or unconformity.

Relict Karst

Relict karst represents karst landforms created at the surface of the earth under a set of morphogenetic conditions and can survive alteration when subjected to different conditions of modern day (Klimchouk, 1996). They exhibit characteristics of small rill-karrens or big cave systems.

Interstratal karst

This refer to karst that develop by dissolution of soluble rocks along the bedding planes or disconformities (Klimchouk, 1996).

Intrastratal and subjacent karst

Intrastratal karst is where there is artesian confinement and flow in mainly upstream while subjacent karst develops below less soluble strata (Klimchouk, 1996).

The extent of cave development is determined by subaerial exposure whereas cave passages that are either connected or disconnected with different level of heterogeneities are formed by either near surface processes or burial processes (extent (Wright et al., 1991). Collapse of the rocks above the cave passages and infilling by sediments and precipitated cements within the cavities results into different geometry (Figure 1.4-3) that vary in scale and complexity (R. G. Loucks, 1999).

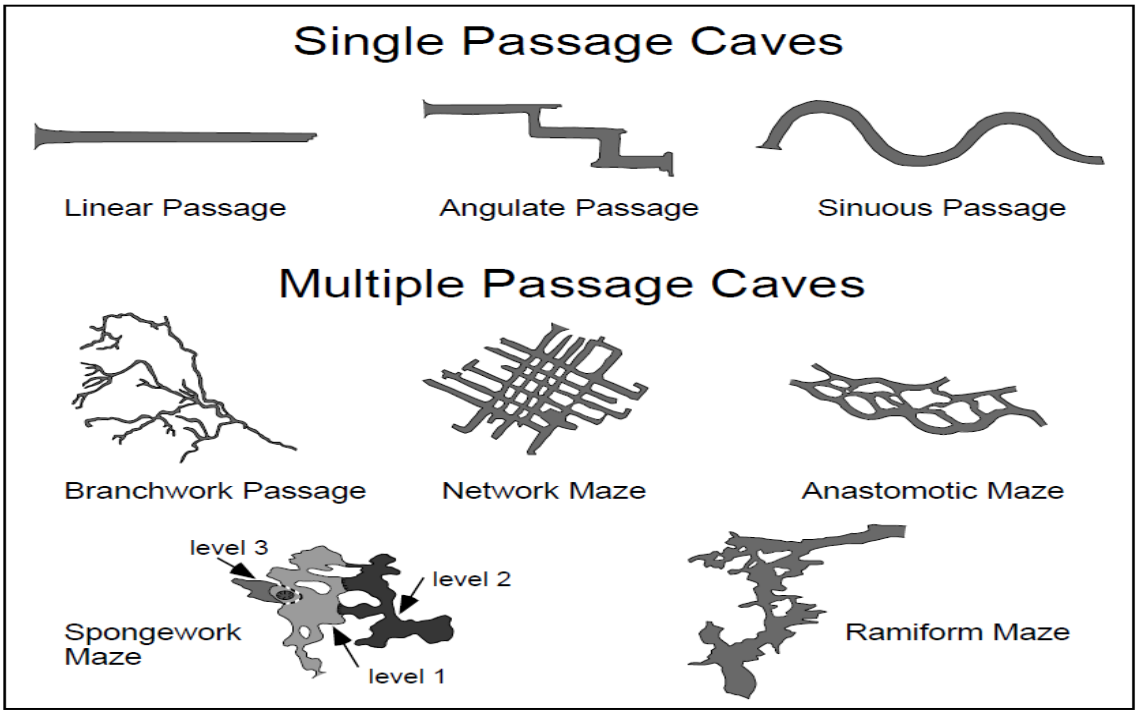

***Figure 1.4-3**: Classification of near surface cave geometries and passages (from Loucks,1999).*

1.4.1 Burial and diagenesis of paleokarst deposits

Paleokarst deposits are a combined contribution from both near surface and burial processes whose pattern of distribution is directly controlled by the parent cave geometry and cave passages size (Hammes et al., 1996; Kerans, 1988; R. G. Loucks & Handford, 1996; Mazzullo & Chilingarian, 1996). The distribution of paleokarst deposits is very complex at micro-scale, meso-scale to field scale. At every scale, the distribution of infill from clastic sedimentation, collapse and brecciation influences porosity and permeability in the paleocave system. Early speleologists reported finding cave passages completely clogged with ice that no longer exists to date (Horn, 1947). At present, traces of cryogenic carbonate found in caves in northern Norway may be evidence of ancient ice deposits that melted over time (Lauritzen et al., 2018). Paleokarst deposits found in areas with high geothermal activities may contain lava deposits for example the lava caves in Iceland (Hróarsson & Jónsson, 1991). The widely used conceptual model showing the evolution of processes from formation, collapse, and burial of paleocave passages is based on the work of R. G. Loucks (1999) as illustrated in Figure 1.4-4 while the corresponding paleocave facies are described in Figure 1.4-5, and Table 1.4.1. This conceptual model describes a transition of a cave passage with falling water level from the phreatic zone to the vadose zone. The falling water level causes water that initially filled and supported the weight on the cave ceiling to flow out of the cave passage resulting into a possibility of collapse of the ceiling and the cave walls. After the collapse, cave is then filled with a variety of breccia as from chaotic breakdown, and sediment sediments as classified by ternary diagram in Figure 1.4-6.

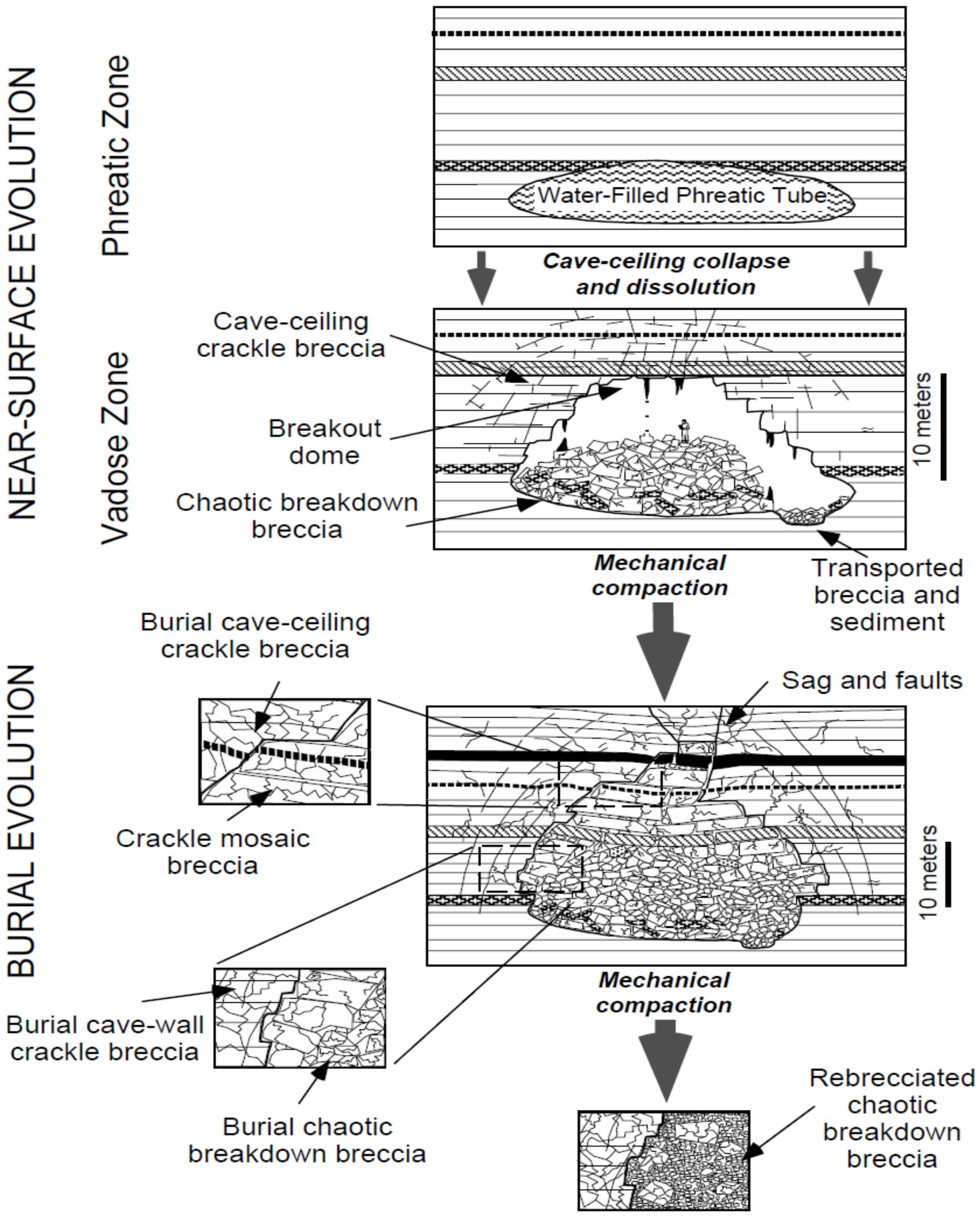

***Figure 1.4-4**: Paleocave collapse and compaction stages (R. G. Loucks, 1999).*

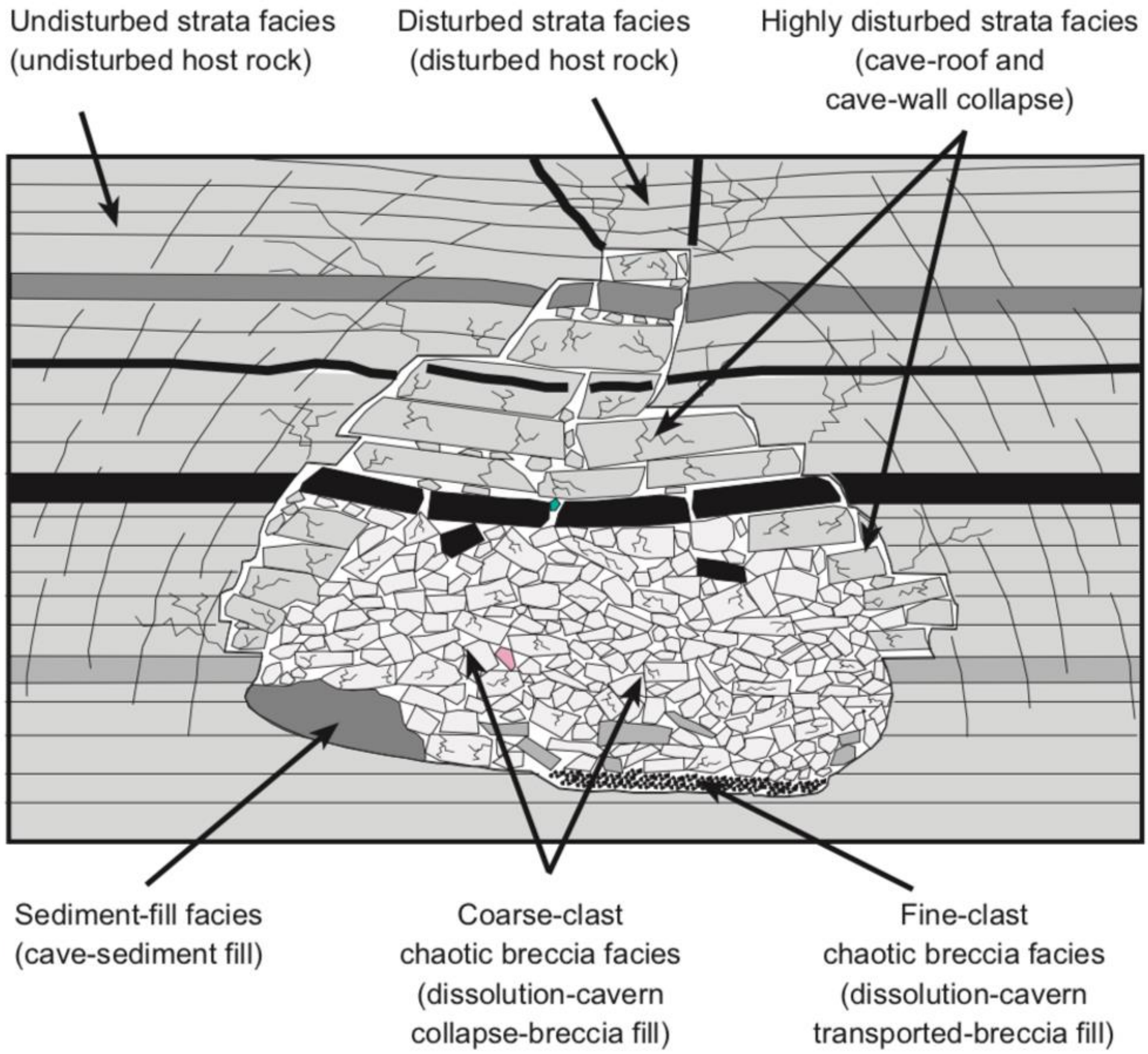

Figure 1.4-5: *Description of facies in a buried karst (R. G. Loucks, 1999).*

Table 1.4-1: Description of paleokarst deposits.

Paleokarst deposits	**Characteristics**
Undisturbed strata	Excellent bedding continuity for several metres.
Disturbed strata	Bedding continuity but folded and offset by faults.
Highly disturbed strata	Consists of collapsed host rock from cave roof.
Coarse-clast chaotic breccia	Poorly sorted, granular to boulder sized breccia clasts.
Fine clast chaotic breccia	Laterally sorted by water or ice, consists of transported breccia cavern fill. Moderated sorted and chaotic with granular-to cobble sized clasts.
Cave sediment cavern fill	Consists of carbonates or siliciclastic.

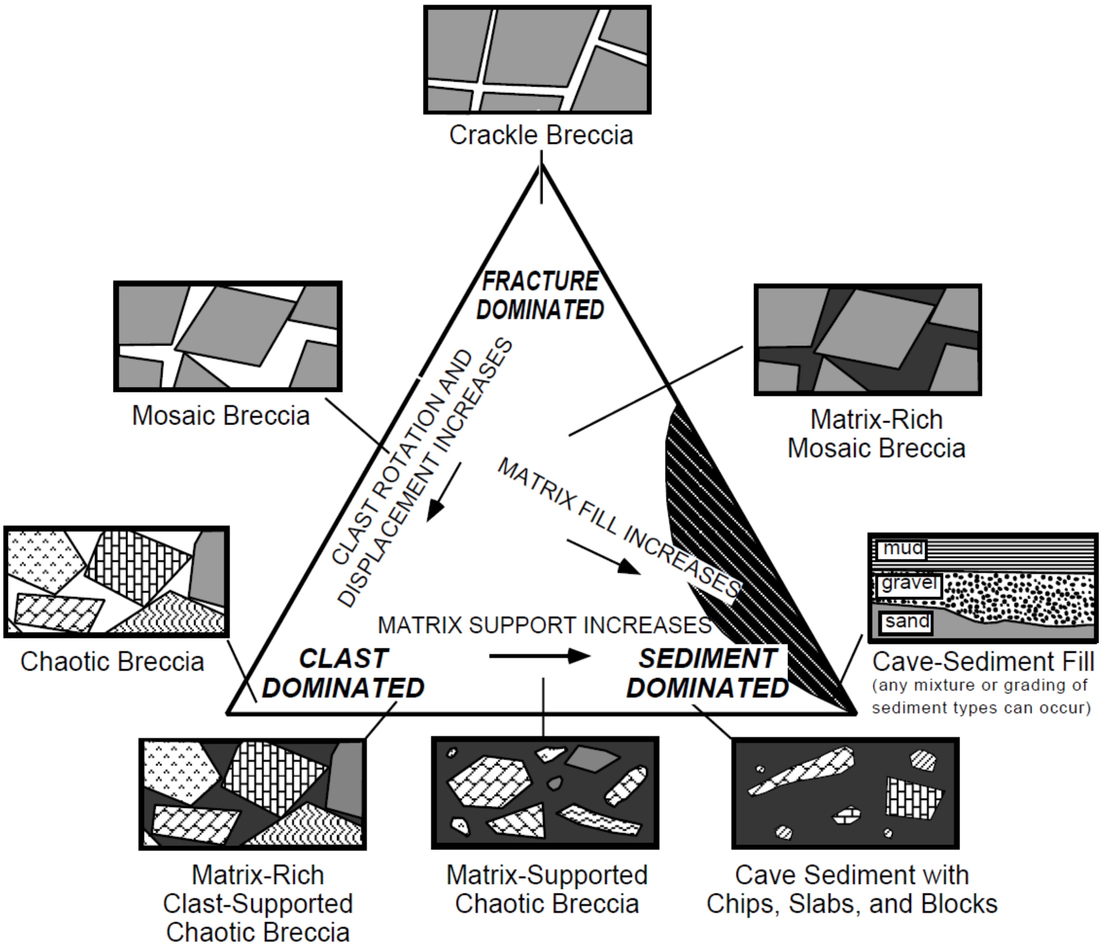

***Figure 1.4-6**: Classification of cave infills (Loucks,1999).*

When paleokarsts are coalesced by compaction, porosity modification may occur. R. G. Loucks (1999) categorized porosity based in paleocave deposits on a ternary diagram (Figure 1.4-6) as (1) cavernous porosity, (2) inter-breccia porosity between clasts, (3) fracture porosity in clasts, walls, and ceilings, (4) matrix porosity in cave-sediment fill, and (5) limited matrix porosity in host wall rocks and in breccia clasts. Porosity in the matrix is lower than the coalesced cave collapse because karstification in areas of continental karsts takes place only in carbonates with less matrix porosity (Palmer, 1991). However, during burial, chemical precipitation causes cementation of the pore system greatly reducing porosity. Depth can also destroy porosity in paleocave system for example at burial depth greater than intragranular porosity ceases to exist. Tectonic faults and fractures contribute to communication (permeability) between the different pore systems in paleokarst reservoir (R. Loucks & Anderson, 1980; Mescher et al., 1993; Tinker & Mruk, 1995). The different linking pore systems stretch over metres to kilometres and are sweet spots for hydrocarbon exploration. From several studies on porosity in huge piles of collapsed material in mines (Pappas & Mark, 1993), cavity infill and collapse porosity classification ranges on average from 80% before burial to about 25% after compaction. If the roof of a cavity remains intact during burial, any sediments present in it will be sheltered from compaction, but not from cementation. Preliminary findings from a study of cave infills in Maras cave in Greece (Figure 1.4-7), Lønøy et al., 2019 suggested that sediment infills may contribute significantly to paleokarst reservoir pore volume. Infill by sediments happens both during the active and inactive stages of cave evolution and are commonly very heterogeneous, making classification difficult.

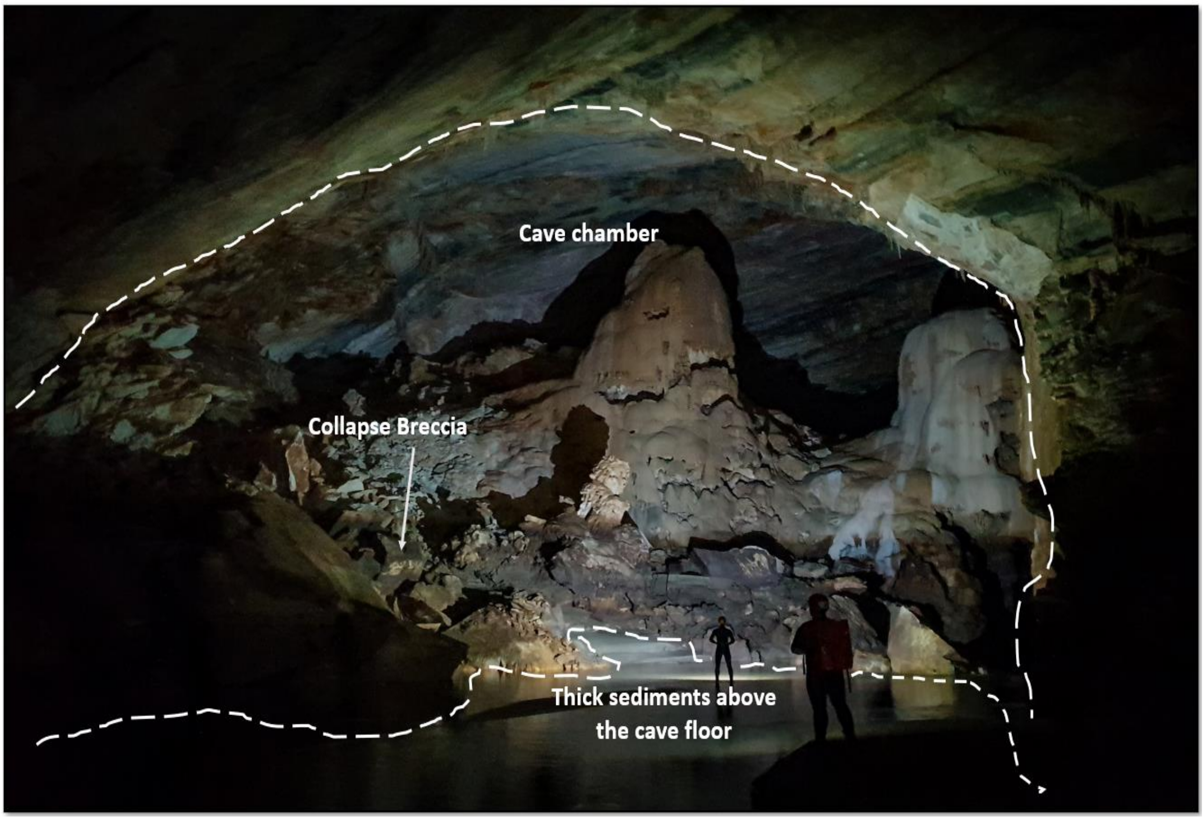

Figure 1.4-7: *A large chamber from Maras cave partly filled with thick clastic sediments and collapse breccia* (B. Lønøy et al., 2019).

1.4.2 Major paleokarst reservoirs in the world

Some of the world's biggest of oil reservoirs such as the Yates field in west Texas, the Kirkuk oil field in North Iraq, the Grosmont heavy oil field in Canada, Ghawar field in Saudi Arabia, the Jiangbian gas field in China, and the Brazilian Presalt traps exhibit paleokarst features.

The Yates field in west Texas is very crucial paleokarst reservoir discovered in 1926 with a reserve of 5 billion barrels of oil. The reservoir consists of mainly Permian dolomite formation in the eastern compartment and high shale volumes in the western compartment with poor reservoir properties (Tinker & Mruk, 1995). Extensive karstification formed by mixing zone dissolution exists in the eastern part of the reservoir. The karstification phase resulted into a network maze geometry following the fractures and joint trends in the reservoir.

In Northern Iraq, the Kirkuk oil field discovered in 1927 is categorized as a fractured paleokarst carbonate reservoir. By 1980, the Kirkuk oil field had produced a cumulative of more than 9 billion barrels of oil (Trice, 2005). The reservoir consists of mainly limestone formed between the Eocene and the Oligocene. The limestone is composed of grainstones, rudstones and dolomitized skeletal fragments. Karstification and dissolution in the limestone formation developed as result of subaerial exposure and interaction with acidic meteoric flowing water along pre-existing fractures and joints (Daniel, 1954).

The Ghawar oil Field is a fractured carbonate reservoir discovered in 1948 and consists of the world's biggest conventional oil reserves. As of 2005, the daily production by water injection stood at 5 million barrels from the upper Jurassic Arab-D Formation (main pay zone) accounting to about a third of the cumulative oil production in Saudi Arabia (Afifi & Discovery, 2005). The high production rates are attributed to the excellent reservoir quality, existence of fractures in deeper tighter regions and the effective seal integrity due to lack of faults. The Arab-D Formation is dolomitic in nature consisting of three types of dolomites i.e fabric preserving dolomite (very fine crystals), non-fabric preserving dolomite (most dominant) and baroque dolomite (coarse and crystalline), Cantrell et al. (2004) . The non-fabric preserving dolomite extends over several kilometres of the Arab-D formation. It is heavily altered and consists of mainly intercrystalline porosity. The non-fabric preserving dolomite is associated with the Super K-zones (high permeability and productivity zones). The super K zones are a hypogenic karst system distributed throughout the reservoir area consisting of fractures, vugs, faults and with layers ranging from 10-20 feet (Dogru et al., 2001).

The Grosmont Formation in Alberta was discovered in 1952. It is a heavy oil paleokarst reservoir with reserves of up to 315 billion barrels (Dembicki & Machel, 1996). A shallow marine carbonate platform constitutes the depositional environment for the reservoir. Paleokarstic features in the reservoir of the carbonate platform were formed by severe karstification and dissolution. The porosity and permeability of the karstified formation is up to 40% and 30 D (Darcy unit), respectively. In some parts of the reservoir, poor porosity and permeability are present because of calcite precipitation (Dembicki & Machel, 1996).

The Jiangbian gas field is part of the Ordos sedimentary basin in China. The Jiangbian gas field, a lower Ordovician paleokarst reservoir was discovered in 1987 with initial gas reserves of up to 11 trillion cubic metres (J.-y. Li et al., 2008). The lithology in this reservoir are finely crystalline limestone, dolomite, and karst breccia. About 85% of the payzone is made of dolomite, porosities of up to 15% and maximum permeability of 1000 mD (J.-y. Li et al., 2008). The karsts breccia is associated with fractures in the reservoir and plays an important role in the gas flow behaviour. To the east of the gas field, karstification and dissolution is evident on several outcrops of the reservoir formation.

The most recent oil and gas discovery with paleokarstic characteristics is the Brazilian pre-salt that extends from the coast of Espírito Santo to Santa Catarina. Discovered in 2007, the Brazilian pre-salt is sedimentary basin infused with carbonates. In the Brazilian presalt, the main formations of importance are the Barra Velha and the the Itapema. The Barra Velha Formation is composed of microbial stromatolites, laminates, and shales while the Itapemea is made of calcareous conglomerates, mudstones, and carboniferous shales (Gaffney, 2010).

Paleokarst features do not only host oil or gas but can also be contain water resources, mineral deposits, and are potential geothermal reservoirs. Famous mineral deposits of paleokarst origin are the lead-zinc ore deposits in the Mississippi valley, USA (Sangster & Hillary, 1998).

1.4.3 Production and engineering challenges of paleokarst reservoirs

Paleokarst systems in carbonate reservoirs represent heterogeneity and zonation problems that enhance fluid flow in specific parts of the payzone. The fluids flow rates are several folds higher than the tight zones in the neighbourhood causing the injected fluids to have a preferred flow path, early water breakthrough and poor sweep efficiency.

Paleokarst features like cavities existing in multiple hydrocarbons, water and geothermal reservoirs are zones of high porosity and permeability that are associated with drilling problems. During production, a surge in porosity or permeability may results in borehole collapse or loss of tools while drilling.

Paleokarst features are very difficult to detect and characterize on seismic because of low seismic resolution.

Engineering problems such as sinkhole collapse are huge economic constraints and geohazards. Sinkhole collapse occur due to dissolution of host rocks proximal to the water table. As the rocks dissolve, the water table moves close to the surface causing the ground to sag and collapse inward (Frumkin et al., 2015).

1.5 Reservoir modelling and Simulation of Paleokarst reservoirs

Reservoir simulation is a branch of reservoir engineering where computer simulation systems are used to describe fluid flow in a reservoir (Peaceman, 1977). The computer simulation system is the reservoir simulator. There are several simulators used by academic institutes or the oil companies for example IMEX developed by Computer Modelling Group (CMG), ECLIPSE by Schlumberger and OPM Flow by the Open Porous Media Initiative (OPM). The reservoir model is the input data to the computer simulation systems. To prepare a reservoir model, an integration of contribution from different disciplines (Figure 1.5-1) is required and the reservoir simulator is the intersection of these disciplines. The modeler can filter and propose what to include and exclude from the reservoir model and seek consensus from other parties in different disciplines. Members from different disciplines should understand each other and be able to integrate aspects to come up with a common point of view.

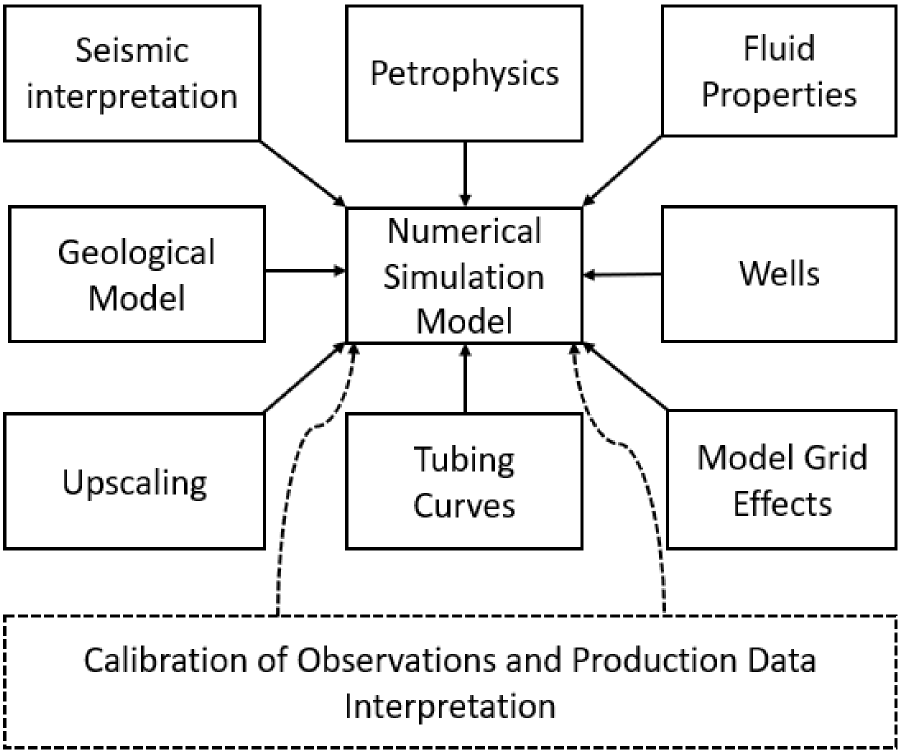

***Figure 1.5-1**: Integration from different disciplines to form a reservoir model (Haldorsen & Damsleth, 1993).*

Commercial simulators include a reservoir model, well model, wellbore model and a surface model. The fluid flow equations describing extraction of fluids from the reservoir or the injection of the fluids into the reservoir are defined by the well model. The wellbore model represents flow from the target pay zone to the surface while the surface model is associated with the surface facilities and separator conditions. The needs for simulating different scenarios may suggest using a different simulator. Most simulator assume constant temperature conditions (isothermal). However, if heat injection is involved for example, in the case of secondary oil recovery in heavy oil, waxy oil and the tar sands, then a simulator that considers temperature variations need to be used. STARS developed by CMG and ECLIPSE Thermal Simulator by Schlumberger accounts thermal processes.

1.5.1 Flow Simulation Equations

The flow equations used in each reservoir model depends on the flow regimes to be simulated, physical mass conservation laws and empirical relationships. To model flow, several equations are adopted depending on whether the media has open space or porous. Flow simulation is very demanding procedure involving mathematically creating flow grids and calculating flow behaviour and pressure gradients across the grids. An in-depth numerical mathematics of flow simulation is beyond the scope of this study, an overview of the commonly used flow equations is listed below:

The Darcy's equation

The Darcy's equation (Darcy, 1856) is the basic equation of flow describing fluid flow in a porous media. Porous media implies that the porosity of the domain of interest is less than unity. The flow regime in this scenario is defined by a Reynold number less than 1000 equating to laminar or slow flow rate. Darcy's equation (2) for a single phase:

$$q = \frac{-kA}{\mu L} dp , \tag{2}$$

where q= flow rate (sm^3/day), A=cross section area (m^2), μ=fluid viscosity (Pa. s), dp=pressure change (Pa), and L= length (m). The Darcy's equation is a simplified approach to model flow in karstic features; however, it might not give realistic fluid flow behaviour in the open space region. But it can perfectly describe flow in any porous media such as the non-cave facies.

Navier-Stokes Equation

The Navier-Stokes equation (3) was developed by Navier Stokes in 1822 to model flow of any fluid in existence. Galdi Giovanni, 2011 explained the mathematical theory of Navier stokes equation for steady state flow (Galdi, 2011). In principle, the equation is used to model fluids flowing fast in free flow region. In a free flow region, the porosity of the domain is unity:

$$\nabla p^{\varepsilon} - \mu\Delta \boldsymbol{v}^{\varepsilon} = \boldsymbol{f} \ in \ \boldsymbol{\Omega}^{f} , \tag{3}$$

where the physical parameters are defined as $\boldsymbol{\Omega}^{f}$ =free flow region, p^{ε}= fine scale pressure, ε=l/L, $\boldsymbol{v}^{\varepsilon}$ = permeability tensor, l and L are the length scales of both fine and coarse scales.

Stokes-Brinkman's equation

Brinkman established an equation that models fluid flow and capture transitional boundary layer effects between free flow fractures and porous regions (H. J. F. Brinkman, Turbulence, 1949). It is a combination of Navier-stokes equation and the Darcy's Equation. The Stokes-Brinkman's equation (4) [(Laptev, 2003) and (H. J. P. Brinkman, 1947)] is used to model single-phase flow that partially exhibit both free flow (***f***) and flow in porous media (***p***).

$$\mu \boldsymbol{K}^{-1} \boldsymbol{v}^{\varepsilon} + \nabla p^{\varepsilon} - \mu^{*} \Delta \boldsymbol{v}^{\varepsilon} = \boldsymbol{f} \ in \ \boldsymbol{\Omega} , \tag{4}$$

where, **K** is a permeability tensor, which is Ω^{p} is equivalent to the Darcy permeability of the porous media; μ is the physical viscosity, μ* is the effective viscosity and $\boldsymbol{v}^{\varepsilon}$ represents the actual physical velocity of the fluid and Darcy velocity in the porous region.

1.5.3 Upscaling of paleokarst reservoir properties

It is difficult to encounter an entirely homogeneous paleokarst carbonate reservoirs because they have a wide range of heterogeneities. Heterogeneities in reservoirs are multiscale and the factors entailing these scale transitions from the rock pore to the field reservoir model can be best presented on a logarithmic scale, (Ringrose & Bentley, 2015) , Table 1.5-1. Field reservoir models can consist of up to 10 million grid cells with a horizontal cell size of 50-100 m and vertical cell sizes of order 1-10m.

Table 1.5-1: *Dimensions used for crucial volumes in multi-scale reservoir modelling (**Ringrose & Bentley, 2015**).*

	X (m)	Y (m)	Z (m)	Volume (m³)	Reservoir volume fraction
Pore-scale model	5×10^{-5}	5×10^{-5}	5×10^{-5}	1.25×10^{-13}	0.00000005
Core plug sample	0.025	0.025	0.025	0.000031	0.00003
Well test volume	400	300	10	1,200,000	0.1
Reservoir model	8,000	4,000	40	1,280,000,000	1

Heterogeneous reservoirs consist of distinct layers, blocks, varying permeabilities in all direction. Therefore, to capture fluid flow of the entire reservoir or units of interest, averaging of permeabilities should be considered. The principle scales of upscaling are (i) Pore to lithofacies (ii) Lithofacies to geomodel (iii) Geomodel to reservoir simulator. Faults and fractures can also act as reservoir properties and maybe be incorporated at the geomodel scale using transmissibility multipliers. Porosity does not change significantly, thus simple averaging methods such as arithmetic averaging can be used. Permeability is averaged depending in how it was distributed as the rock was deposited. Three permeability averaging techniques were used to represent a homogenised system in the upscaled models.

Arithmetic permeability averaging

This is average absolute permeability that represents flow in parallel layered system from fine grid to a course grid. This method is best suited for horizontal flow as described by equation (5).

$$K_{arithmetic} = \frac{\sum_1^n t_i K_i}{\sum_1^n t_i}, \tag{5}$$

where K_i is the permeability of layer i and t_i is the thickness of layer i.

Harmonic permeability averaging

This is used to average lithologies where there is a significant vertical permeability and is described mathematically by equation (6).

$$K_{harmonic} = \left[\frac{\sum_1^n t_i / K_i}{\sum_1^n t_i}\right]^{-1}, \tag{6}$$

where K_i is the permeability of layer i, and t_i is the thickness of layer i

Geometric permeability averaging

Most heterogenous formations approximates flow properties of uniform formation with a permeability close to a geometric average as shown experimentally by Warren and Price (1961). Mathematically, it is defined by equation (7) as:

$$K_{geometric} = exp\left(\frac{\sum_1^n t_i l_n(k_i\ )}{\sum_1^n t_i}\right), \tag{7}$$

where l_n (K_i) is the logarithmic permeability of layer i, and t_i is the thickness of layer i.

Upscaling from geological model to a flow simulation model according to (Ringrose & Bentley, 2015) can also be done depending on the degree of complexity of representative elementary volume (REVs).

(i) Averaging of well data implicitly into the simulation grid: Small scale features and explicit reservoir property averaging is ignored. This approach simple, computationally cheap and is suitable for homogenous formations with less complexities or heterogeneities.

(ii) Single phase upscaling in the vertical direction: This approach is suitable for transforming geomodels into flow simulation model of the same grid domain in the horizontal direction (dx, dy). During upscaling, averaging of reservoir properties is done to ensure preservation of even the smallest features, thin layers or pinchouts.

(iii) Single phase upscaling in all directions: multiscale flow properties are estimated in all directions (x, y, z) using either full tensor or diagonal upscaling methodologies while ignoring multiphase flow effects.

(iv) Multiphase upscaling in all directions: This approach is used in large scale models to compute multiscale flow properties in all directions (x, y, z). The development of steady state solutions to multiphase flow has increased the use of this methodology. However, it represents expensive computation costs.

1.6 Previous work

Carbonate reservoirs that are paleokarstic in nature present a lot of heterogeneities and petrophysical complexities. This makes modelling and forecasting production scenarios very difficult. However, there are several methodologies to model, upscale and simulate production paleokarst reservoirs.

Nordli (2009) investigated the effect of breccia pipes on fluid flow behaviour in paleokarst reservoirs. In the study, it was postulated that highly permeable zones in the background act as thief zones resulting in poor sweep efficiency. Geological input to the reservoir models used by Nordli (2009) were based on Nordeide (2008). Nordeide (2008) used several properties of collapse breccia and their importance in the Wordiekammen formation (Billefjorden, Svalbard).

Furnée (2015) presented a procedure for modelling paleokarst reservoirs and the effect of collapsed cave radius by comparing production scenarios derived from fluid flow simulation. He tested traditional upscaling methods while minimising loss of details. In his study, the reservoir model was assumed to be a porous media. Reference curves were produced could be a benchmark for future simulation of both synthetic and real field paleokarst carbonate reservoirs.

To effectively capture and upscale reservoir properties, Popov et al. (2009) proposed a unified procedure of modelling and numerically simulating paleokarst carbonate reservoirs consisting of vugs and caves interconnected at multiple scale of fracture network using the Stokes-Brinkman's equation (3). The Stoke-Brinkman's equation permits inclusion of vugs or mega-karsts that are either fully porous or partly filled (free flow regions).

A recent relatively robust method called Embedded Karst Model (EDKM) developed by M. Correia et al. (2019) as continuation of a previous methodology (Embedded Discrete Fracture Model, EDFM) by Moinfar (2013). The EDFM does not represent karst volume and complex geometries. However, the EDKM allows inclusion of a representative volume through grid blocks of karsts and matrix modelled in different domains. This method greatly maintains resolution of the karstic elements in the coarser model and reduces the computing time by 95%.

2 METHODOLOGY

In this section, the methods and steps taken to achieve results presented in the section 3.

2.1 Workflow

An outline of the methodologies employed in the present study is given in the following:

- construction of reference generic paleokarst models accounting for varying karst geometries, sizes, and infill.
- assignment of cave and non-cave (matrix) properties in the respective generic model domains.
- upscaling (averaging and homogenization)
- Flow simulation of generated models
- Seismic modelling procedure
- Comparison of 4D seismic with flow simulation models

The workflow for the steps involved in the construction of generic paleokarst models are as follows (Figure 2.1-1):

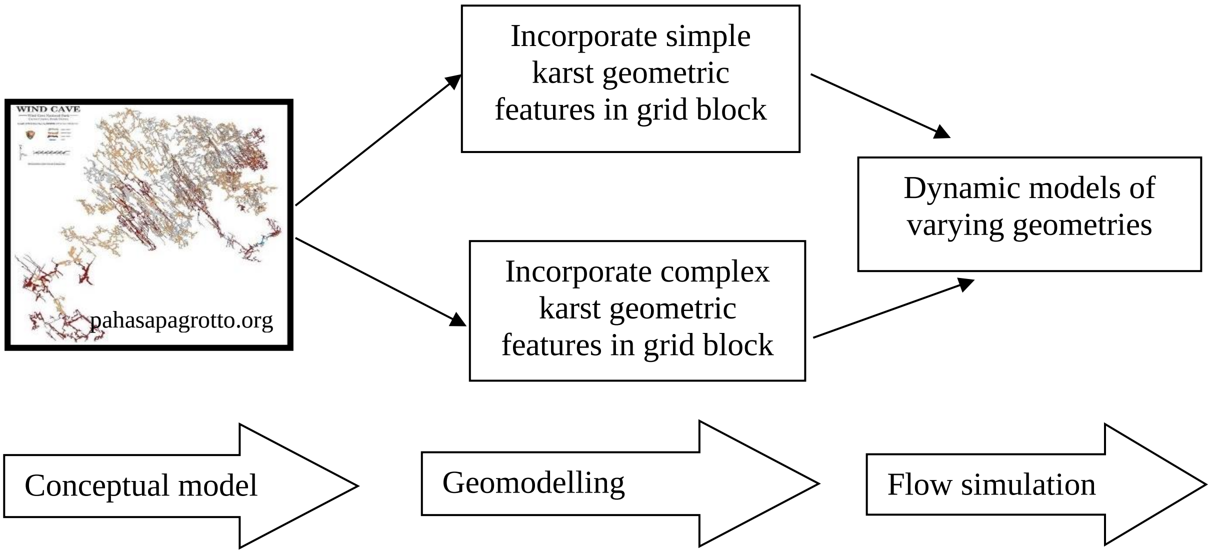

Figure 2.1-1: *Workflow for methodology used to construct of generic paleokarst models.*

2.2 Grid Construction

Different methodology for modelling exists but are cumbersome and require a lot of work. (Furnée, 2015) presented a methodology of creating polygons to construct a cave geometry using mapped survey points from Setergrotta cave (Mo I Rana, Norway). This section gives an overview of a quick and simplified cave geometry construction from conceptual model using an excel layout in 2D and creating an Eclipse data files to build the cave floor, roof and the overburden in 3D by adding a layers in the z-direction (depth).

2.2.1 2D Paleokarst skeleton

The initial step of my work started with creating a generic grid from scratch using excel and then defining the grid geometry and petrophysical properties in text files (.DATA Files). The text files were then imported and run in a numerical flow simulator. The characters in the text files were at most 126 characters per line because it is the maximum the simulator can read. The initial dimension of the 2D grid model is 614 m x 100 m x 30 m with a 2 m x 2 m x 2m cell size giving a total of 230,250 cells for both the simple and complex geometries. Numerical values 1 and 2 were assigned to the matrix and the karst domains, respectively. The 2D skeleton (Figure 2.2-1) is purely generic capturing different cave geometries and many branching passages. Cross sectional diameters of 2,6,10,14, and 18 m were used in the different cave segments. Fractures or faults were initially excluded because the aim of the study is to understand flow behaviour in caves only. The excel 2D skeleton is then converted to a text file for further construction procedure of adding layers and converting it to a 3D geomodel.

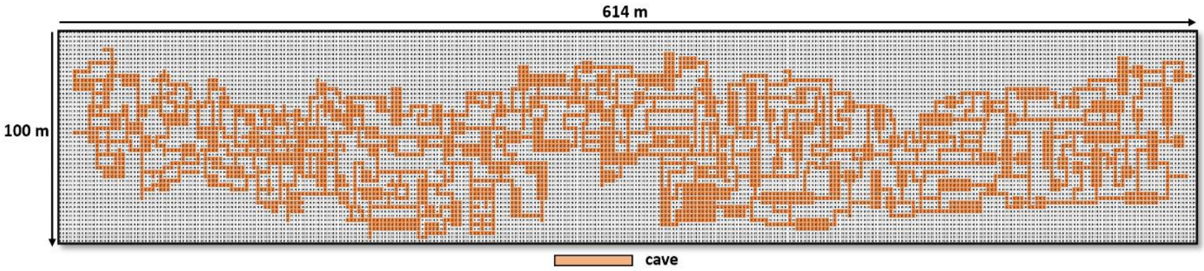

Figure 2.2-1: *2D cave geometry (orange) constructed in excel based on conceptual models.*

2.3 Geomodelling

2.3.1 Construction of 3D paleokarst geomodels

A further step to convert the 2D paleokarst reservoir skeleton into 3D geomodel was initiated. First by assuming the 2D skeleton from excel as the layout for the central layer and then adding more layers above and below to a total of 15 layers. The 15 layers are an equivalent of 30 m with karsts of up to 18 m. The top two layers and the bottom two layers have only matrix while the rest of the layers contain both karst and matrix. Both the simple and complex generic models measured 614 x 100 x 30 m (x, y, z) and are filled with porous media in two grid domains consisting of both the matrix and the karstic features. The model consists of 15 layers with layer 8 as the central layer. Layer 8 is the line of symmetry through the centres of all caves. The geometry and shape of all caves is imprinted on the surface of the central layer. The diameters of caves greater than 2 metres increase vertically and downwards and are all centred about the line of symmetry (layer 8). All the 2 metres are contained in the layer 8. To closely approximately the diameter and shape of caves passages, a regular grid consisting of uniform square cells was adopted, Figure 2.3-1(a-b).

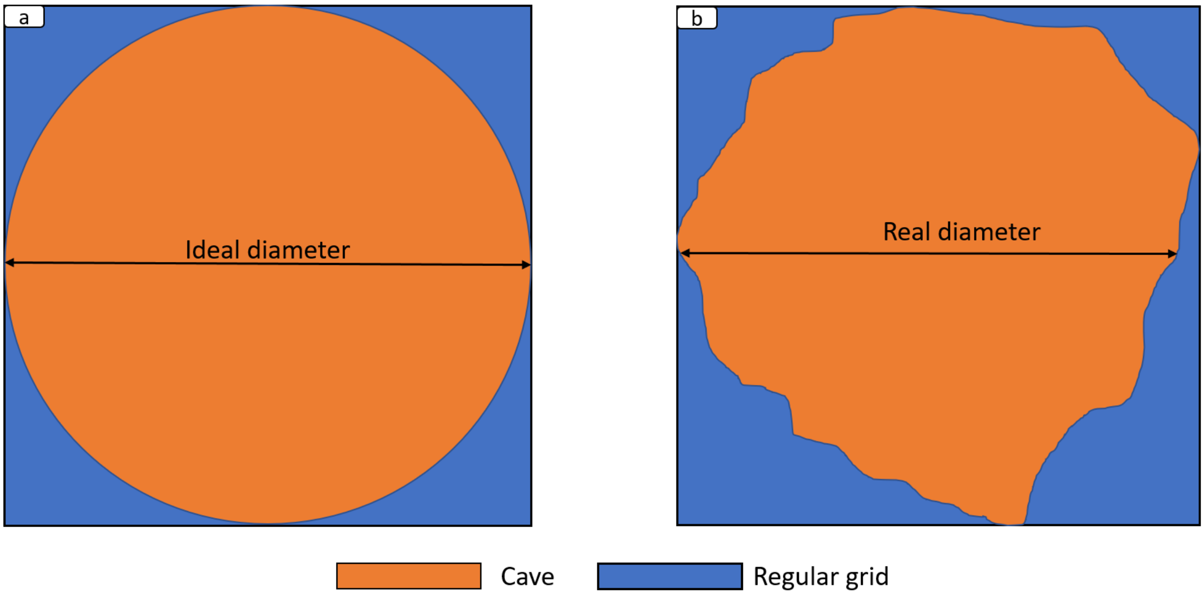

Figure 2.3-1*: a comparison of cave geometries (a) an ideal circular cave geometry (orange) a uniform diameter perfectly inscribed by the grid (blue) (b) a conceptual model of what a real cave may look like (orange) inscribed by a regular grid (blue).*

All lengths of the grid sides are equivalent to the diameter of the inscribed cave in Figure 2.3-1 (a). However, most of the cave passages are not perfectly circular or spherical approximating the geometry described in Figure 2.3-1 (b). The diameter of the mapped cave survey points will not be the same as the length of the grid. Similar grid block sizes (2x2x2 m^3) are used for both the matrix and karst domain making the model structured and easier to use in a commercial simulator. A description of the models and their respective input parameters are shown in Table.2.3-1**.**

Table 2.3-1: *Input parameters for generic paleokarst models.*

Model Name	**Dimensions**	**Lithology**	**Petrophysical properties**	**Geometry**	**Dominate passages**
Complex generic paleokarst model	Model size • 614x100x30 m • 2x2x2 m block size	• Collapse breccia • Matrix	High K (1000 mD) Low K (0.1 mD) high Ø=20%, low Ø=2%	Network maze with many branching passages.	2-6 m (majority) with few >6m passages.
Simple generic paleokarst model	• 614x100x30 m • 2x2x2 m block size	• Collapse breccia • Matrix	High K (1000 mD) Low K (0.1 mD) high Ø=20%, low Ø=2%	Few branches and simplified geometry.	>6 m (majority) with few small passages.
Simplified Infill karst model	• 614x100x30 m • 2x2x2 m block size	• Collapse breccia • Clastics (sand) • Matrix	High K(2200mD), moderate K (350mD,Kz=35mD), low K=0.1mD high Ø=20-25%, low Ø=2%	Few branches and simplified geometry.	>6 m (majority) with few small passages.

Two geomodels were inherited from the base model. One having a very complex geometry [Figure 2.3-2(a)] and the other consisting of a very simple geometry [Figure 2.3-2(a)]. The third model is inherited from the simple geometry geomodel by assigning different petrophysical properties in the karst domain to represent sediment infill (clastic sediments and collapse breccia). see Figure 3.1-25 in the results and discussion section.

Figure 2.3-2: *a comparison of cave geometries (a) complex generic karst model (b) simple generic karst model.*

2.3.2 Petrophysical and rock model

The petrophysical and rock model was built in 15 layers with alternating zones of low and high permeability. Because of computational costs, multi-scale features and limitation of data, homogenization of rock properties rather than detailed property assignment was used to describe effective properties in the simulation block. High porosity and high permeability values were assigned for the cave domain while low porosity and low permeability values were assigned for the non-cave domain. Flow is solved using the Darcy's equation by averaging properties (porosity and permeability) for both the matrix and karst domains. This is done explicitly by the commercial simulator. In this study, ECLIPSE 100 a schlumberger simulation software was used. The MULTNUM Keyword, the values 1 and 2 adopted to represent non-cave facies cells and the cave facies cells, respectively. And to populate the cells with petrophysical properties, the keyword MULTIREG was used. Precaution should be taken not to assign a value less than 1 for example 0 if you are using ECLIPSE E300. Any numerical value greater than 0 is recommendable for region definition with ECLIPSE E100. The non-cave petrophysics properties were assigned for the entire porosity (PORO) and permeability values (PERMX, PERMY, and PERMZ) for the entire grid. Using the MULTIREG key word, multipliers were used to overwrite and populate region 2 (cave) with higher values to distinguish it from the non-cave. The petrophysical properties of the cave segment were multiples of the non-cave region. This method allows definition of new petrophysical properties to be done fast and only in the ECLIPSE data File and nothing must be changed in the MULTNUM include files.

2.3.3 Upscaling strategy for fluid flow simulation

Non-selective homogenization by averaging properties in both cave and the non-cave facies rescaling. This is done explicitly by a commercial reservoir modelling software (Roxar, 2018). The mathematical expressions for averaging methodologies used in the upscaling process are discussed in the introduction section. Arithmetic averaging was employed for obtaining effective porosity for the output grid cells. The output value is an upper limit for a given cell parameter in any given direction. Diagonal tensor, harmonic geometric and harmonic averaging were used to compute effective permeability. Diagonal tensor rescaling outputs an estimate of diagonal permeability components principal to 4 directions. Harmonic averaging is a lower bound for effective permeability in any given direction. Geometric averaging yields a lower effective output grid cell value than the arithmetic average for the same input values. Important to note is that the choice of rescaling for permeability does not affect the end results as much. The full tensor rescaling (six directional permeabilities) methodology was excluded because eclipse only handles up to four directional (diagonal) permeabilities. See more on upscaling in results and discussions section.

2.3.4 Flow based simulation using Eclipse

Flow simulation of both the reference model (geological model) and coarser models is done using ECLIPSE E100 commercial simulator. Since emphasis is mainly on the flow pattern in cave section with varying diameter and geometry, RESINSIGHT software is used for high resolution visualization. The most important items used in the data file input (***Appendix 3***) to the flow simulation model contained the following sections:

RUNSPEC

The RUNSPEC section specifies model's title and dimensions, field units (metric), phases, reservoir compartments, linear solvers, messages, and the start date of the simulation. Water and oil phases were included in the system, and the start date set at 01.01.2019. The CPR (constrained pressure residue) linear solver rather the default Eclipse Linear solver was used to reduce CPU costs and avoid linear convergence problem. The NSTACK (Linear solver size) which is the same as the LITMAX was set to 58 and the a NUPCOL of 10 rather the default (3) to limit convergence problems. The print limit for the message was set to 1000 and the stop limit at 100,000 severities.

GRID

The grid section is composed of dimensions, length, tops, NNCs, petrophysics and grid orientation (GDORIENT). In this section, The COPYREG, MULTNUM and MULTIREG keywords were introduced with the purpose of populating the grid cells with reservoir flow properties like porosity, permeability, and transmissivity. The MULTNUM is used assigns region numbers to specify the matrix and karst cells separately. The assigned cell number must be greater than 0. The MULTIREG keyword is used to populate regions defined by MULTNUM with petrophysics (permeability and porosity) as a multiplier of the dual porosity or permeability values. The COPYREG keyword is used to copy petrophysics from one region to another in the same model. The GDORIENT is used to make the Z-direction is consistent with grid geometry specified and to verify whether the input properties are in an increasing or decreasing order. This keyword is important in situations where the reservoir is to be oriented either below or above sea level during simulation.

EDIT

This is an optional section containing guidelines for modifying diffusivities, block centre depth, transmissibilities, pore volumes and non-neighbour connections (NNCs). The keywords in this section are DEPTH, PORV, TRAN (X, Y, Z, R, THT), DIFF (X, Y, Z) and DIFF (R, THT). The keywords can be used to replace data for an entire reservoir or specific regions of interest using the BOX keyword. Multipliers keywords can also be used in this section.

PROPS

This section defines rock and fluid properties such as rock compressibility, viscosity, surface density, dissolved fluids at reservoir conditions. Constant values are used throughout all the simulations in this thesis. More of the details on the fluid properties are included in ***Appendix 3.***

REGIONS

To explicitly understand flow patterns in specific karst geometry, the REGIONS section was introduced. A total of 70 user defined regions was used. Region 1 and 2 were the default regions defined by the MULTNUM keyword. To inherit properties and create new flux regions, the keyword FIPNUM was used. FIPNUM is a user defined quantity.

SOLUTION

This section describes model initialization and equilibration. Equilibration data is defined using EQUIL keyword. In this thesis, the datum depth was set at 1515 m corresponding to the depth of the central layer of the reservoir for better calculation and the oil water contact set so that reservoir with entirely filed with oil.

SUMMARY

The summary section specifies results to report after simulation. This includes total field oil production (FOPR), production rates (FOPR), watercut (FWCT), injection rates, reservoir pressure and so on. To understand contributions and fluid flow behaviour from different regions of interest defined in the REGIONS section, data from these regions was requested. This was done by adding R at the start of the default keyword and then specifying the region numbers.

SCHEDULE

In this section, production and injection scenarios are specified. The keyword COMPDAT describes the type of wells to be used, their target depth, state, penetration direction. For most of the models, horizontal wells INJ1 and PROD1 were used to respectively inject water and produce oil. Vertical wells were used only in 5-spot well models to analyse sensitivities. The wells (an injector and a producer) were placed in the central layer across the entire reservoir width. Positioning of the wells was in three scenarios: (i) Outside the cave (ii) inside the cave only (iii) both in cave and non-cave region. The keywords WCONPROD and WCONINJE specifies rates, fluids produced or injected and the state of the producer or injector, respectively. To maintain a nearly constant reservoir pressure during production, keywords GCONINJE and VREP are introduced. This creates a bottom hole pressure at the injector that adjusts relative to an increase or decrease in the average field reservoir pressure. The DATES keyword defines timesteps at which production reports are printed throughout the lifetime of the field. The time steps were set at 6 months and a production time of 26.5 years up to 46.5 years in some models.

2.3.5 Defining Regions of Interest

One of the aims of this study is to do a sensitivity analysis on how pressure, saturation, and flow flux change in the different segments of the cave.

i) Complex generic paleokarst model

A total of 33 regions with different geometry and diameters were defined. The FIPNUM KEYWORD was used to define the cave and non-cave regions while the FIPCAVE (User Defined Quantity) explicitly defined only regions of interest where the sensitivity analysis was to be done.

ii) Simple generic paleokarst model

The basis of construction is based on simplicity. This is done by including many bigger karst channels between 6 metres and 18 metres with only a 2 metres channel. Branching networks were also excluded from the model.

2.3.6 Reducing simulation run time

One of the challenges I initially faced was that the models took a lot of time to run because of the complexity and geometry associated with paleokarst reservoirs. Using trial and error to come up with smooth and fast runs with less severity by tuning parameters and timesteps did not help. Rather including the CPR (Constrained Pressure Residue) keyword in the RUNSPEC section greatly reduced the run time by about 95%. The CPR linear solver uses a two-step preconditioning that extracts and solves a pressure equation at each iteration and then uses the sum of the two steps to approximate a solution.

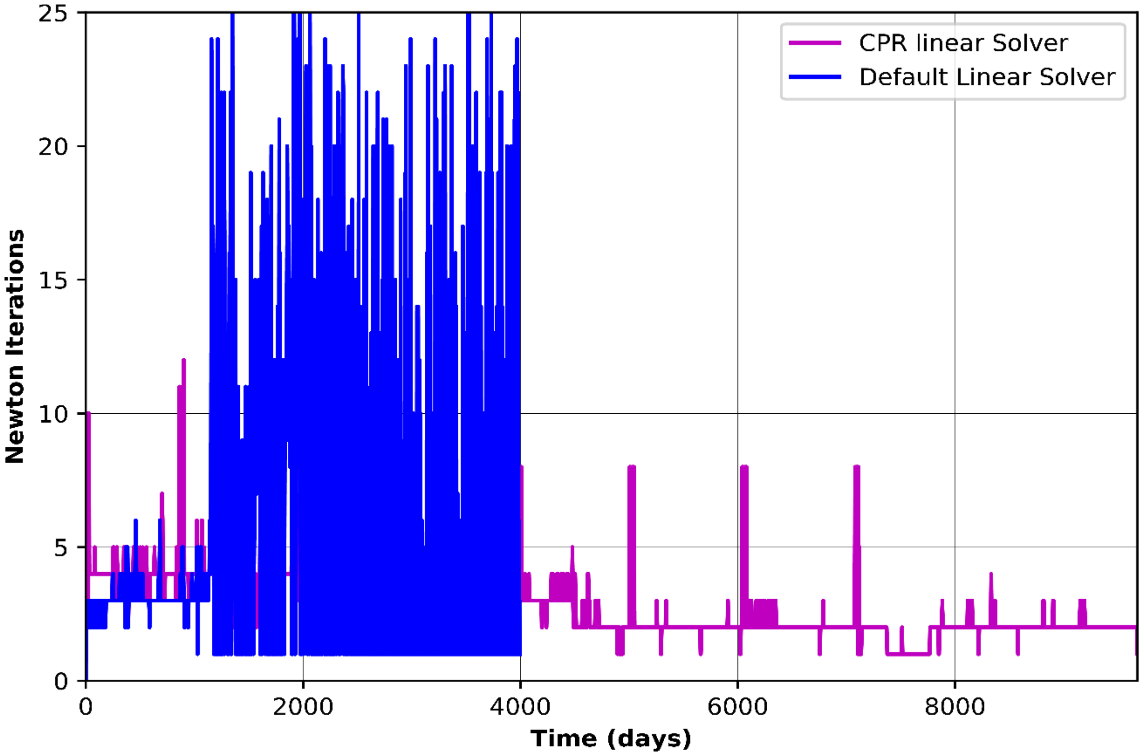

***Figure 2.3-3**: Comparison between CPR linear Solver (Magenta) and the default Eclipse linear solver (Blue) based on number of Newton iterations achieved during flow simulation of a complex generic paleokarst model.*

The flow simulation for the complex generic paleokarst model using the default linear solver terminates after 4044.7 days of production due to linear convergence failure on the last iteration and linear convergence problems (Figure 2.3-3).

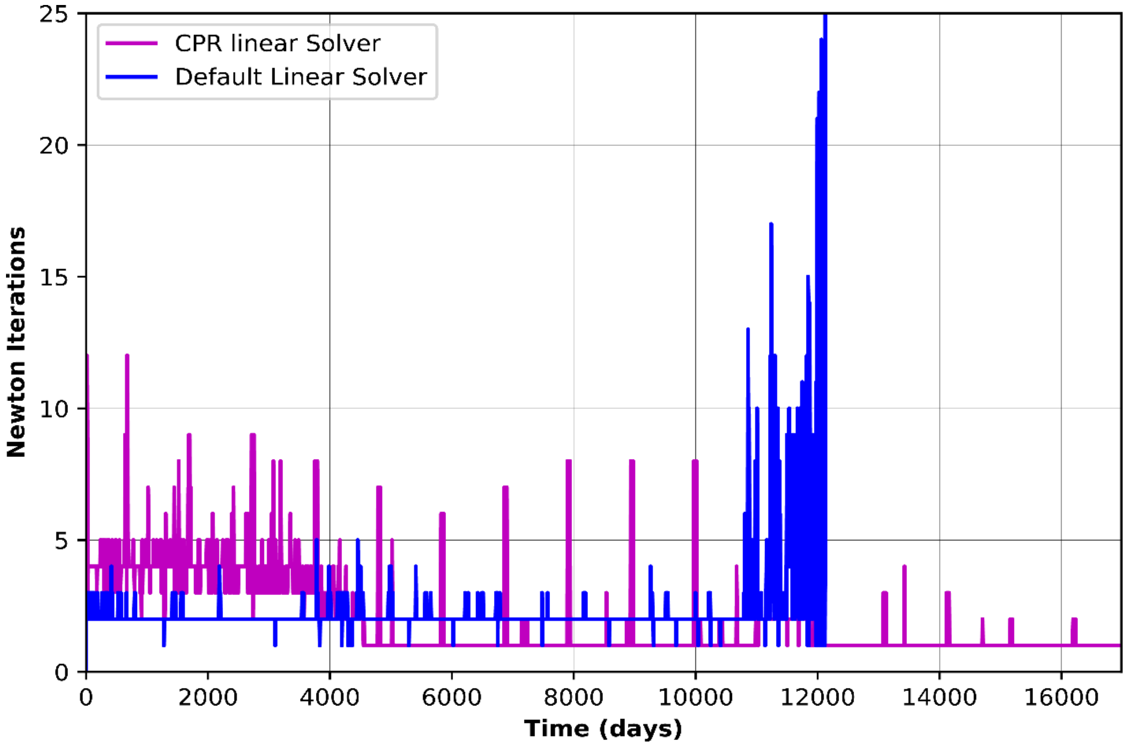

***Figure 2.3-4**: Comparison between CPR linear Solver (Magenta) and the default Eclipse linear solver (Blue) based on number of Newton iterations achieved per time-step during flow simulation of the simple generic paleokarst model.*

The flow simulation for the simple generic model using the default linear solver runs smoothly before terminating at 12126.7 days of production due to linear equation convergence problems (Figure 2.3-4). Using the CPR linear solver, the number of iterations greatly reduced from over 20 to about 4 per time-step, and to less than 3 per timestep with the default Eclipse solver. All the runs ended without linear convergency problems or iteration problems. The comparison of computation times (TCPU) in (Table 2.3-2) further reveals the advantage of using CPR linear solver over the default linear solver. The CPR linear solver works best for the complex generic paleokarst model while the default linear solver produces the least computation time with the simple generic paleokarst model The CPR linear solver should therefore be adopted for karst models with very complex geometry for least computation time. The run times were achieved on a computer with a 3.30 GHz dual processor and 64 GB RAM.

Table 2.3-2: CPU times achieved with different linear solvers.

Model	CPR Linear solver	Default Linear Solver
Simple generic paleokarst model	15862.64 s	17214.25 s
Complex generic paleokarst model	20892.97 s	17678.31 s*

*run terminates prematurely due to linear convergence problems.

2.4 NOTEPAD++

The process of creating data files for flow simulation is very time consuming, mundane, and very prone to errors. Notepad++ a text editing software provided a fast and easier way to find and replace characters in data files simultaneously.

2.5 Visualizations of simulation outputs

To visualize the outputs of the simulation results, a commercial simulator and an open source visualization platform called RESINSIGHT were used. RESINSIGHT is an open source software developed under the Open Porous Media initiative (OPM) supported by Equinor AS and other partners. It works on both Linux and windows operating systems reading the Eclipse binary format faster. The fact that it is an open source software allows flexibility to look at results at any time on any type of personal computer and from anywhere. I preferred the RESINSIGHT software because of the freedom to view, zoom, rotate, and export plots and snapshots of regions of interest while maintaining high resolution graphics and images.

2.6 Fracture Modelling

Fractures are introduced in the generic paleokarst models to assess their influence on the overall flow pattern in the presence of karsts. Paleokarst carbonate reservoirs are heavily fractured with vugs of varying sizes and distributions. Therefore, to create a realistic fractured generic paleokarst model two fracture trends (vertical and horizontal directions) are put in every layer (Figure 2.6-1). The assignment of fractures is stochastically and explicitly done by a commercial modelling software. Karsts that are connected are in away linked to the global fracture network by small scale fissures according to (Jennings Jr & Lucia, 2001).

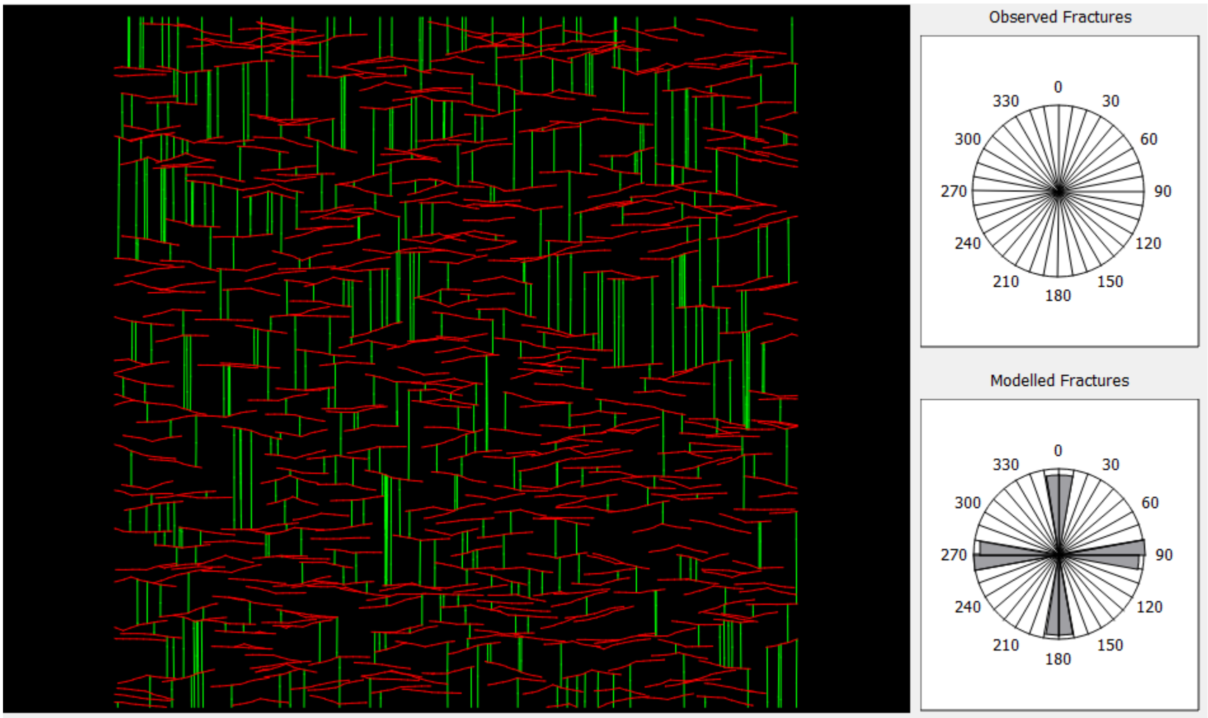

Figure 2.6-1: *Fractures sets in the central layer generated stochastically. The green lines are the vertical fracture sets (Frac_vertical) while the red lines (Frac_horizontal) are mainly horizontal fractures.*

The main fracture directions are either vertical or horizontal in agreement with the all cave passages modelled. The horizontal fractures are parallel to the flow direction and the pressure gradient while the vertical fractures are perpendicular to both the flow direction and the pressure gradient. Inter-porosity transfer of fluids between fractures and the pore system depends on permeability and the degree of fissuring assuming that the fracture porosity is less than the porosity of the entire pore system (Barenblatt et al., 1960). The fine scale fractured paleokarst model has triple porosity and permeability consisting of matrix, fractures, and karst porosity. In the fracture sets, fracture porosity is created using a dual-porosity option in the RMS software. The input parameters used are the same as those specified in Table 2.6-1. At this stage, the fracture permeability only in the x and y direction is generated in each layer and the z-direction permeability tensor is the permeability (Kz) of the host matrix. There is no definitive manner to specifically assign a z-direction permeability in the RMS Software. This may cause to some extent the underestimation of the vertical permeability (PERMZ). However, the flow direction is mainly in the horizontal direction (dx) of the grid, therefore the vertical permeability may have less influence on the fluid flow pattern in the cave passages. Fractures oriented parallel to the flow direction tend to have a high oil recovery than those normal to the flow direction (Gao et al., 2017)

Table 2.6-1: *Input parameters to a fracture model used to populate the generic model with fractures.*

Fracture set	Orientation (degrees)	Orientation variability	Density (fracture/m)	Length (m)	Length variability	Fracture thickness
Frac_hor	0	5	50	50	5	1
Frac_vert	90	5	50	50	5	1

Default RMS input parameters used include: Aperture (50 µm), Stiffness (0.8), Thickness (1), thickness variability (0) and a truncation probability of 1. The attributes used in modelling of each fracture set are described by ROXAR RMS 11.0.1 release notes as follows:

- Density: This parameter specifies the trend of the fracture density in each grid cell as a multiplicative inverse of the fracture length.

- Orientation: Defines the orientation of fracture trends in each grid cell measured in degrees. For instance, a value of 90 degrees means that the fracture sets are oriented in the vertical direction and 0 degrees will imply that the fractures are oriented in the horizontal direction.

- Orientation variability: This parameter defines a standard deviation of the fracture set orientation distribution.

- Length: This is a parameter that defines an average horizontal length of a specified fracture set. Length will typically 1-1000 metres.

- Length variability: this parameter defines the distribution of a specific fracture set.

- Fracture aperture: This a measure of the distance the walls of the fractures in the fracture set measured in microns (µm). The Fracture aperture is very important when using Discrete Fracture Network modelling. Discrete Fracture Network is an explicit network of individual fractures.

- Stiffness: This is a dimensionless parameter between zero and unity that controls the shape of the fractures as they grow in the modelling algorithm. A value of 0 causes the fracture to follow the orientation trend as it propagates from cell to cell whereas a value of 1 causes the fractures to propagate in a straight line.

- Thickness: Values between 1 and the total number of grid layers traversed by fractures in a specified set.

- Thickness variability: This is a measure of grid layers defining the thickness of fracture set distribution.

- Truncation probability: This is a value ranging from 0 to 1 used to control truncation between fractures belonging to alternative set. A value of zero means that fractures in each set will always cross other fractures whereas a value of unity will cause fractures to just stop at other fractures.

2.7 4D seismic modelling

4D seismic modelling of paleokarst reservoir is done to monitor changes in dynamic properties in the reservoir during or after production. The methodology employed to map 4D seismic anomalies is discussed in section 3.3.

3 RESULTS AND DISCUSION

In this section results from dynamic flow simulation, upscaling, synthetic seismic modelling, and fracture modelling of paleokarst models with different cave geometries are discussed.

3.1 Sensitivities of Paleokarst

This sub-section addresses sensitivities in paleokarst based on observation from varying geometries, petrophysics, flux rates, well patterns, and karst (cave) sizes, and their influence on oil production. The reservoir is filled with oil and secondary water injection is adopted to flood and improve recovery rates.

3.1.1 Sensitivity to varying cave geometries

Flow simulation was performed on two base models with the same average reservoir properties and production rates, but different geometric configuration described in Table 2.3.1 and Figure 2.3-2. In Figure 3.1-1(a &b), the model comprises of a complex geometry having a lot of branching, maze like networks and a lot of small sized passages. The flow pattern of the water flood initially follows the cave geometry, with a very homogeneous waterfront. However, the short separation length between individual cave conduits causes a high-pressure gradient in the direction of flow leading to flux into the non-cave regions at the branching nodes of the cave passages.

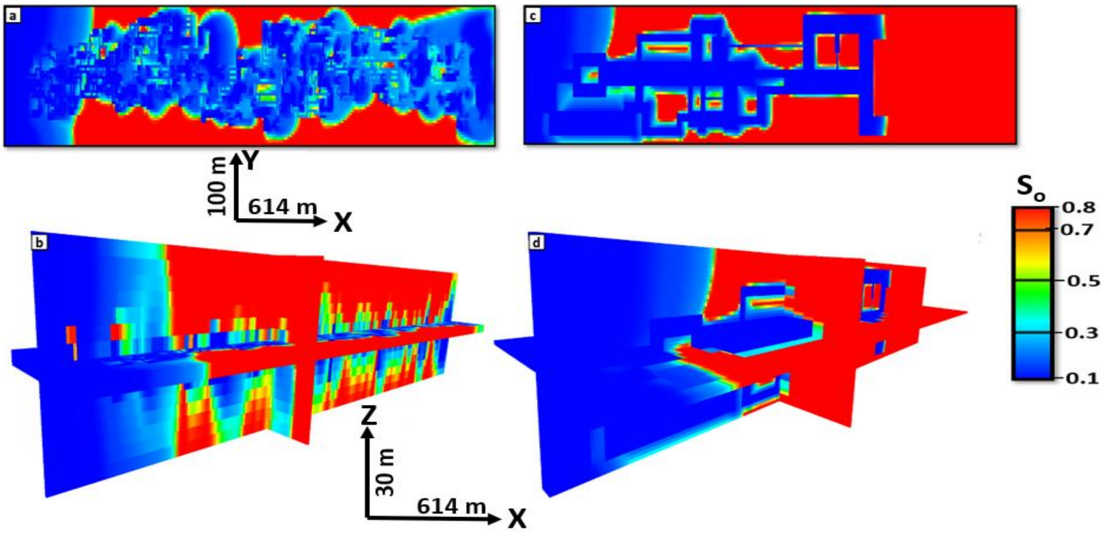

Figure 3.1-1: *Oil saturation plots of paleokarst models with varying geometries displaying (a) flow patterns and waterflood front (blue) in the central layer of a complex cave geometry and the (b) corresponding 3D planar view (c) flow patterns and waterflood front (blue) in the central layer of the simple cave geometry, and the (d) corresponding 3D planar view.*

In Figure 3.1-1(c&d), the geometric configuration of the model is simple with less branching and small sized cave passages. Most of the cave conduits are greater than 6 m in diameter. The flow pattern mainly follows the cave geometry at a much slower rate than the model with complex geometry. The slow flow rate of displacement is evidently shown by the different position of the water flood (in blue) in the oil saturation plots [Figure 3-1-1(a-d)] taken at similar injection time lapse. Flooding of the non-cave region is very minimal because the large separation length between the cave conduits resulting into a low-pressure gradient in the direction of fluid flow.

The flow behaviour of the injected fluids in both the fine scale version of the simple and the complex models during production were also visualized by performing streamline simulations. For simplicity vertical wells were used to inject and produce the reservoirs in the two cases as shown in Figure 3.1-2. From the streamline simulation, it is observed that the flow streamlines are mainly concentrated and denser in the cave region than in the non-cave region. The fluid flow preference to the cave geometry is attributed to the huge permeability contrasts between the cave facies and the non-cave facies. The contrast in permeability causes the fluids the fluid to move across in regions of the highest permeability irrespective of the complexity of the cave geometry. It should be observed that the streams close to the wells tend to spread across the entire reservoir to the edge in both cases. These edge effects may be attributed to software artefacts or the large pressure build up proximal to the wells.

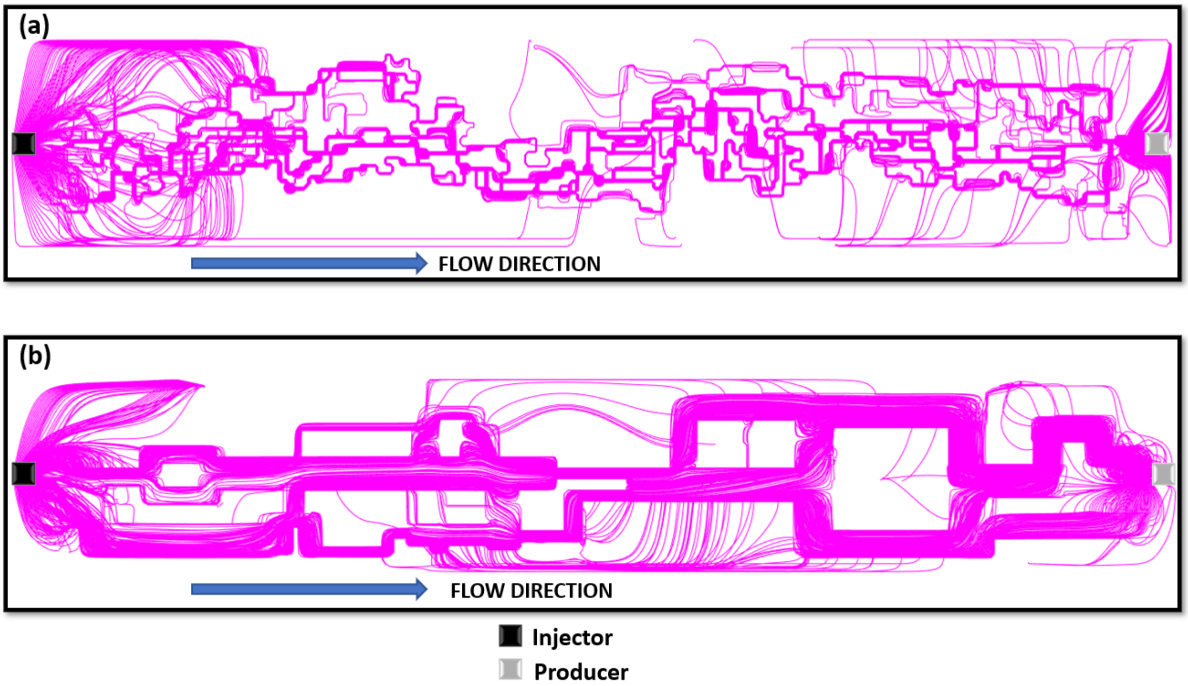

Figure 3.1-2*: Streamline simulations (in pink) on cave models displaying (a) flow patterns across the entire complex cave geometry (b) flow patterns across the entire simple cave geometry.*

3.1.2 Sensitivity to varying cave sizes

Caves (karsts) and fracture cavities in carbonates are of different sizes and diameters. Fluid flow may vary depending on gravity segregation, karst diameter and the size of contributing conduits. To understand fluid flow behaviour in karsts of varying sizes, oil saturation plots from the bottom, centre, and top of having diameters of 6 m, 10 m, and 18 m are compared. The diameters of the karsts are designed so that they greatly exceed the dimensions of the pore system. This is done so that the permeability of the karst is greater than that of the matrix. Regions of interest in the base model (complex generic cave model) are defined and the oil saturation in the bottom, central and top layers are compared to quantify sweep efficiency through the entire karst height (Figure 3.1-3).

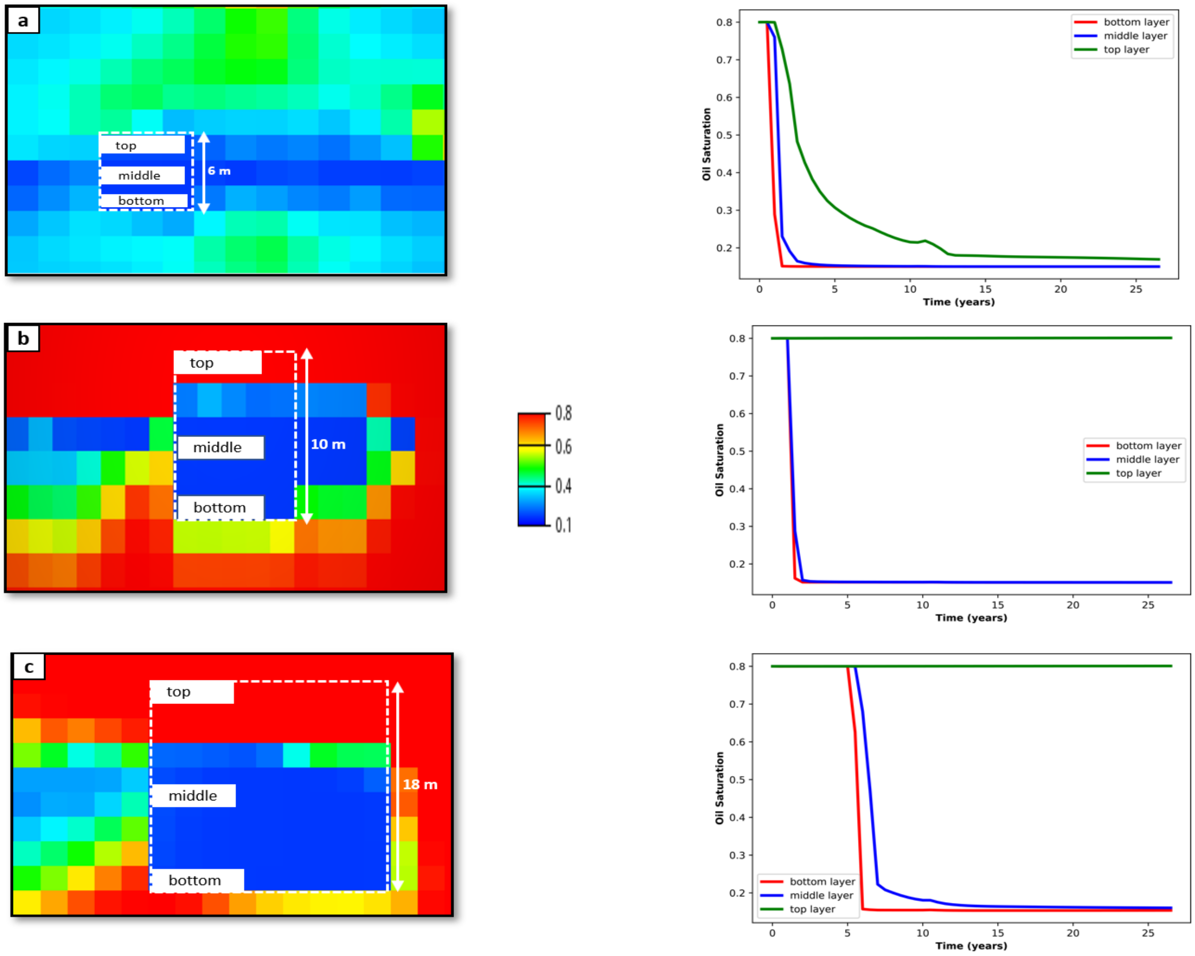

Figure 3.1-3*: Oil saturation plots (left) and saturation plots (right) showing (a) 6 metre cave (b) 10 metre cave (c) 18 metre cave.*

In the 6 m cave (Figure 3-1-3), there is a nearly perfect sweep in the bottom and the central layer while better sweep with less oil trapping is observed in the top-most layer. However, in the 10 m and 18 m karsts [Figure 3-1-3(b-c)], excellent oil sweep exist bottom most and the central layer while the topmost layers are left un-swept contributing to much of the trapped oil left behind after production. The sweep efficiency is quantified by the reduction of oil saturation with increase in time of water flooding or oil production. These observations show that oil recovery reduces with increase in the karst height possibly attributed to gravity becoming a dominant force influencing fluid flow. In addition, the inability of the water flood to displace and produce oil at the topmost karst height due to uncertain flow behaviour suggests the need to implement other secondary or tertiary recovery methodologies. (Wang & Sun, 2019) suggested the use of cyclic water huff and puff to significantly improve oil recovery in karsts. However, an excellent residual oil recovery using this method is limited by; heterogeneities, multi-scale range of fractured-vuggy features, flow behaviours, water oil interaction problems and rapid water breakthrough during water injection. The N_2 flooding oil recovery technique possesses better results because of its minimum miscibility pressure with the trapped oil, swelling abilities, and pressure distribution high enough to alter its flow pattern to reach even the topmost cave layers (J. y. Li et al., 2008).

3.1.3 Sensitivity to increasing matrix permeability

It is suggested that lack of vertical permeability barriers (Kx=Ky=Kz) and high permeability matrix results into increase in oil recovery and early watercut in paleokarst simulation models (Pantou, 2014). Therefore, to study sensitivities resulting from permeable matrix in paleokarst reservoir during production, a total of 23 flow simulations were performed on both the simple and complex models by varying the permeability of the background matrix (non-cave facies) in an increasing steps of between 0 to 100 mD while the karst permeability was unchanged (1000 mD). When the simulation results were visualized, interesting flow patterns were observed at non-cave permeabilities (background matrix) of 10 mD, 20 mD, 30 mD and 40 mD. The criterion of choice is based on when the fluids starts to prefer to flow in both the cave and the non-cave regions. At 0.1 mD, the flow pattern follows the cave geometry and the water flood front is very homogeneous with the cave and minimal flow into the matrix. The non-cave facies have low permeability and less storage capacity thus there is minimal flux from approaching waterfront. The displacing water flood instead prefers flowing into the more permeable cave facies with easy leaving a pronounced flow patten, Figure 3.1-4 (in blue). The cave geometry can be retraced when the simulation run is paused at a specific timestep especially in the central layer of the payzone. At the top of the cave system, the water flood is less pronounced than at the bottom because of difference in gravitation forces and viscous forces. Comparable results are observed in the Ordovician reservoir unit of the Tahe oil field in china between rock matrix of permeability between 0.1 mD and 1 mD, large karsts and fractures (Zheng et al., 2010).

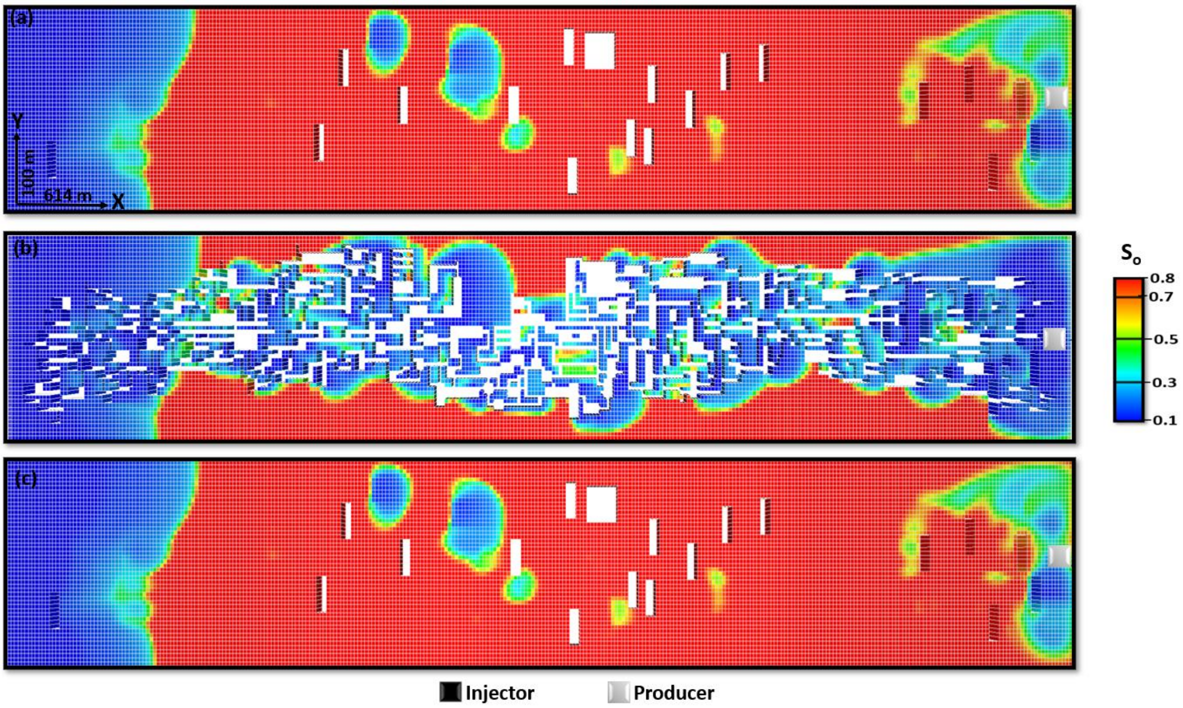

***Figure 3.1-4**: A horizontal section of the complex paleokarst flow simulation model showing oil saturation at 0.1 mD matrix permeability of the (a) top-most layer of the cave system (b) central layer of the cave system (c) bottom-most layer of the cave system.*

At 10 mD, the water flood invades parts of the non-cave region and its flow path starts to deviate from the cave geometry (Figure 1.3-5 and Figure 1.3-6). This is because the increase in the non-cave matrix permeability reduces the resistance of the formation to incoming waterflood thus displacing the some of the oil in the pores. The shape of the approaching waterfront is not linear across the reservoir and cave geometry cannot be fully reconstructed when the simulation visualisation is paused. This happens regardless of geometric complexities and the flow path is mainly in the cave facies.

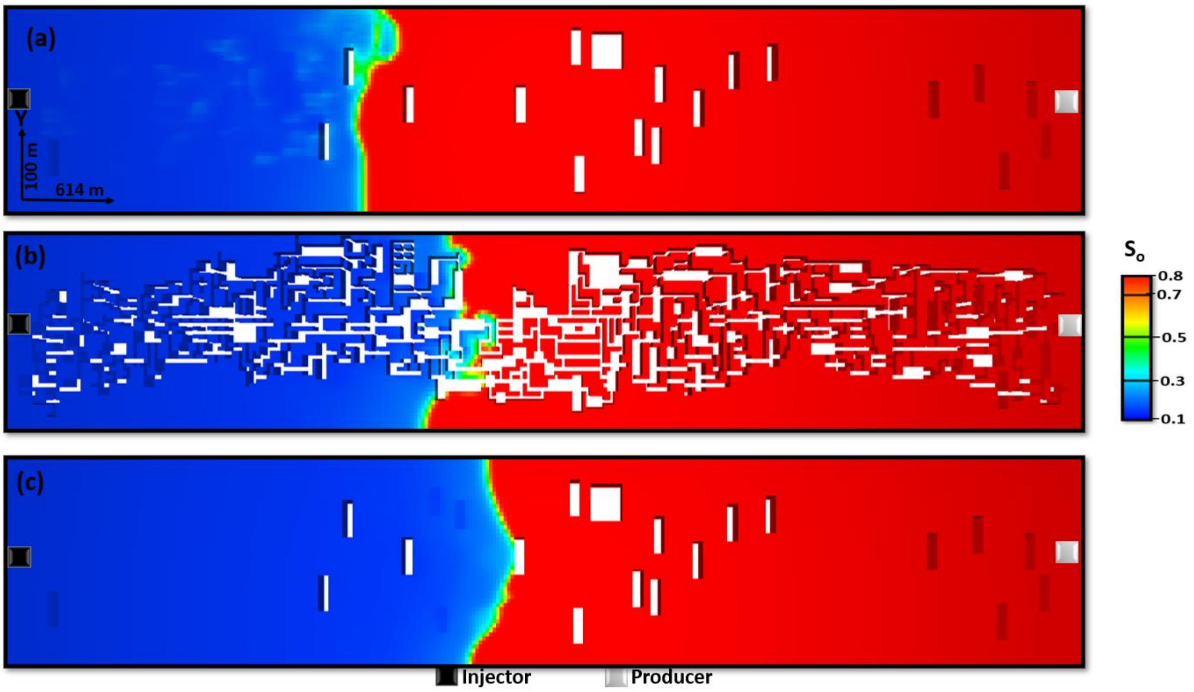

Figure 3.1-5: *A horizontal section of the complex paleokarst flow simulation model showing oil saturation at 10 mD matrix permeability of the (a) top-most layer of the cave system (b) central layer of the cave system (c) bottom-most layer of the cave system.*

Figure 3.1-6*: A horizontal section of the simple paleokarst flow simulation model showing oil saturation at 10 mD matrix permeability of the (a) top-most layer of the cave system (b) central layer of the cave system (c) bottom-most layer of the cave system.*

When the permeability of the non-cave facies is once again increased to 20 mD, massive invasion of the waterflood regardless of the facies increases improving the sweep efficiency across the reservoir. Sweep efficiency refers to the fraction of original oil in place produced by a displacing fluid during primary, secondary, or tertiary oil production. At this threshold, flooding is non selectively occurring irrespective of the geometric complexity and height in both the cave and the non-cave regions as shown in Figure 3.1-7 and Figure 3.1-8. The waterflood also observed to advance fast at the bottom of the cave than at the top of the cave passages possibly because of gravity forces dominating at lower depth. The flow pattern approaches linearity or a piston-like displacement.

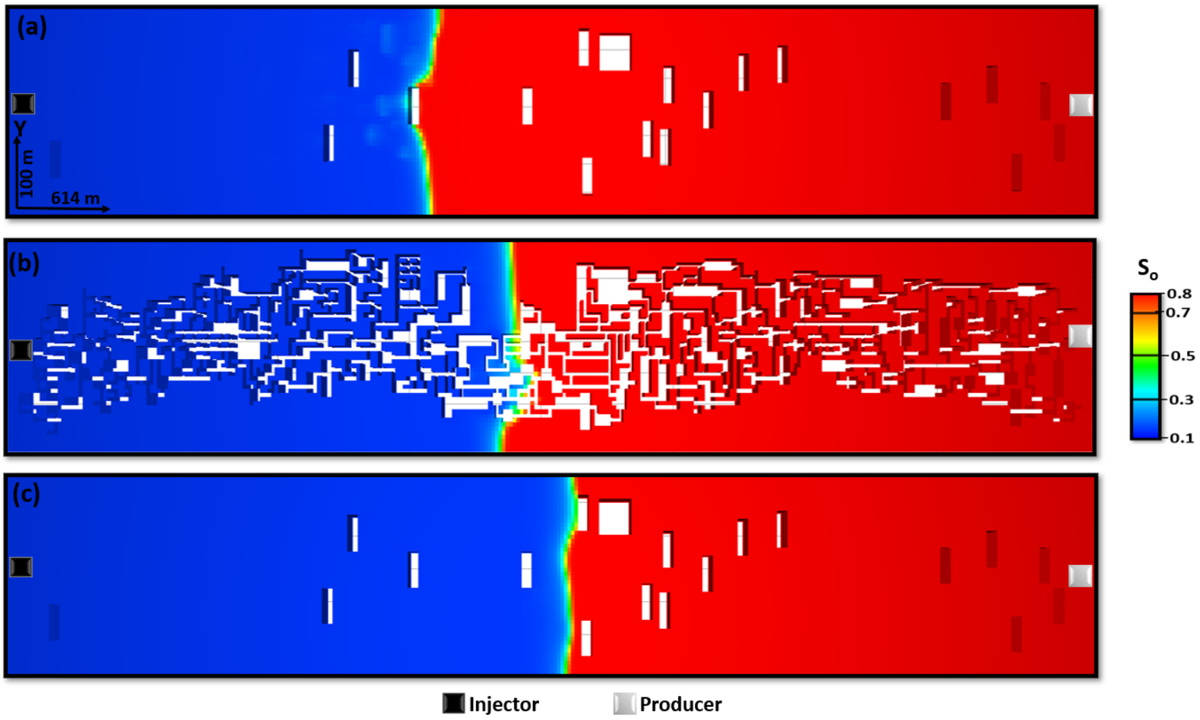

Figure 3.1-7: *A horizontal section of the complex paleokarst flow simulation model showing oil saturation at 20 mD matrix permeability of the (a) top-most layer of the cave system (b) central layer of the cave system (c) bottom-most layer of the cave system.*

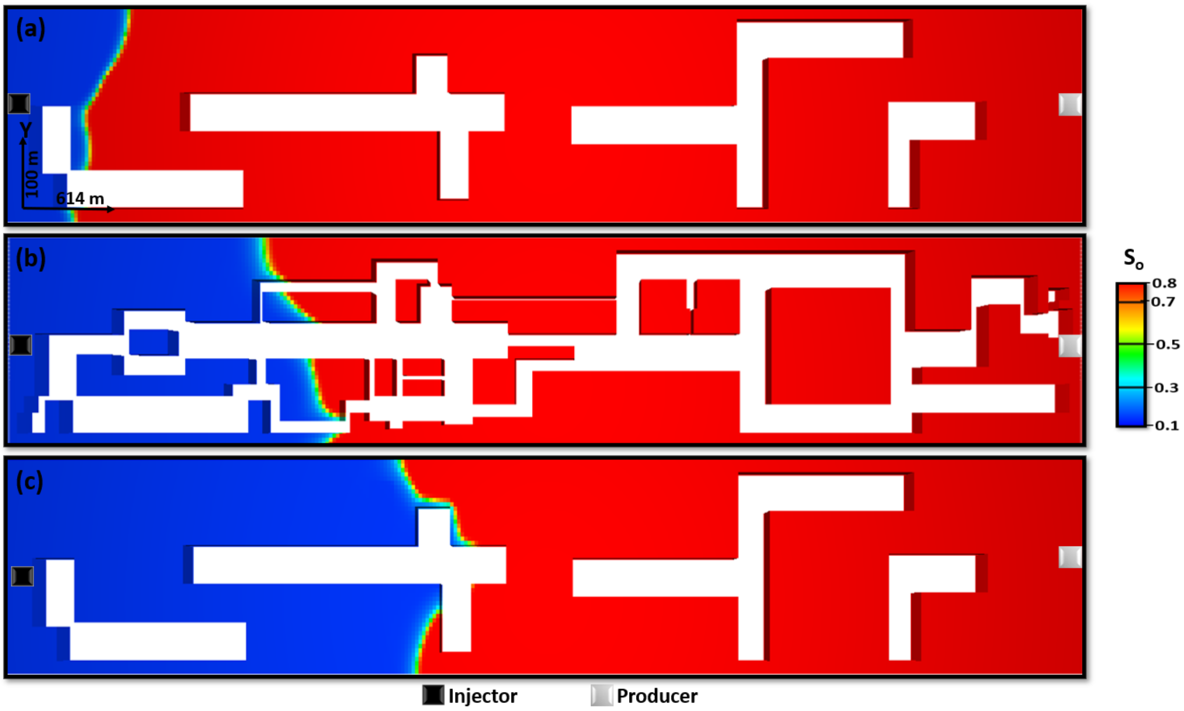

Figure 3.1-8*: A horizontal section of the simple paleokarst flow simulation model showing oil saturation at 20 mD matrix permeability of the (a) top-most layer of the cave system (b) central layer of the cave system (c) bottom-most layer of the cave system.*

Further increment of the non-cave permeability to 30 mD and 40 mD respectively leads to a trade-off between the onset of linearity and linearity or piston-like displacement. At 30 mD, a possibility of an onset of linearity of the flow pattern is observed in the complex paleokarst model (Figure 3.1-9) while the flow pattern is less linear and bulging in the simple paleokarst (Figure 3.1-10). Linearity is achieved the water-flood approaches both the cave and no-cave facies with the same magnitude and without any preference making the cave geometry to be untraceable. The distance between the waterfront sweeping into the cave and the expanding front behind reduces until both fronts nearly merge.

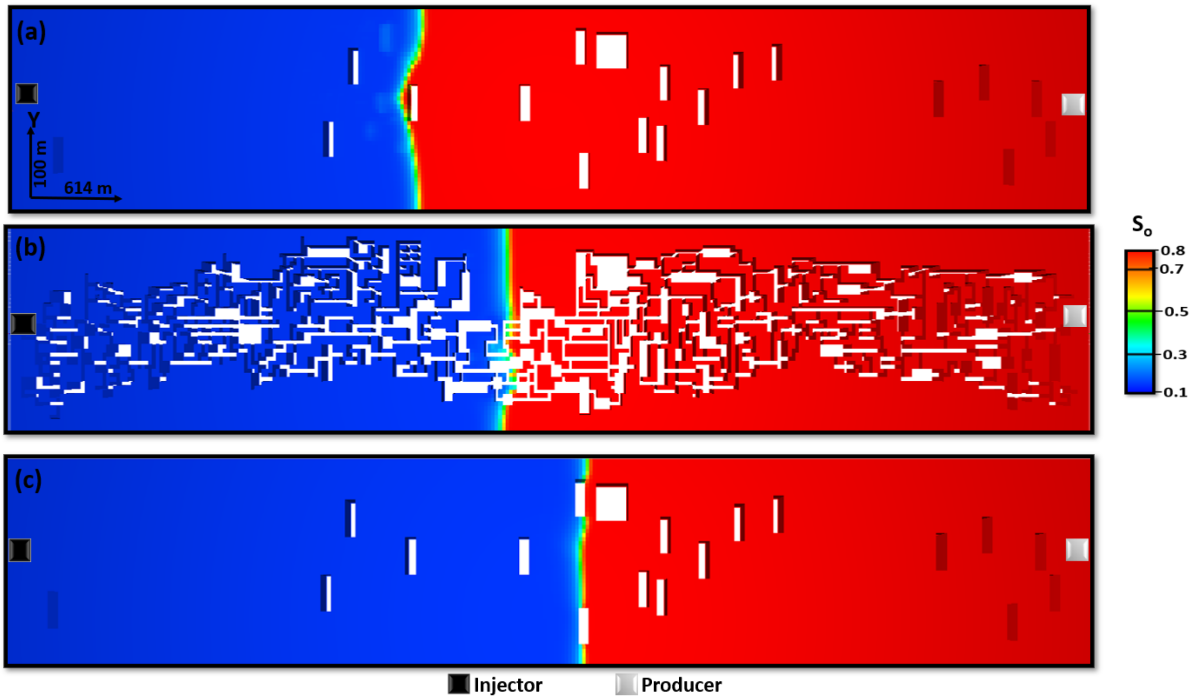

Figure 3.1-9: *A horizontal section of the complex paleokarst flow simulation model showing oil saturation at 30 mD matrix permeability of the (a) top-most layer of the cave system (b) central layer of the cave system (c) bottom-most layer of the cave system.*

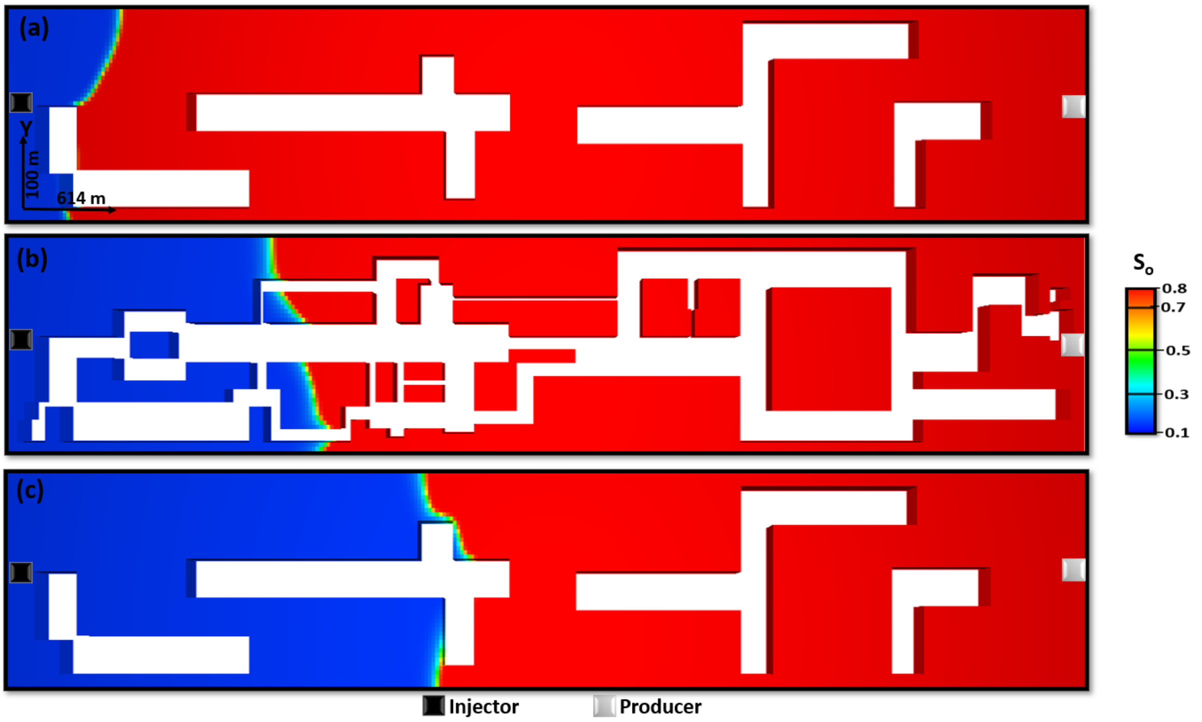

Figure 3.1-10: *A horizontal section of the simple paleokarst flow simulation model showing oil saturation at 30 mD matrix permeability of the (a) top-most layer of the cave system (b) central layer of the cave system (c) bottom-most layer of the cave system.*

At 40 mD, the displacing waterflood invades both the non-cave and the cave facies in a more uniform and homogeneous manner regardless of the cave geometry (Figure 3.1-11 and Figure 3.1-12). The shape of the approaching waterflood approximates linearity because the rock matrix is very permeable so that the pores are filled up with water and the is oil displaced. A streamline simulation of the paleokarst models at 40 mD further reveals that both the non-cave and cave facies become easiest path of preferred flow (Figure 3.1-13).

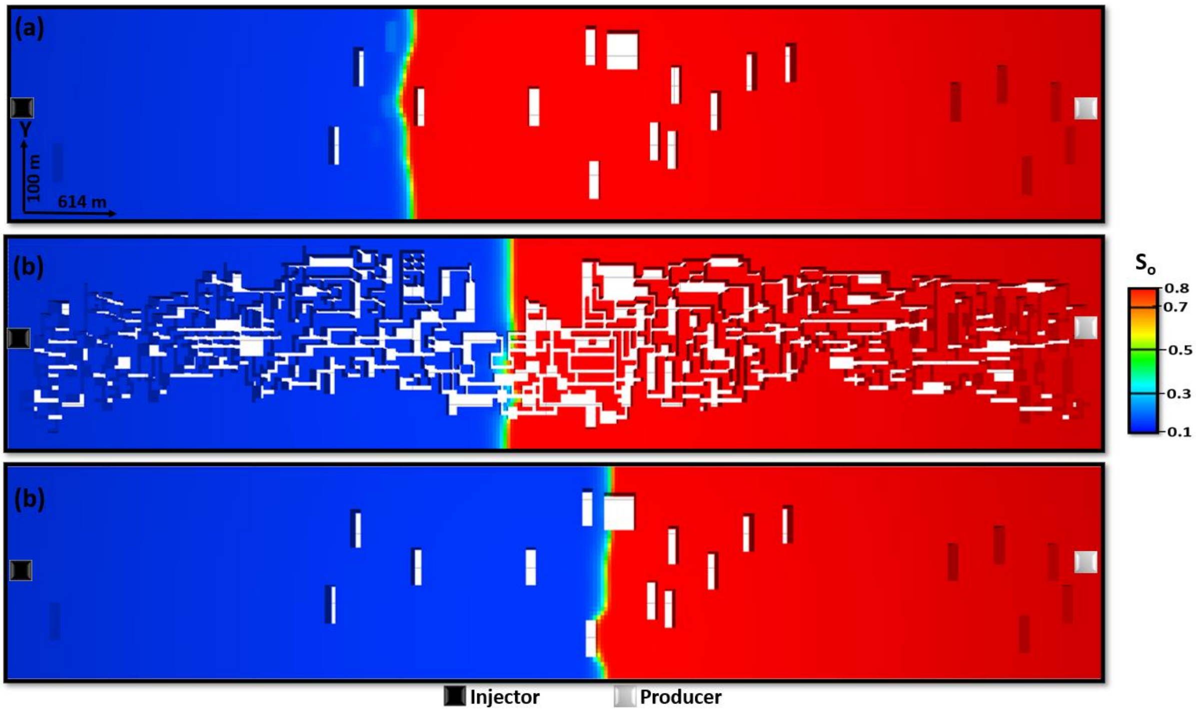

***Figure 3.1-11**: A horizontal section of the simple paleokarst flow simulation model showing oil saturation at 40 mD matrix permeability of the (a) top-most layer of the cave system (b) central layer of the cave system (c) bottom-most layer of the cave system.*

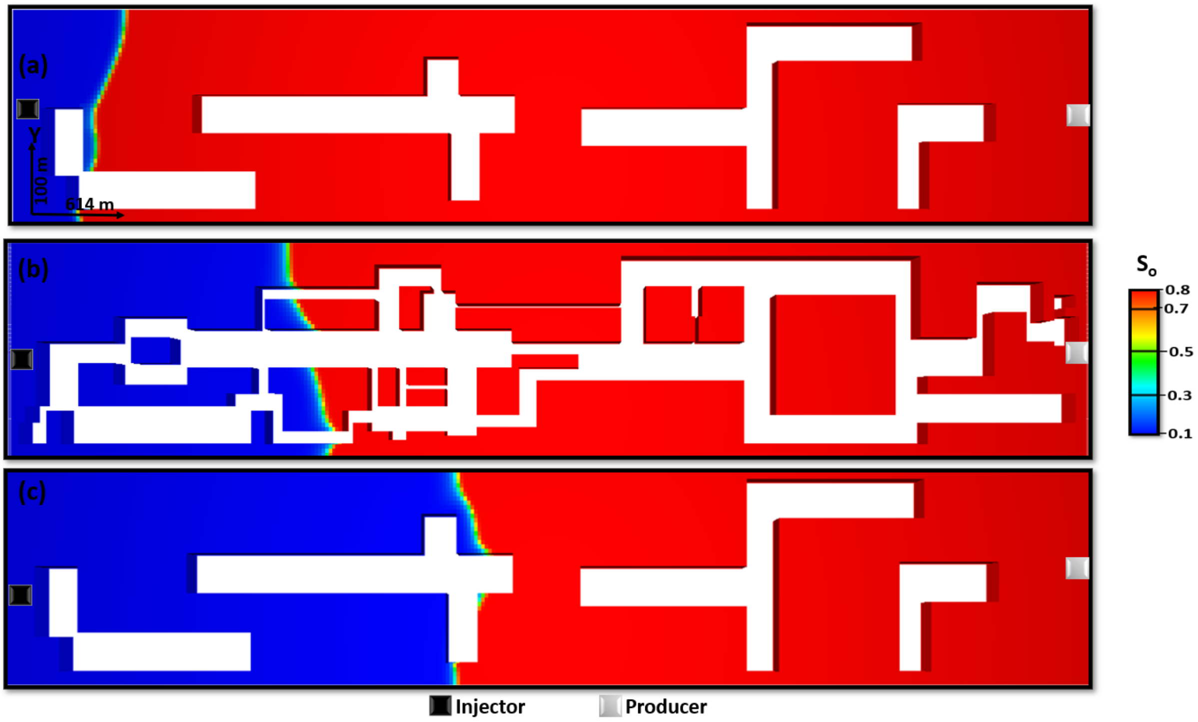

Figure 3.1-12: *A horizontal section of the simple paleokarst flow simulation model showing oil saturation at 40 mD matrix permeability of the (a) top-most layer of the cave system (b) central layer of the cave system (c) bottom-most layer of the cave system.*

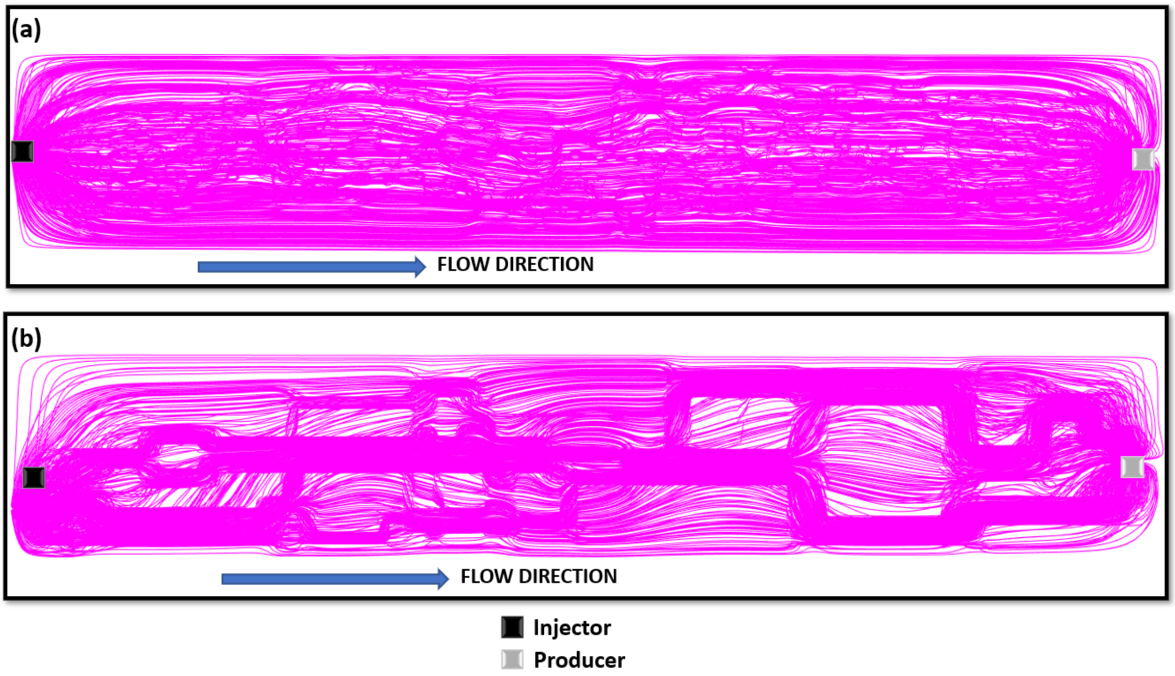

Figure 3.1-13: *Streamline simulation results at 40 mD background matrix permeability of (a) Complex simulation (b) complex paleokarst model (c) simple paleokarst model.*

There are no strict criteria but rather a qualitative approach is adopted to assign a range of permeabilities when sensitivities are observed. Sensitivities due to increasing non-cave facies permeability (non-cave facies) are as follows; from 0-5 mD, the cave geometry is visible and from 5-20 mD cave geometry is partially visible while at non-cave facies permeability greater than or equal to 20 mD, the cave geometry and the background are indistinguishable. The sensitivities in the low permeability case reveals that waterfront channels advances more into the highly permeable cave facies with very low non-cave facies invasion while the upper case shows negligible waterfront channelling and indistinguishable invasion of both cave and non-cave facies. The threshold of the non-cave (matrix) permeability can therefore be taken as a trade-off between 30-40 mD but also a value range of 10-40 mD is permeable enough to permit flow in the non-cave region as shown by the 3D plots in Figure 3.1-14 and Figure 3.1-15.

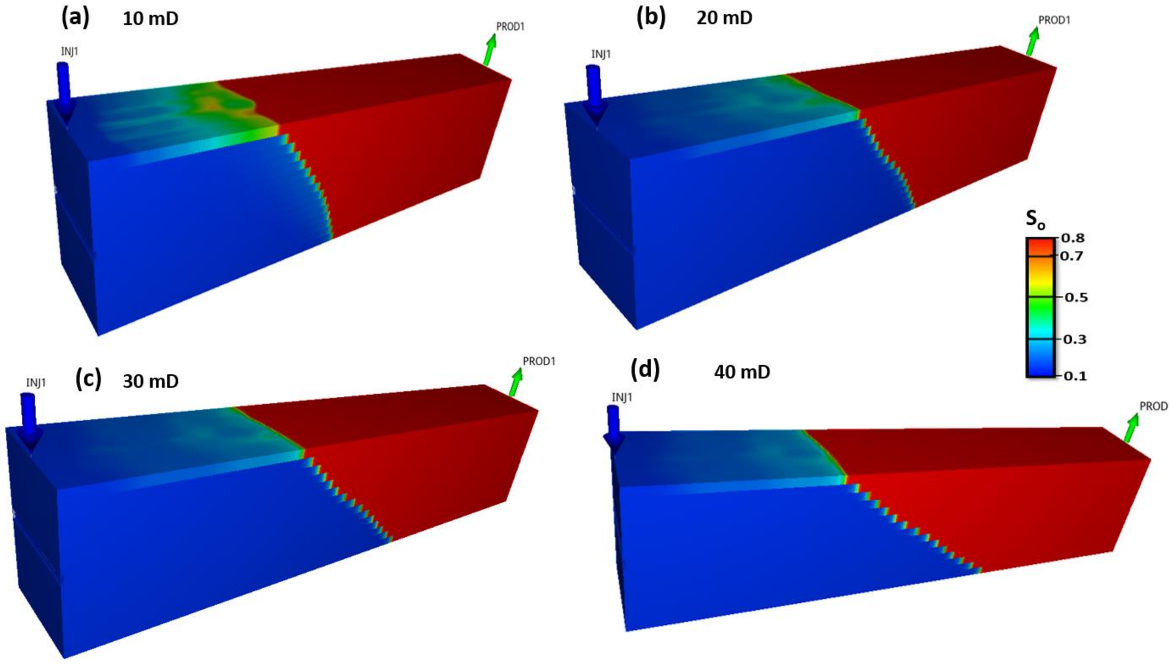

***Figure 3.1-14**: 3D sections of the complex paleokarst flow simulation model showing the waterflood front at matrix permeabilities of (a) 10 mD (b) 20 mD (c) 30 mD (d) 40 mD.*

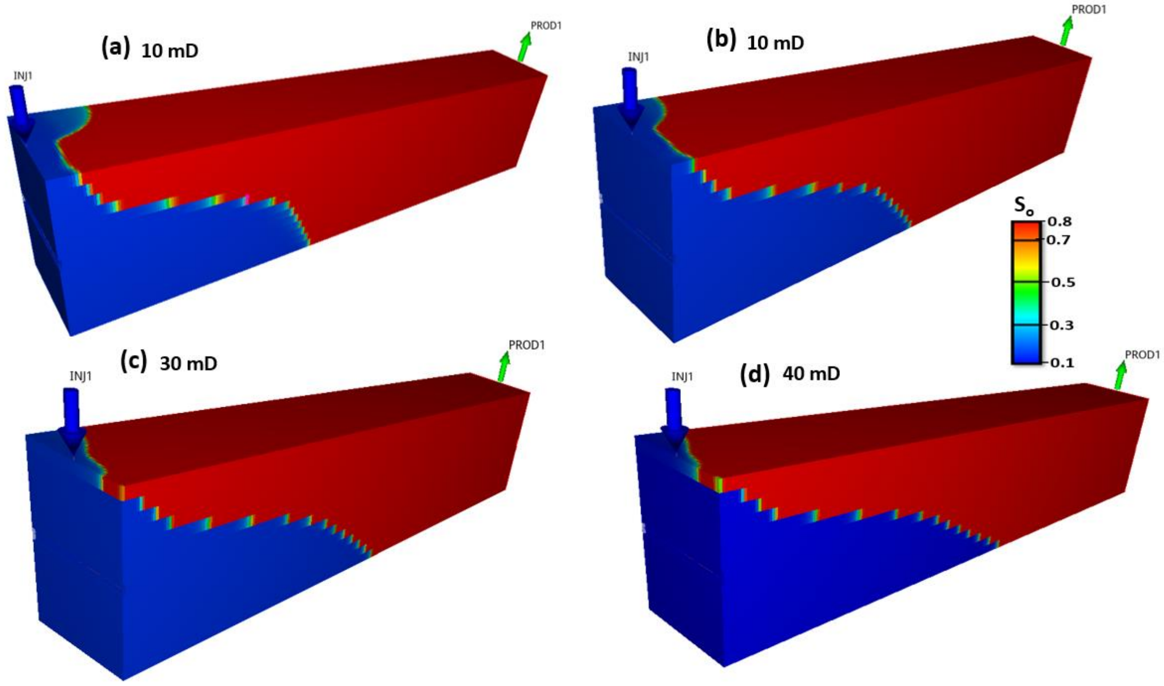

***Figure 3.1-15**: 3D sections of the simple paleokarst flow simulation model showing the waterflood front at matrix permeabilities of (a) 10 mD (b) 20 mD (c) 30 mD (d) 40 mD.*

In a relatable perspective, a recovery factor plot (Figure 3.1-16) and field oil efficiency plot (Figure 3.1-17) of both karsts and matrix regions further reveals that improvement in oil recovered in non-cave facies regions. Starting at permeabilities as low as 10 mD in the complex paleokarst model and 5 mD in the simple paleokarst model. The increase in oil recovery with increase in non-facies permeability maybe attributed to a balance of gravity, capillary and viscous forces.

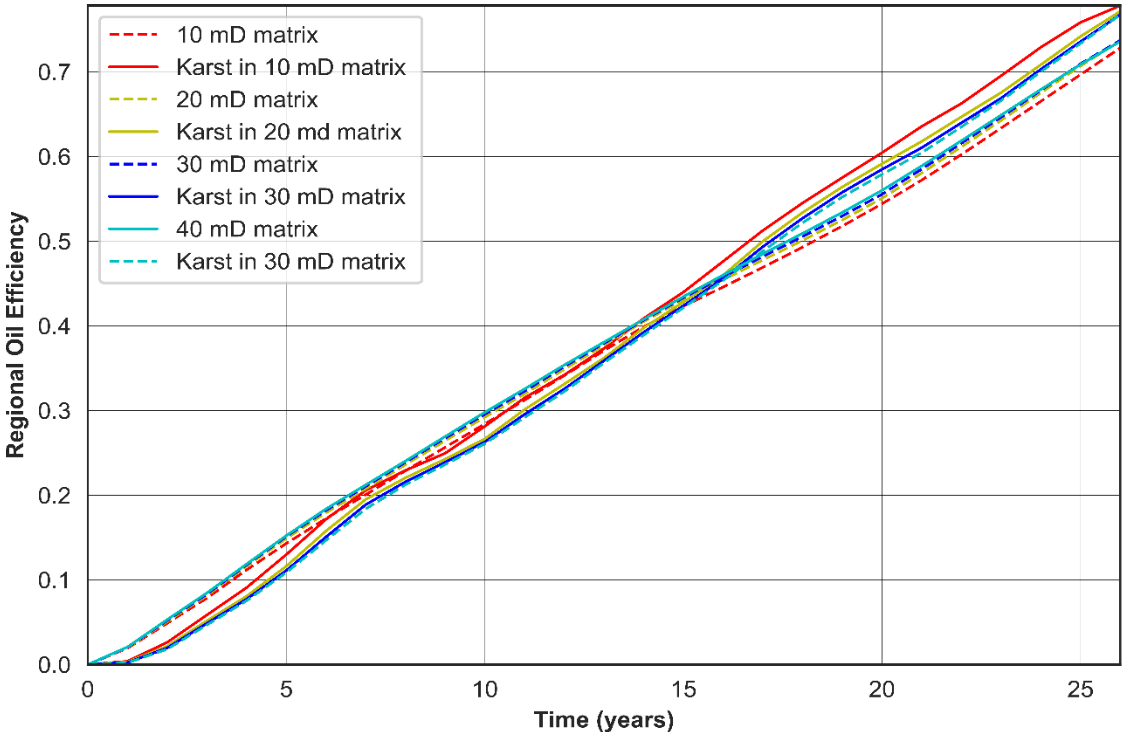

Figure 3.1-16: *A plot showing the regional oil efficiency of increasing non-cave permeability in the complex paleokarst model. The regional oil efficiency represents the fraction of original oil recovered from the cave facies (bold lines) and the non-cave facies.*

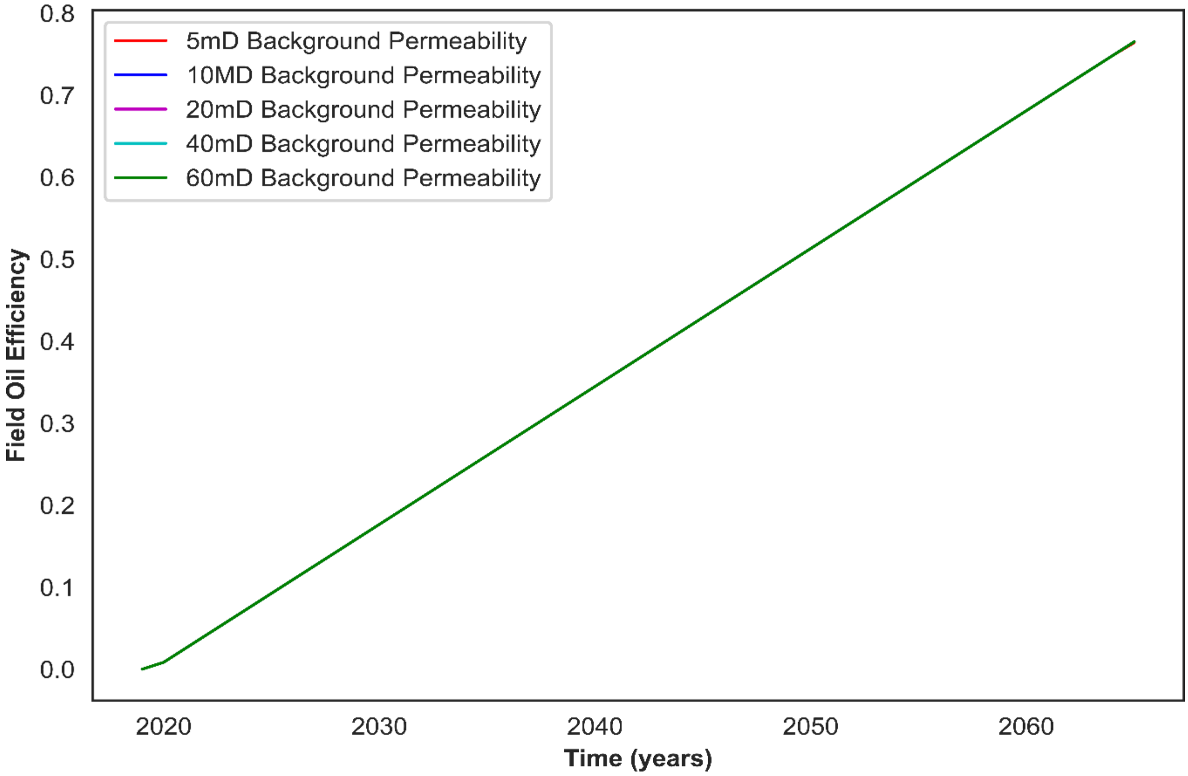

Figure 3.1-17: *A plot showing the field oil efficiency of an increasing non-cave permeability in the simple paleokarst model. The field oil efficiency is indistinguishable for all the non-cave permeability cases.*

3.1.4 Sensitivity to cave-matrix flux invasion

In this section, emphasis is put on how flux from cave facies contributes to fluid flow into the non-cave region (region) and the corresponding sensitivities. The direction of fluid flow in reservoir models is greatly influenced by pressure gradient and is regarded as linear in the flow simulator (x-direction). Further findings on whether the fluid invasion of the matrix occurs in all direction when background permeability varies are also considered. The simple generic paleokarst model was used in this study to define karst regions of interest for purposes of simplicity. In all defined karst regions with 0.1 mD (regardless of length and orientation), there is less invasion of the matrix by the displacing fluid (blue) occurs and is mainly in the direction of flow (x-direction). The flux from the cave to matrix for both short, long, horizontal, and vertical karst passages is nearly net. However, there is significant matrix invasion in the x-direction observed in the long horizontal karst proximal to the horizontal producer well (Figure 3.1-20). A cumulative oil flux value of nearly 1000 sm^3 into the non-cave region is caused by a very high-pressure gradient (in x direction). The pressure gradient is created by the difference between a declining reservoir pressure field and the high flowing bottom well pressure at the producer. In the vertical karst region (Figure 3.1-18 and Figure 3.1-19) increasing the matrix permeability results into a counter-flow behaviour as observed in the flux plots on the right. The counter flow behaviour means that there is flux from matrix to the karst region indicating the presence of a permeable matrix domain. Because the karsts are oriented vertical (y-direction), counter flow will only imply that fluid from the matrix will flowing into the cave in all directions (x, y, and z).

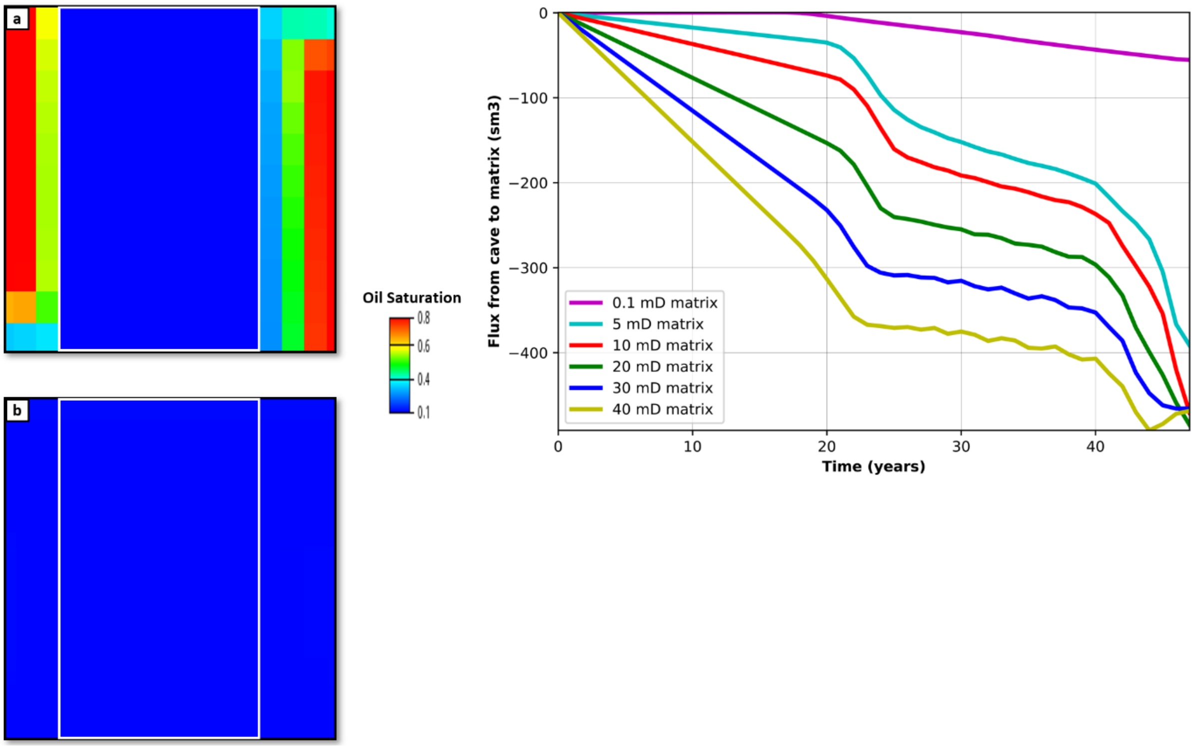

Figure 3.1-18: *Oil saturation plot (Left) of a short vertical karst region (in white rectangle)* ***(a)*** *0.1 mD matrix permeability* ***(b)*** *10 mD matrix permeability. (Right) A plot of flux from cave to matrix of increasing permeability.*

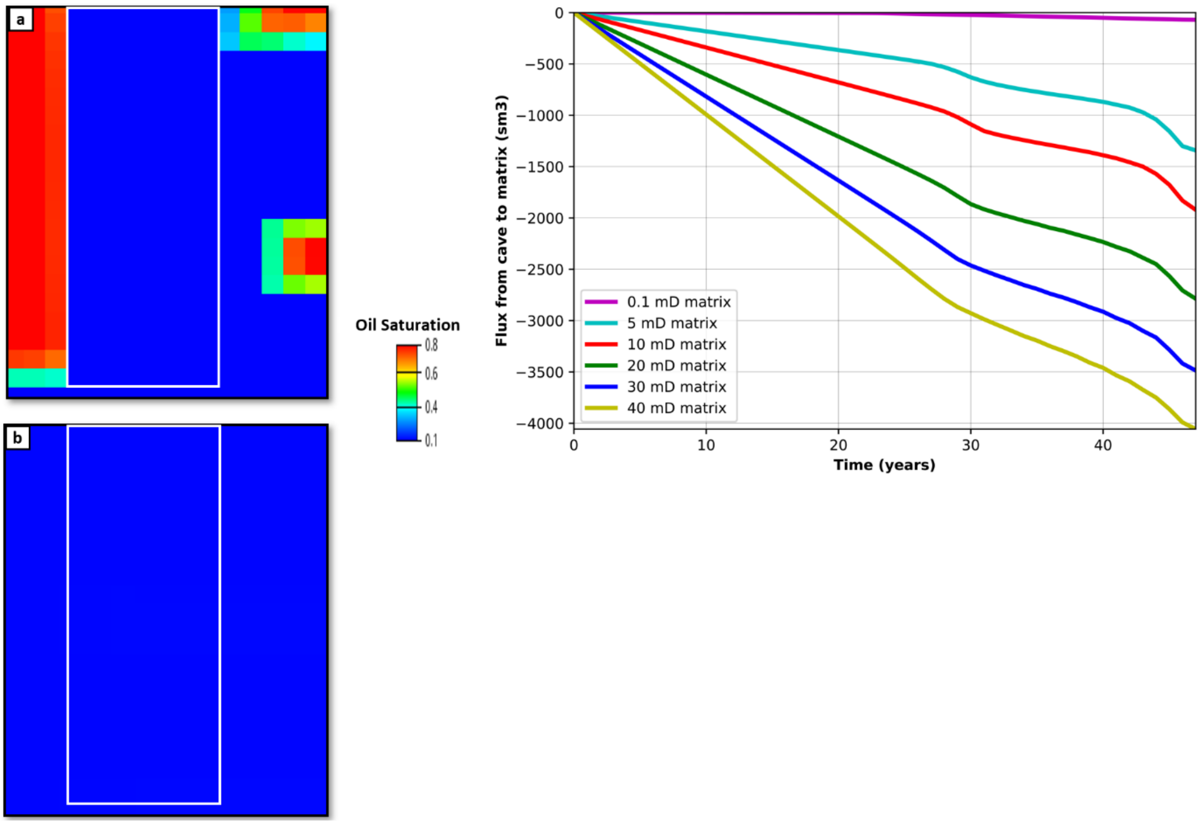

Figure 3.1-19*: A vertical cross section of saturation contrast (Left) in a long vertical cave region (in white rectangle) (a) 0.1 mD matrix permeability (b) 10 mD matrix permeability. (Right) A plot of flux from cave to matrix of increasing permeability*

As the matrix permeability is increased, the flux invasion starts to deviate from the linear direction of flow. In the horizontal karst region (Figure 3.1-20 and Figure 3.1-21) increasing the matrix permeability generally results into a cave to matrix flow behaviour. The cave-matrix flow behaviour means that there is flux from cave to the matrix region indicating the presence of a permeable matrix and more reservoir homogeneity. Because the karsts are oriented x-direction, the flux behaviour implies that fluid from the cave invades the matrix not only in the x-direction. The flux plot in Figure 3.1-21 shows that the long horizontal karst proximal to the well exhibits counter flux behaviour from permeabilities greater than 20 mD.

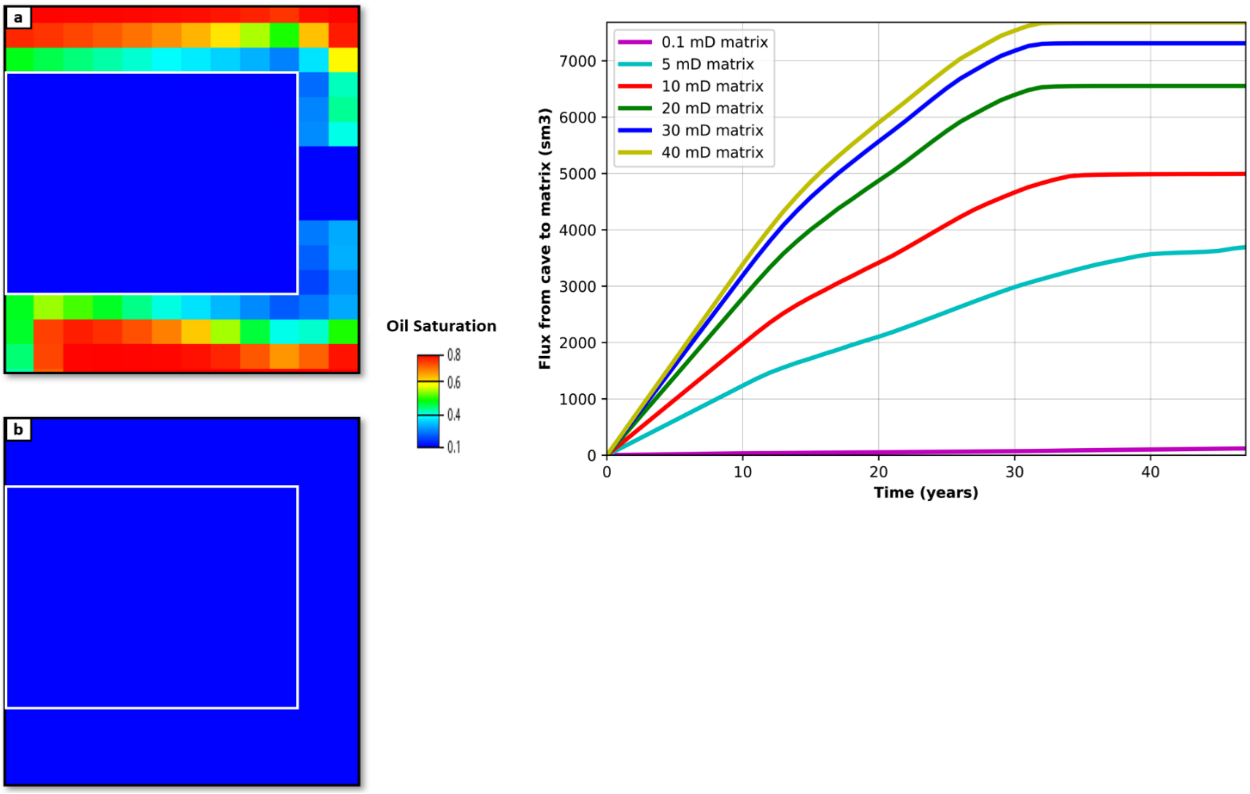

Figure 3.1-20*: A vertical cross section showing saturation contrasts (Left) in a short horizontal cave facies region (in white rectangle) (a) 0.1 mD matrix permeability (b) 10 mD matrix permeability. (Right) A plot of flux from cave with increasing non facies permeability.*

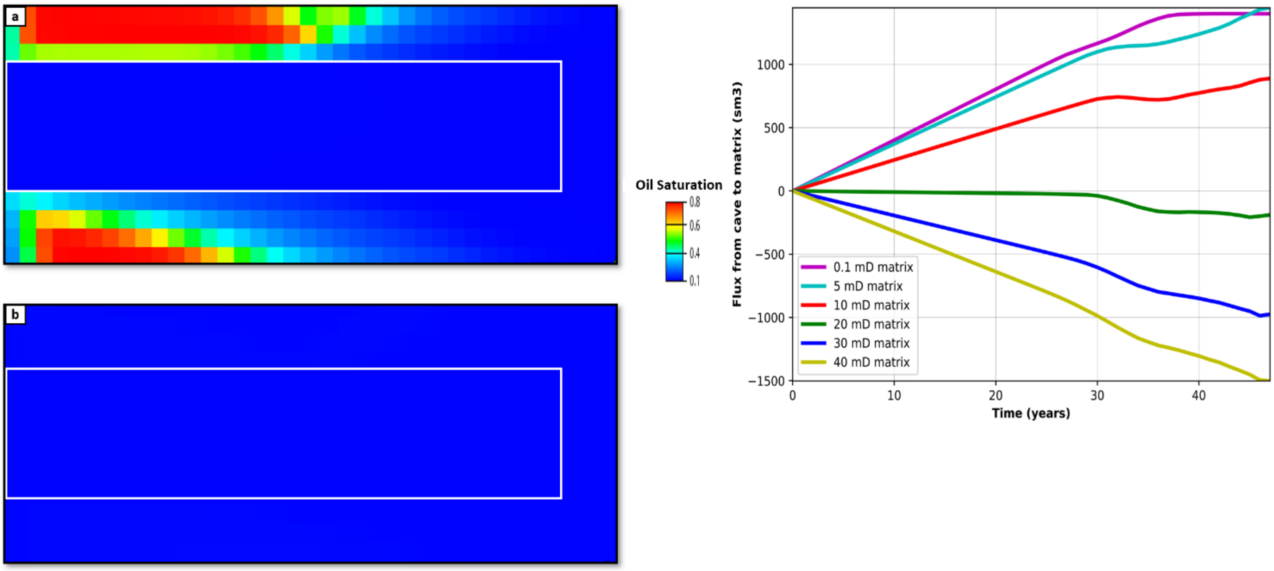

Figure 3.1-21: A vertical cross-section showing saturation contrasts (Left) of a long horizontal cave passage near a producer (in white rectangle) (a) 0.1 mD matrix permeability (b) 10 mD matrix permeability. A plot of flux from cave with increasing non-cave facies permeability (Right).

3.1.5 Sensitivity to inflow and outflow geometry

The geometry and size of the section tend contributing to different flow patterns and oil sweep in an adjacent inflow karst. The position and shape of the waterflood front may differ depending on the geometry of the karst.

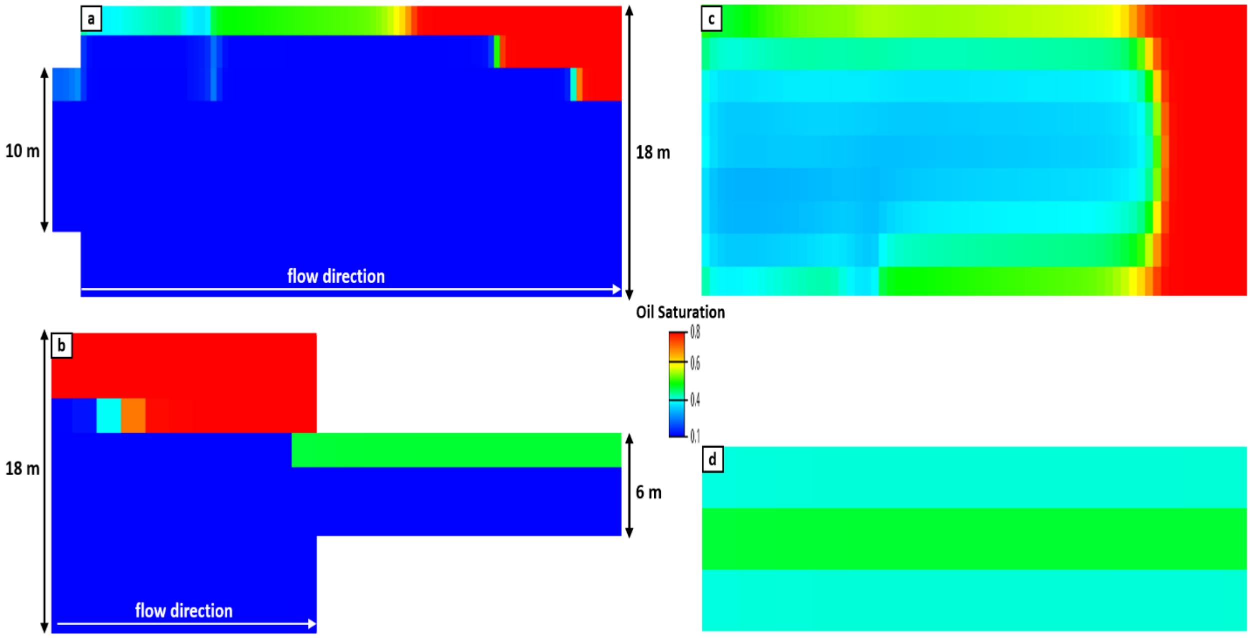

***Figure 3.1-22**: Oil saturation plot of different karst geometry (a) A vertical cross section of an 10 m inflow and 18 m out flow karst cavities and (c) the corresponding top view of outflow karst conduit (b) A vertical cross section of a 18 m inflow and a 18 m out flow karst cavities and (d) the corresponding top view of outflow karst conduit.*

It is evident that water flux from bigger karsts contributes to better oil sweep in smaller conduits to which they connected, [Figure 3.1-22 (a & c)]. However, in instances where small karsts are connected to bigger conduits, poor oil sweep is observed in bigger conduits and oil is trapped at the top [Figure 3.1-22(b & d)]. Most of the trapped oil is at heights greater than the diameter of the small conduits. Karst conduits having the same geometry and size tend to have excellent oil sweep and flow continuity in the upper most layers.

3.1.6 Sensitivity to varying infill composition

Caves and fractures infilled by sediments and other clastic sediments are characteristic of a buried and collapsed paleokarst formed in the vadose zone. Infill recovery from an 8 m vertical karst core (Figure 3.1-23) in Tarim basin suggests a fining upward succession consisting of conglomerates, well sorted sandstones, muddy sandstone and calcite (Zhao et al., 2014).

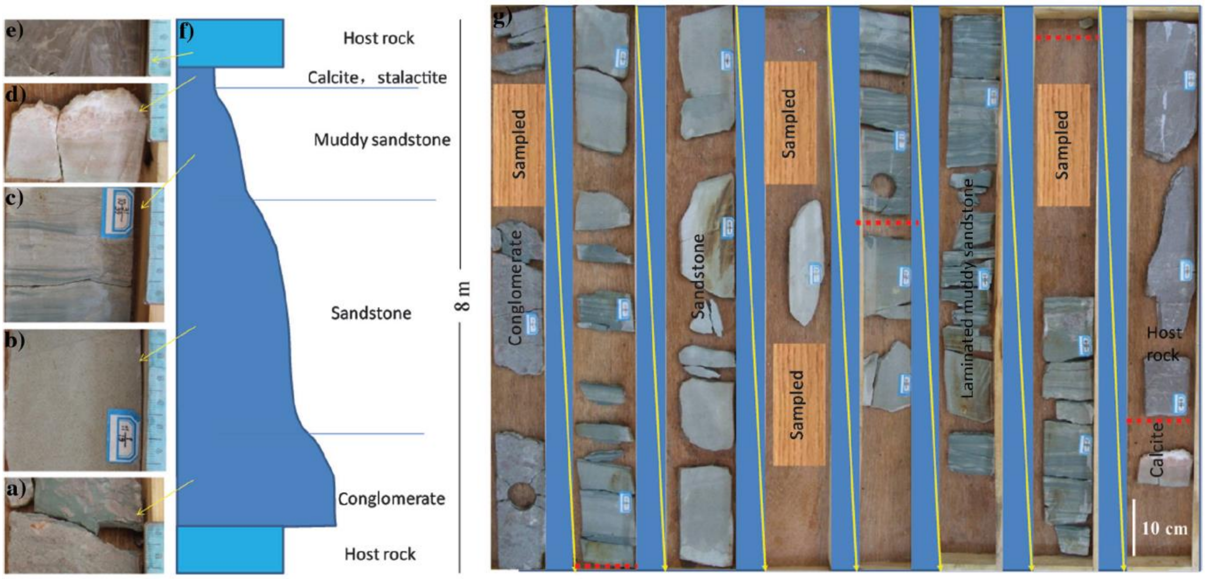

Figure 3.1-23*: core section of karst infills from Tarim basin (a) conglomerate (b) sandstone (c) laminated mudstone (d) calcite (e) host rock (f) log section (g) overview of all the core section.*

Further evidence of massive sediments accumulation in caves has been observed in modern caves. B. Lønøy et al. (2019) using electric resistivity tomography methods discovered several cave passages filled by up to 75% fluvial sediments while in large chambers the sediments were interbedded with collapse breccia. On burial, these cave infill and could affect the reservoir quality and fluid flow behaviour of paleokarst reservoirs. Therefore, to study the effect of infills on the production behaviour in paleokarst reservoir, I adopted the simple generic paleokarst model because of it is less mundane and easier to assign facies and petrophysical properties. Varying reservoir properties (porosity and permeability) are assigned to the karst domain to correspond to a sequence of depositional and collapse phases, for example sand and collapse breccia. The karst infill succession is such that the sand is at the bottom while collapse breccia material fills up the rest of the cave. The background host rock matrix maintains the same petrophysical properties. It is evident that homogenization of the flow properties (porosity and permeability) does not fully capture small scale details and tends to overestimate the cumulative oil production (Figure 3.1-24). Therefore, to increase accuracy and proper estimation, the karst infill flow properties are implicitly assigned.

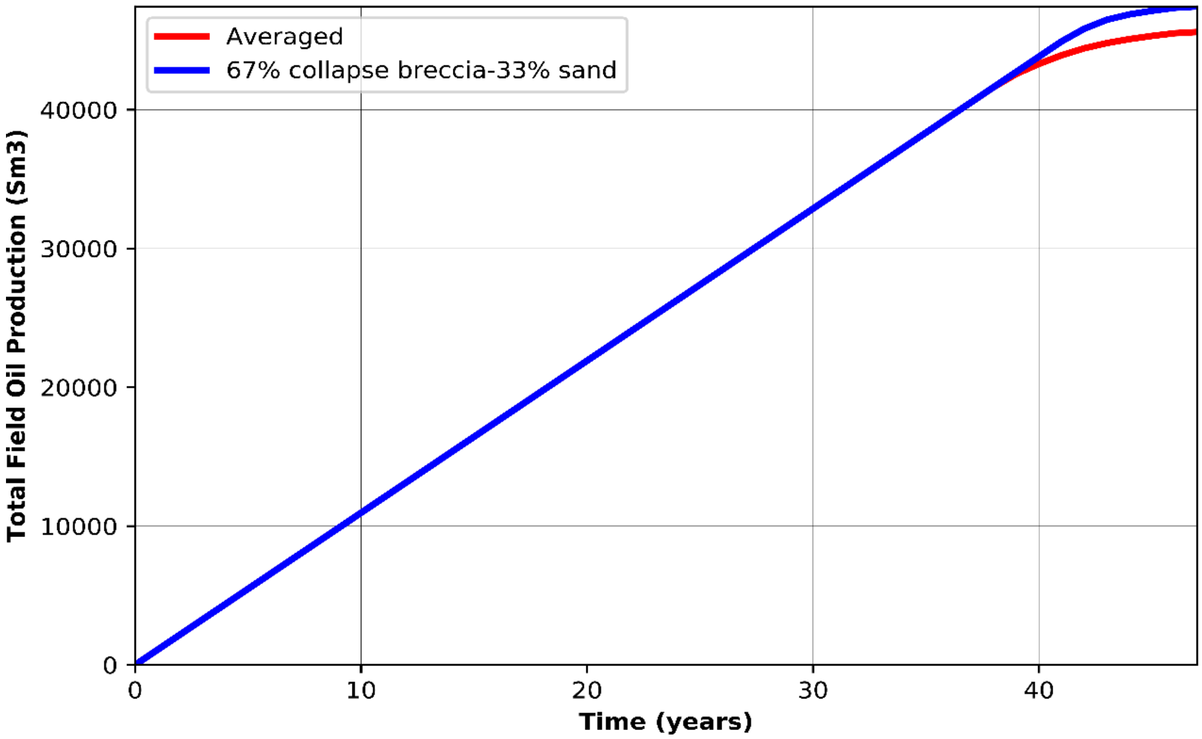

Figure 3.1-24: *Comparison of production from averaged and relative composition of cave infills.*

The sand at the bottom of the cave is assigned a 20% porosity, 350 mD horizontal permeability and 35 mD vertical permeability. The collapse breccia has 25% porosity and 2200 mD permeability. The steps taken in construction of the simplified infill karst model are summarised in Figure 3.1-25.

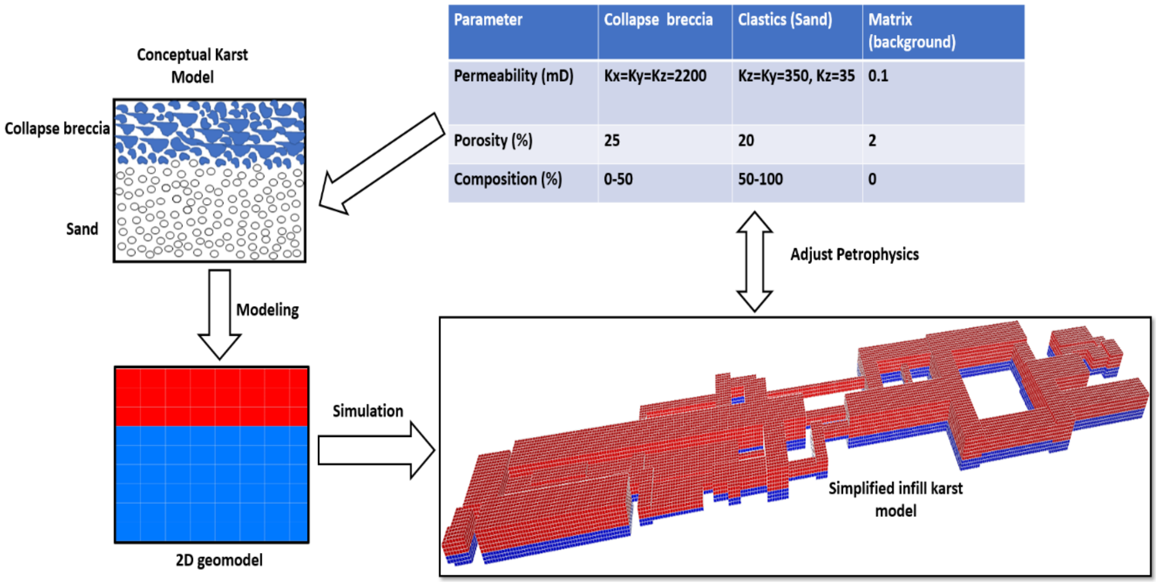

Parameter	Collapse breccia	Clastics (Sand)	Matrix (background)
Permeability (mD)	Kx=Ky=Kz=2200	Kz=Ky=350, Kz=35	0.1
Porosity (%)	25	20	2
Composition (%)	0-50	50-100	0

Figure 3.1-25: *Workflow for cave infill geomodelling.*

Flow simulation of different paleokarst infill scenarios are analysed to predict flow behaviour of injected water in infills of varying petrophysical properties. The simulated paleokarst model consists of 50% sand and 50% collapse breccia. Sand occupies the bottom half of the cave passages while the collapse breccia occupies the rest of the cave passages. Figure 3.1-26(a-d) shows a 2-D vertical section of changes in reservoir saturation and the fluid flow pattern during production by water injection in steps of 5, 10 15 and 20 years. From all the injection phases its observed that injected water prefers to flow at a faster and displace the bottom layers before proceeding to the layers. This behaviour could be associated with gravity segregation happening in the large cave passages where gravity forces are dominant over viscous and capillary forces causing the denser water to sink to the bottom at the onset of water injection. However, uniform flow pattern is observed in regions outside the cave passages where the matrix has homogeneous petrophysical properties.

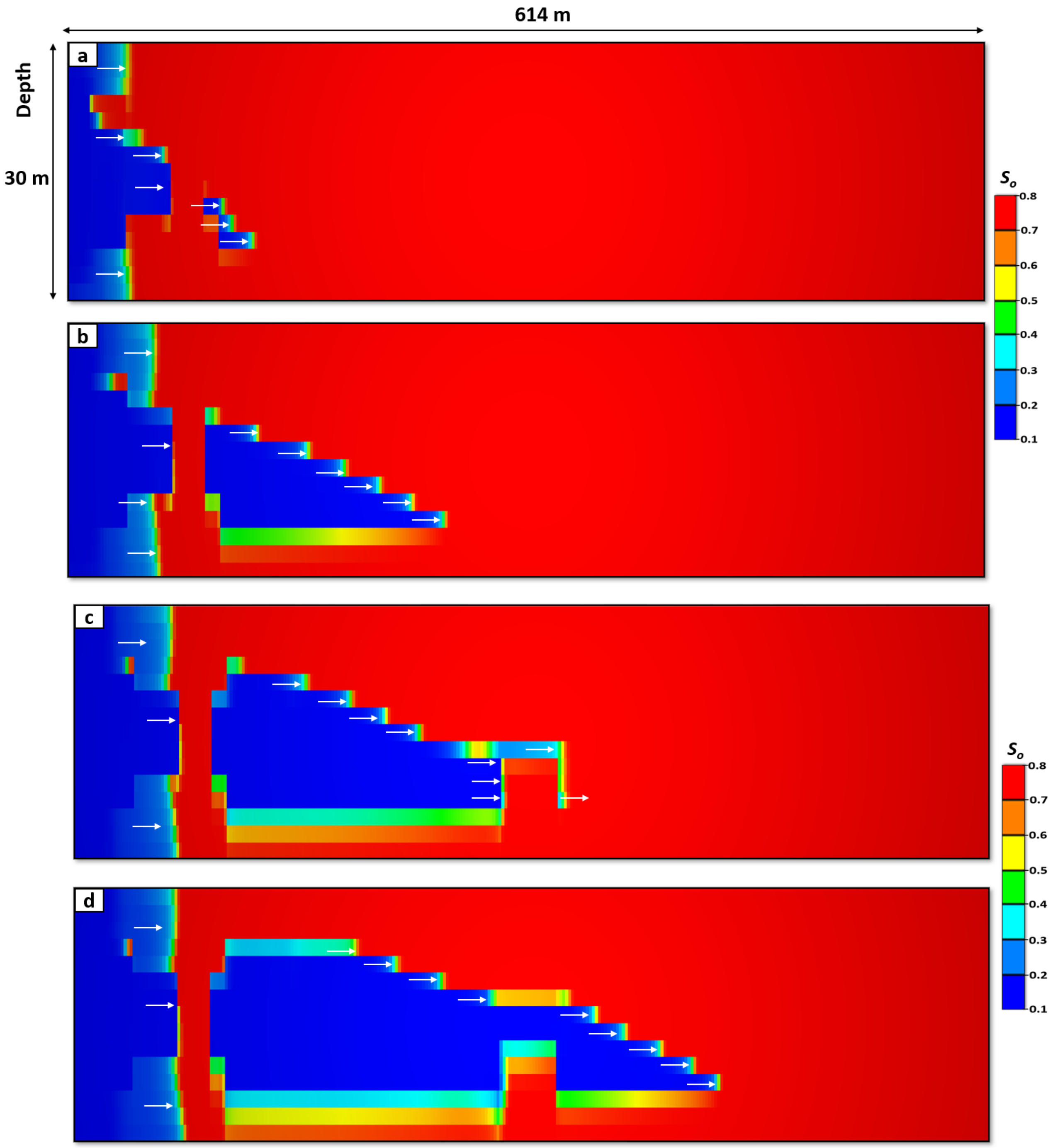

***Figure 3.1-26**: Saturation changes related to flow in different cave sections during water injection phases (a) 5 years of injection (b) 10 years of injection (c) 15 years of injection (d) 20 years of injection.*

To relate the relationship of the flow behaviour observed in Figure 3.1-26 (a-d) to production in paleokarst reservoir, five scenarios of varying karst infill composition in percentage are simulated. The process is carried out in steps, starting with equal infill compositions, and then increasing or decreasing the percentage of each in all karst in the model, i.e., until the karsts are entirely filled with sand. The corresponding total oil produced by karsts in the different realizations are compared (Figure 3.1-27).

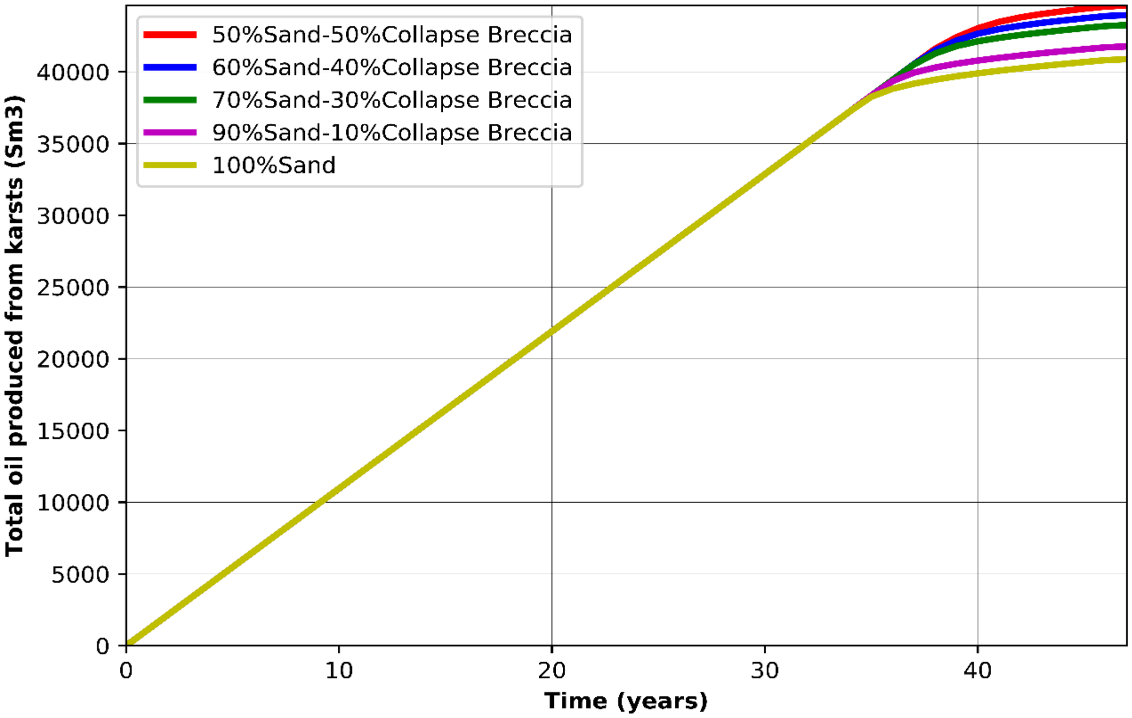

Figure 3.1-27: A plot of cumulative oil produced from karsts with varying karst infill compositions.

It is clearly evident from the production plot in Figure 3.1-27 that best case scenario occurs when the cave is half-filled with sand while the worst-case scenario is observed when the cave is filled with only sand. The approaching oil displacing waterflood in both scenarios exhibits a tendency to sink at the bottom and sweeping the sandstone layers first. This behaviour maybe because of gravity forces dominating over capillary and viscous forces thus upswept oil at the topmost layers of the collapse breccia. The low recovery observed in the caves filled with only sand can attributed to the relative moderate horizontal permeability and the very low vertical permeability as compared to the very permeable collapse breccia. The results and observation from varying sediment infill maybe affected by simulation software artefacts and thus need to be validated with a different flow simulation technique that employ numerical flow equations other than the Darcy’s equation. However, the validation process is beyond the scope of this study.

3.1.7 Sensitivity to well patterns

In this study, sensitivities arising from simulation results of different well patterns are addressed. Well pattern design is a field development strategy aimed at improving recovery in heterogeneous or low permeability hydrocarbon reservoirs. Horizontal and 5-spot well designs are interchangeably simulated such that wells are either placed in the cave or outside the cave.

Firstly, results from two horizontal wells are compared followed by a 5-spot well pattern and its inverted version. A 5-spot well pattern is a model with an injector at each corner of the reservoir and a producer in the centre while an inverted 5-spot well pattern has a producer at each corner and an injector occupies the centre. The complex generic karst model having a volume of 614x100x30 m^3 is used. A homogeneous porosity and permeability are assigned in both the rock matrix and the karst domain. To further understand combined sensitivities resulting from matrix permeability, well placements, and well patterns, results from models having matrix with a low permeability (0.1 mD) and a threshold permeability (40 mD) are compared. From this model, different realizations of well pattern designs are simulated

Horizontal wells

The Complex Geometric Karst Embedded Model-CGKEM with a water injector and a producer outside the karst is adopted for this study. The wells are horizontal in nature and are symmetrically located in the central layer of the reservoir. The injector is positioned to the left while the producer is to the right of the reservoir placed 610 metres apart and penetrating only the rock matrix. The drainage region for the injected water. The reservoir is produced for 20 years and the flow pattern after 5, 10, and 20 years of water injection analysed (Figure 3.1-28). The water injection rate is maintained by a constant bottom hole pressure. For the first 5 years, the injected water distribution flows mainly into the very permeable cave geometry at a faster rate than the distribution in the rock matrix. The water invasion into the matrix is slow because of the very low permeability and lack of storage space (due to low porosity). At 10 years, the entire cave is flooded by the injected water but with less water distribution than at 5 years. This is attributed to the reduction in reservoir pressure as the waterfront advances proximal to the producer. To the extreme right of the reservoir, the water flood starts to cone towards the producer well due to a very sudden high bottom hole flowing pressure. The injected waterflood distribution in the karst greatly increases. This is shown by the prominent shade of blue in Figure 3.1-28 (bottom). Important to note is that the injected waterfront in the rock matrix advances further both around the cave and in the rock matrix between the cave passages.

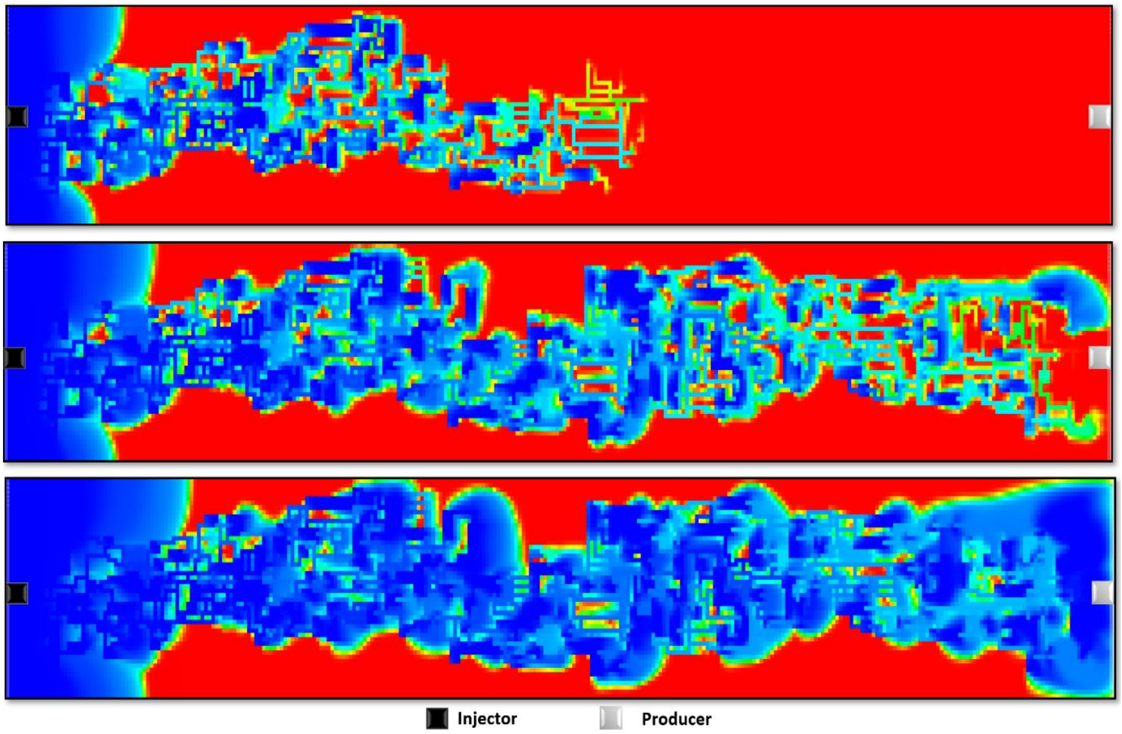

***Figure 3.1-28**: Flow pattern in complex generic model with the horizontal wells outside the cave (top) oil saturation after 5 years of production (middle) oil saturation after 10 years of production (bottom) oil saturation after 20 years of production.*

In the second case (Figure 3:1-29), the well pattern design adopted is identical to that used in the first case. The only difference is that the wells are positioned to only penetrate the cave/karst. The horizontal well sections penetrating the rock matrix are not perforated. This is done to ensure that water is injected into the cave. The produced oil can be a contribution from both the cave and the non-cave facies. The non-cave region is a porous media with low permeability. It is observed that the flow pattern is mainly in the more permeable cave facies at all years of production with less or negligible flow into the non-cave facies. This is mainly the rock units above and below the cave. The matrix rock enclosed by cave passages are easily flooded by the approaching as early at 5 years of production.

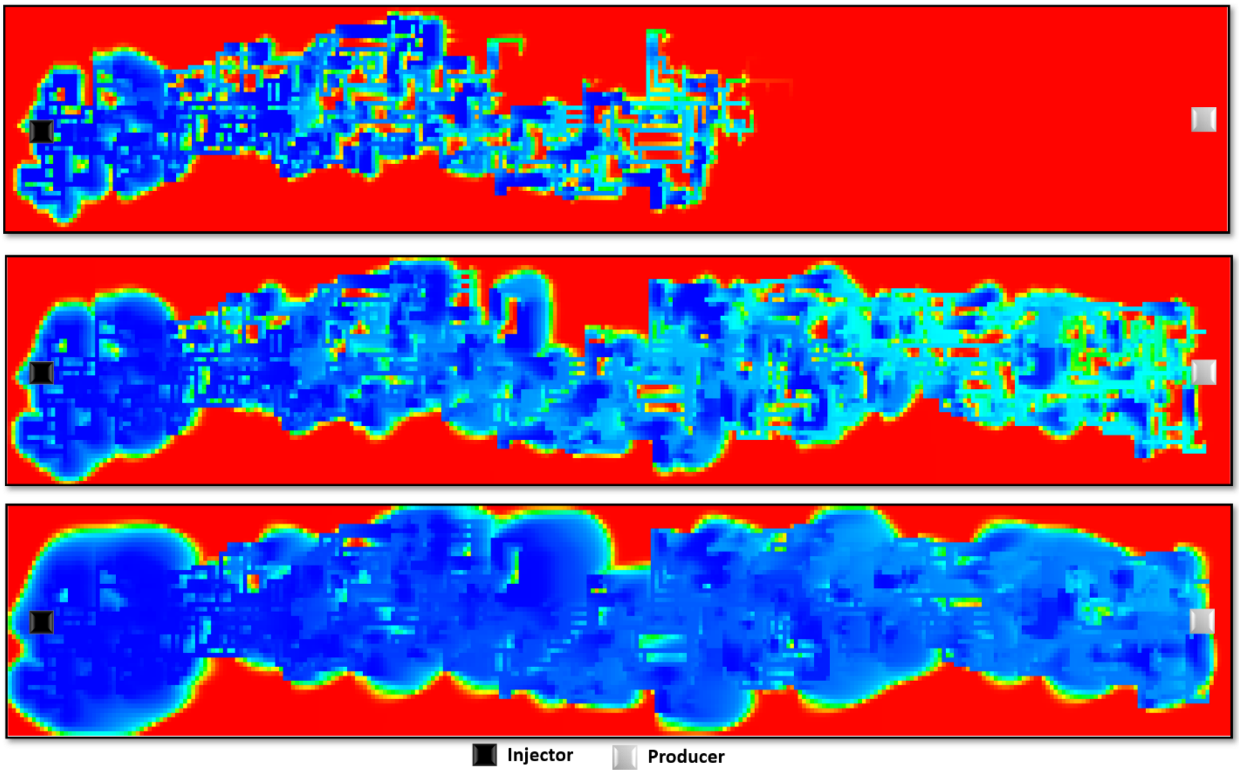

Figure 3.1-29: *Flow pattern in complex generic model with the horizontal wells inside the cave (top) oil saturation after 5 years of production (middle) oil saturation after 10 years of production (bottom) oil saturation after 14.5 years of production. Production stops at 14.5 years because the reservoir pressure falls below the bubble point.*

Better oil recovery factors are observed in models where the wells are in the cave than when the wells penetrate only the rock matrix. Placing the wells in the karst creates a preferred flow path in the direction of flow at a faster rate. Because the reservoir pressure decays with distance, the flow rate drops significantly after water breakthrough as observed causing production to stop after 14.5 years of production (dashed lines in Figure 3.1-30). As the bottom hole pressure drops to zero, the reservoir pressure drops to a minimum disregarding lift requirement. In the realization where the wells are placed outside the cave, the initial flow rate is low because of a flow barrier imposed by a less permeable rock matrix proximal to the more permeable cave 8 metres away. After overcoming this barrier, the injected water sweeps through the cave at a steady rate higher than the areal sweep in the matrix. The reservoir is produced throughout its life with a steady reservoir pressure, better productivity index and economical oil recovery rates.

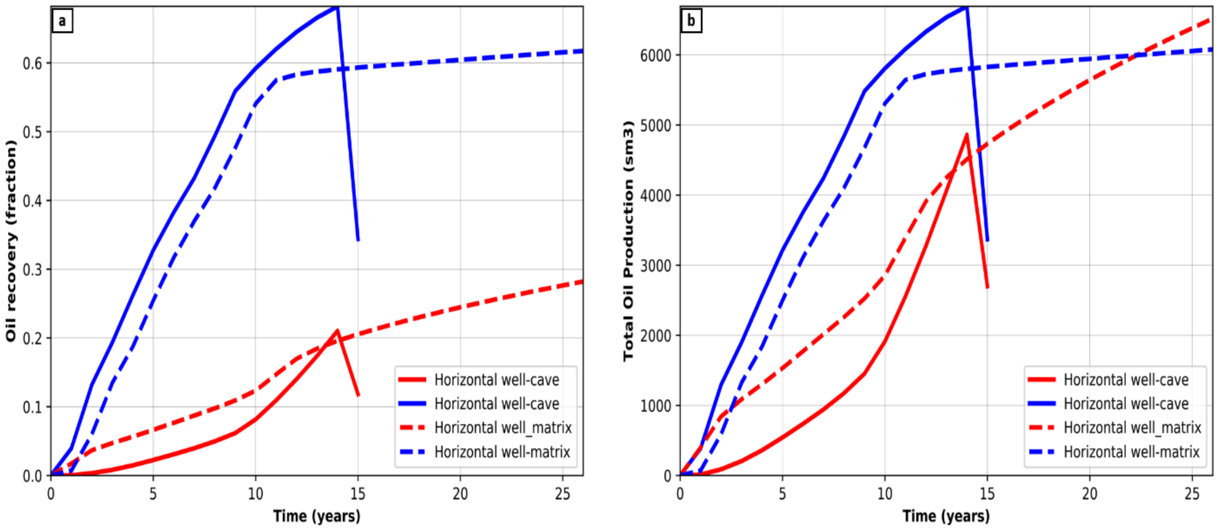

***Figure 3:1-30**: Production plots of the simple generic model using horizontal well. (a) Oil recovery with wells in karsts only (bold lines) and matrix only (dashed lines) (b) cumulative oil produced from karsts only (bold lines) and matrix only (dashed lines).*

5-spot and inverted 5-spot well pattern

The first case, three well placement scenarios identical to the CGKEM were simulated. The difference is that the 5 vertical wells were used in each model instead of vertical wells. The model consists of 4 injectors in the corners of the model a producer in the centre. The water flood injectors and the producers in all the cases have the same injection and production characteristics. The second scenario is the inverted 5-spot well pattern. It is the opposite of the first case. The producers are placed in each corner of the model and a water injector in the centre. Oil saturation plots and recovery factor plots for incidences where the wells are outside the karsts, in both karsts and matrix and outside the karsts are compared (Figure 3.1-31, Figure 3.1-32, Figure 3.1-33, and Figure 3.1-34).

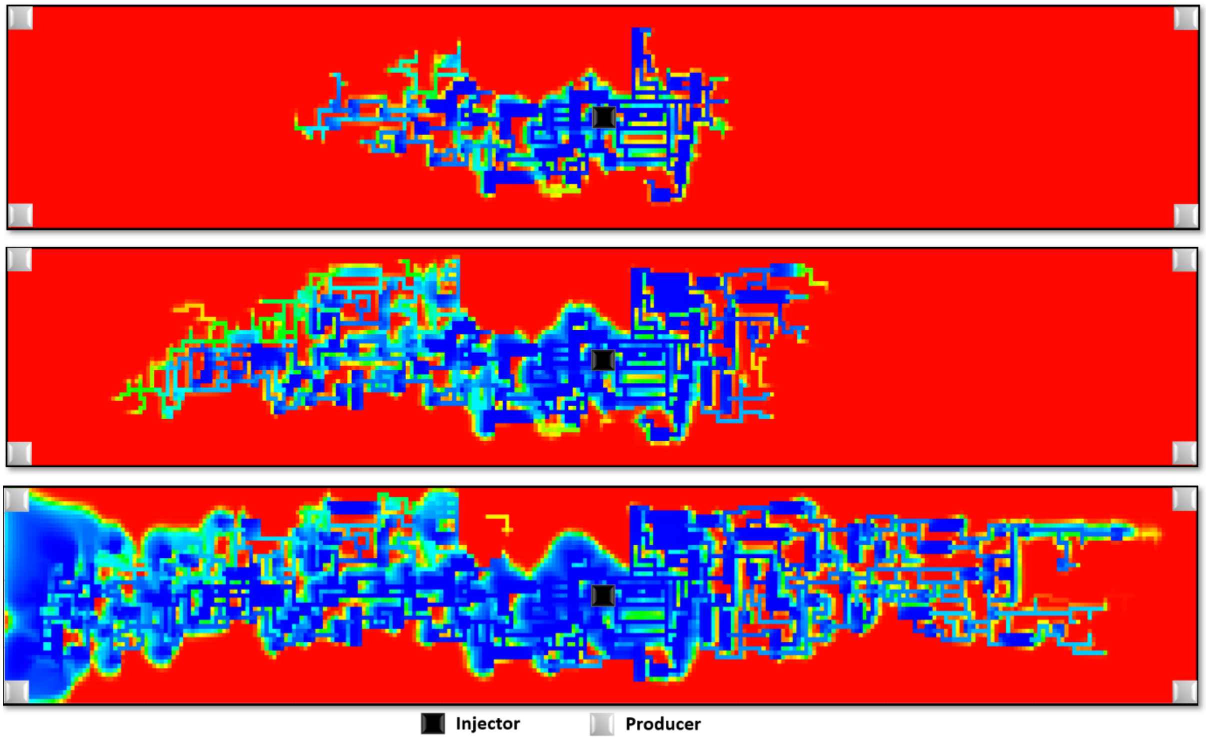

***Figure 3.1-31**: Flow pattern in an inverted 5-spot box model showing wells located outside the cave (top) oil saturation after 5 years of production (middle) oil saturation after 10 years of production (bottom) oil saturation after 20 years of production.*

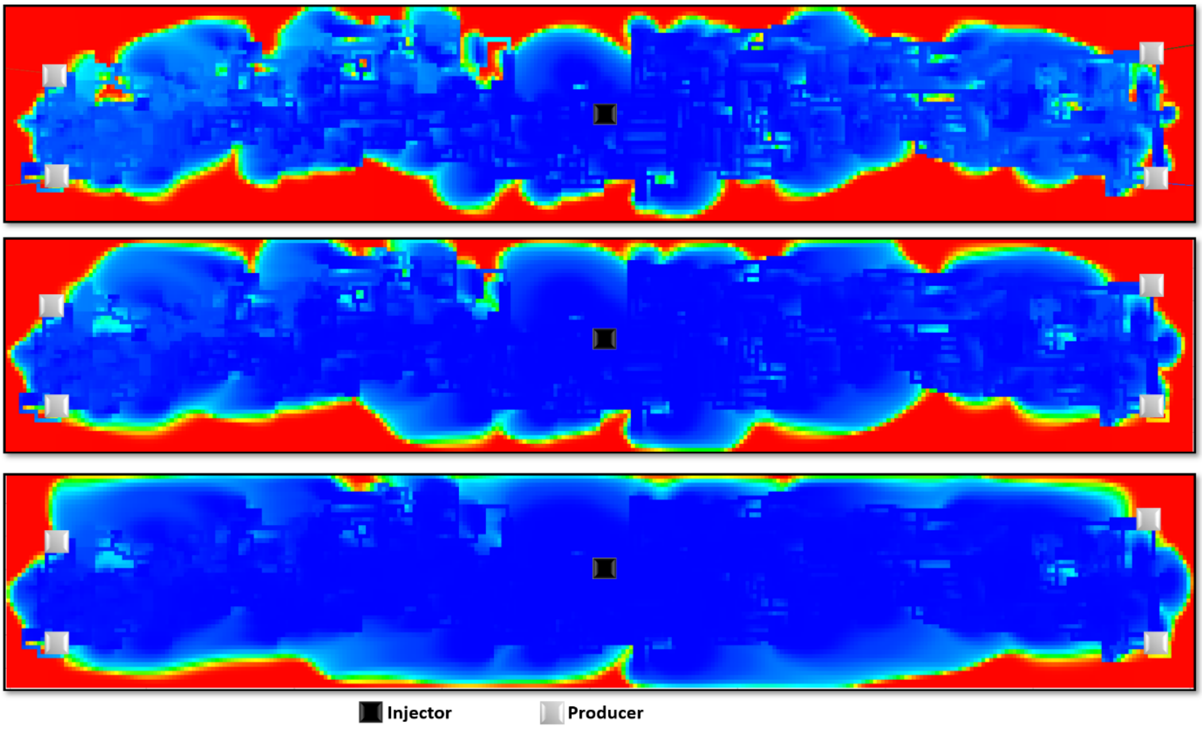

***Figure 3.1-32**: Flow pattern in an inverted 5-spot box model with the producer positioned inside the cave (top) oil saturation after 5 years of production (middle) oil saturation after 10 years of production (bottom) oil saturation after 20 years of production.*

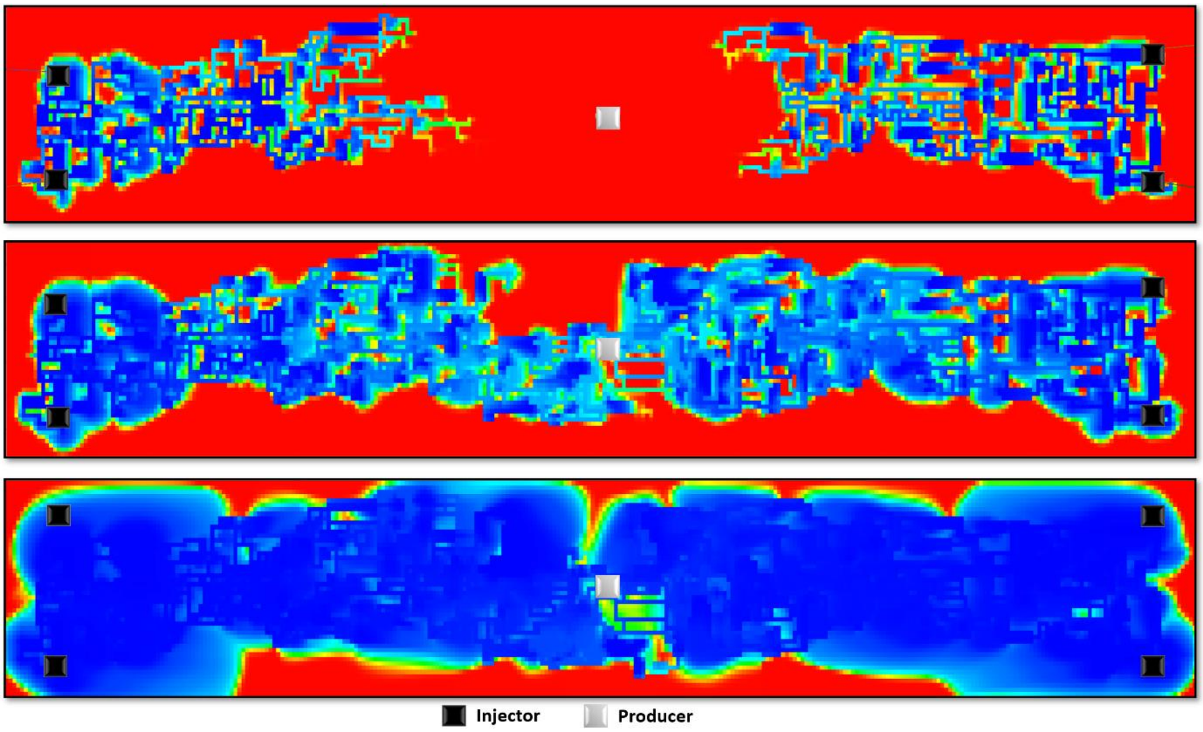

Figure 3.1-33: *Flow pattern in a 5-spot box model with injector wells positioned in cave (top) oil saturation after 5 years of production (middle) oil saturation after 10 years of production (bottom) oil saturation after 20 years of production.*

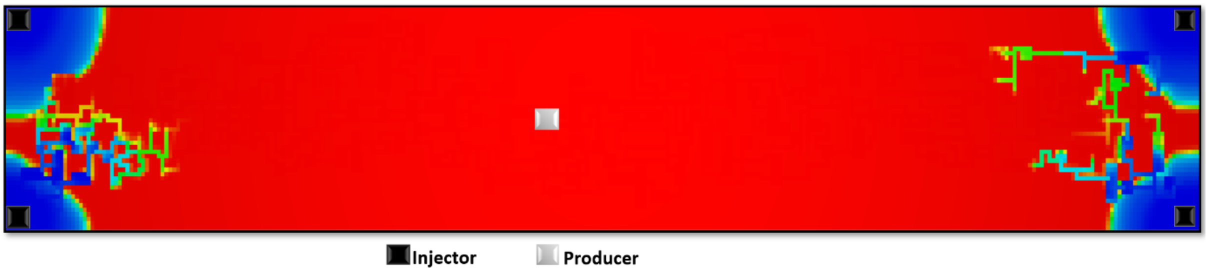

Figure 3.1-34: *Flow pattern in a 5-spot box model with injector wells outside after 5 years of production.*

No production is observed after 5 years if the injectors are placed only in the rock matrix (Figure 3.1-34) because the permeable karst is distal from the heterogeneous karst and host rock is very tight. These are flow barriers that reduce the reservoir pressure significantly. The bottom hole flowing pressure at the wells is not high enough to counter the reduction in reservoir pressure for a long period of time. The injected waterfront expands gradually and flows into the cave geometry only for a short time before production ceases. The production curves for this scenario is shown by a dashed red line in Figure 3.1-35 and Figure 3.1-36.

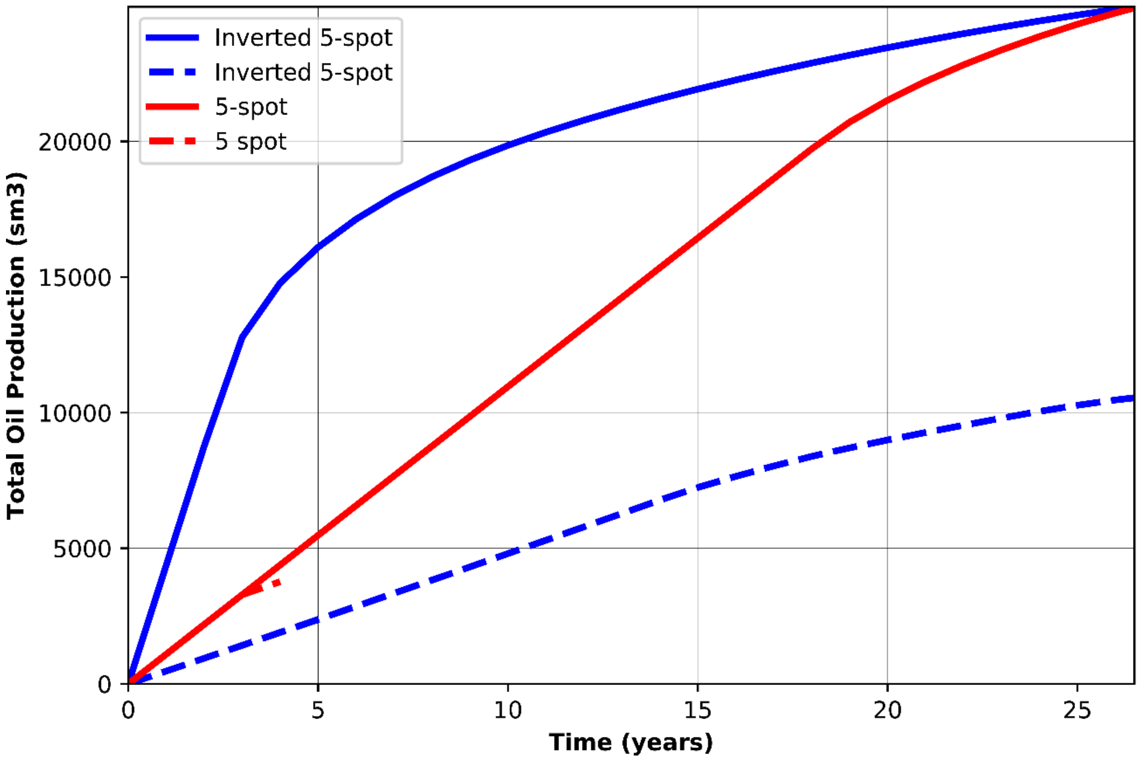

***Figure 3.1-35**: cumulative oil production from both karst (bold line) and matrix (dashed line) using different well patterns.*

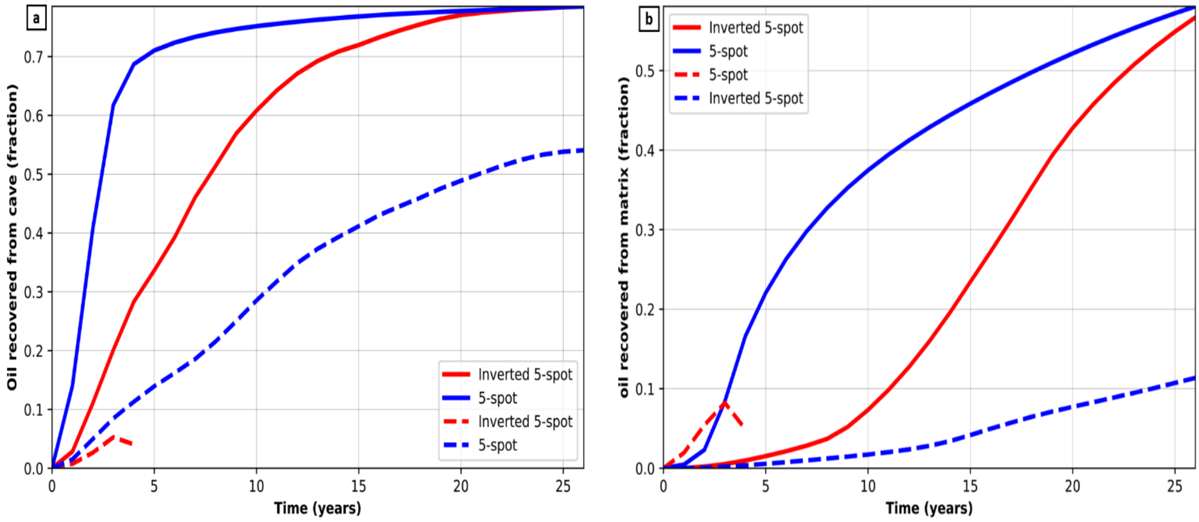

***Figure 3.1-36**: Oil efficiency for both karst (bold lines) and matrix (dashed) using different well patterns.*

3.2 Upscaling

3.2.1 Introduction

Traditional upscaling methods were used for all the generic models in this study because of low computational cost. There has been new development of multiscale upscaling methods of flow simulation in fractured carbonate reservoirs for example Kippe et al. (2008), Popov et al. (2009), Gulbransen et al. (2010), and Alpak et al. (2012). These techniques are used on small scale research studies and are not widely adopted in commercial simulators for large scale reservoir simulation. The most recent successful and fast upscaling methodology for paleokarst carbonate reservoirs is the Embedded Discrete Karst Model (EDKM) by M. Correia et al. (2019). The method involves selectively upscaling the matrix domain in the geological grid while the karst domain with paleokarst features retains the fine scale grid. Communication between the karst-karst and karst to matrix is achieved using a transmissibility multiplier. Transmissibility between karst to karst, karst to matrix is calculated based on the surface area open to flow. The upscaled matrix grid is then merged with the fine scale karst grid to form the EDKM (Figure 3.2-1). On flow simulation, the karst features are preserved at a high resolution.

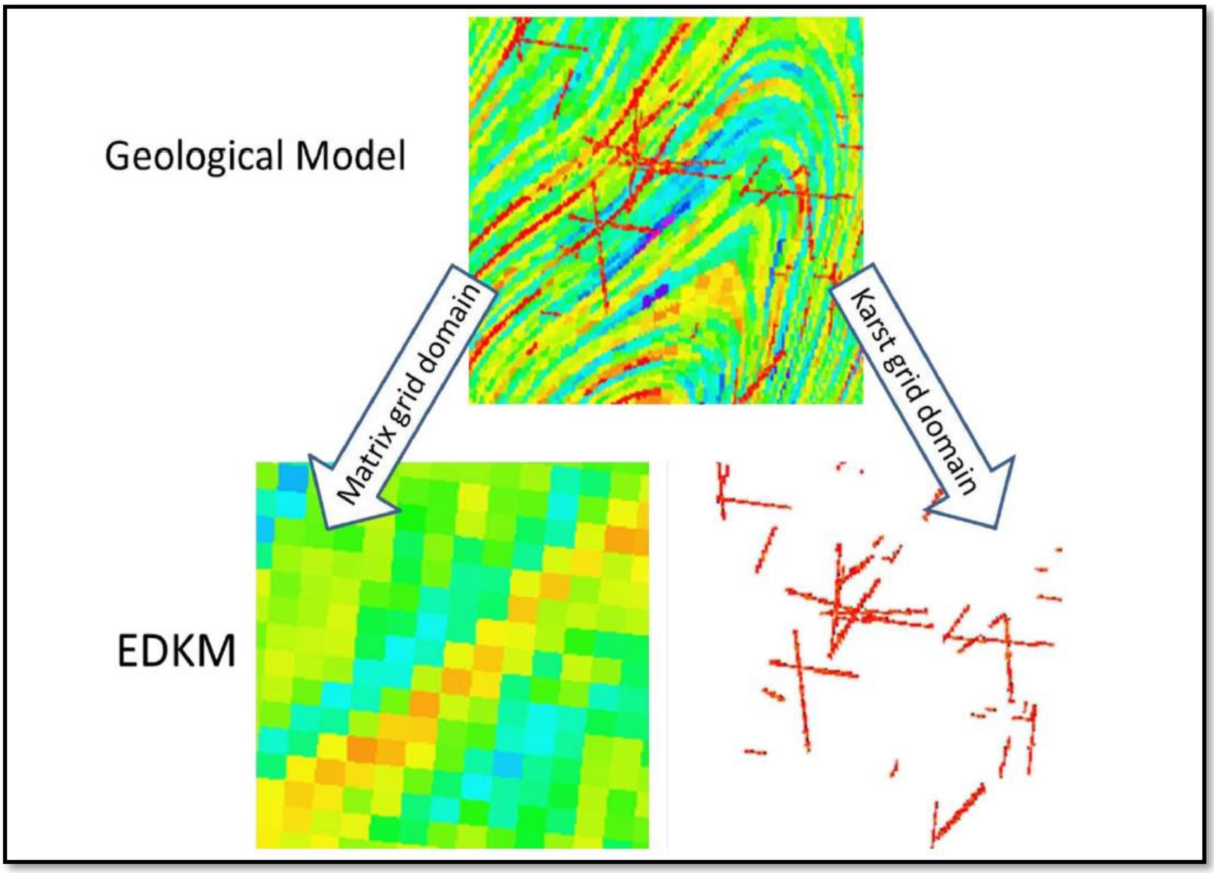

***Figure 3.2-1**: Workflow for the EDKM upscaling technique (M. Correia et al., 2019).*

3.2.3 Upscaling of generic paleokarst reservoir models

The workflow for upscaling I adopted was simple and straight forward because of time constraints and extending the study to other numerical flow simulation methods were deemed to be beyond the scope of the research objectives. First both the matrix grid domain and the karst grid domain are integrated to form the geological grid model. Fractures are excluded in the geological grid. Both the karst and the matrix grid domain have different porosity and permeability. Transmissibility is explicitly computed by the commercial simulator. The geological grid model is then upscaled without separating the karst from the matrix domain. Porosity is averaged using arithmetic averaging methods while permeability is averaged using geometric averaging methods. Lastly, flow simulation is performed using a commercial simulator. The workflow is summarised in Figure 3.2-2.

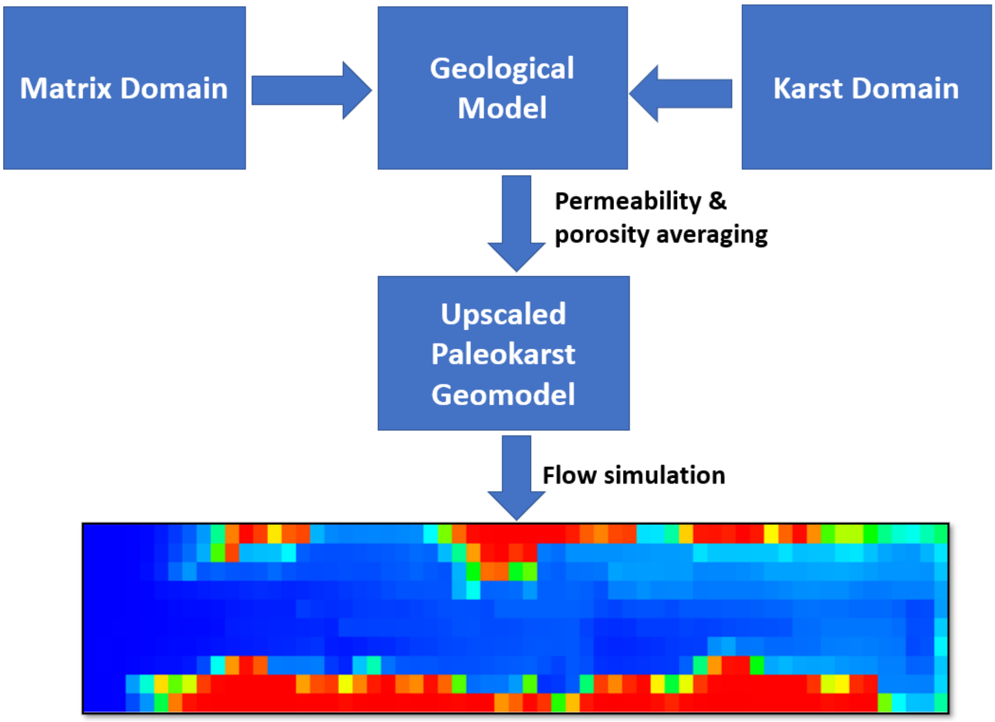

***Figure 3.2-2**: workflow of upscaling methodology adopted in the thesis.*

Upscaling is made by averaging the geological grid in increasing grid sizes of 6 m, 10 m,15 m, and 30 m. The coarsened paleokarst grids may lose vital petrophysical and reservoir flow properties. The fine grid model consisting of 320,250 cells with dimensions of 2 m x 2 m x 2 m is averaged into coarser models of 53,375 cells (6 m x 6 m x 6m), 32,250 (10 m x 10 m x 10 m) and 10,675 cells (30 m x 30 m x 30 m). Before flow simulation was run on the coarser versions, different averaging methods were tested to come up with the best upscaling results that try as much as possible to capture the cave structures and features. Horizontal section in the XY plane (Figure 3.2-3 and Figure 3.2-5) taken at the centre of the paleokarst models reveals that even at the 10 m scale, most cave structures and reservoir flow properties are preserved. However, the cave structures and reservoir flow properties at the 15 m and 30 m scale are smoothened out. Similar contrasts are observed when the coarsened paleokarst models are visualized in the vertical plane (Figure 3.2-4 and Figure 3.2-6).

For the paleokarst model consisting of a very complex cave network, the cave geometry and the original flow pattern are partly preserved after flow simulation in the 6 metres and 10 metres grid cell sizes (Figure 3.2-4 and Figure 3.2-5). But when the upscaling scale is further increased to grid cell sizes of 15 m and 30 m, nearly all the cave features are phased out and the original flow patten exhibited in the finer grid model is almost unrecognisable. This may be attributed to the presence many small passages with sizes between 2-6 m connecting to the bigger cave chambers (greater than 10 m). Also, it should be noted that during the upscaling process, the sampling window will assign a petrophysical value that is closer to the majority of either the non-cave or cave facies. For example, in the 30 m x 30 m x 30 m grid cell, a total 3,375 grid cells of the fine grid model (2 mx 2m x 2m) are averaged into a single coarse cell. If a bigger fraction of the fine grid cells consists of non-cave facies than the cave facies, the coarse cell will take on a lower petrophysical value close to the non-cave. This implies that part of the cave structures smoothens out to nearly match non-cave matrix.

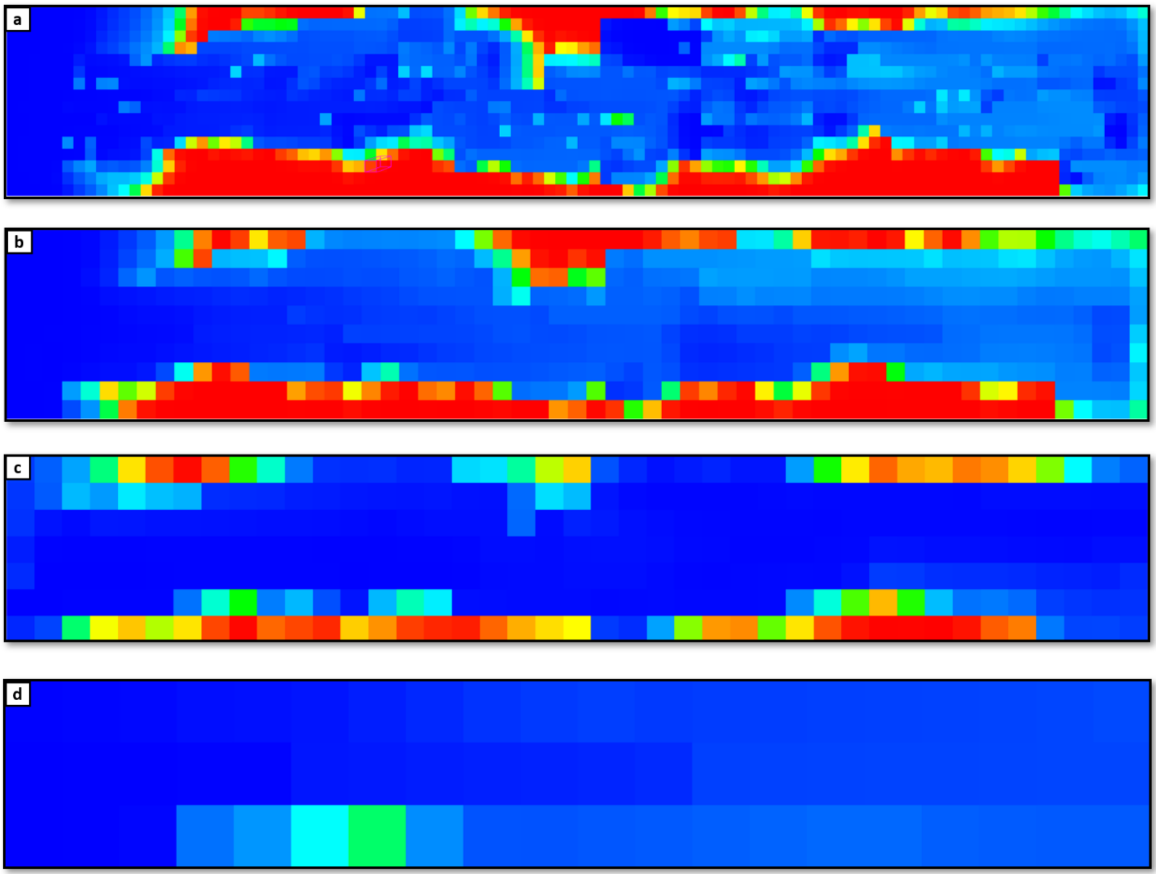

***Figure 3.2-3**: Horizontal sections showing saturation contrasts of the complex paleokarst model at different scale of upscaling done at (a) 6 m grid cell diameter (b) 10 m grid diameter (c) 15 grid cell diameter (d) 30 m grid cell diameter. Note how the cave geometry is smoothened out as the grid diameter is increased.*

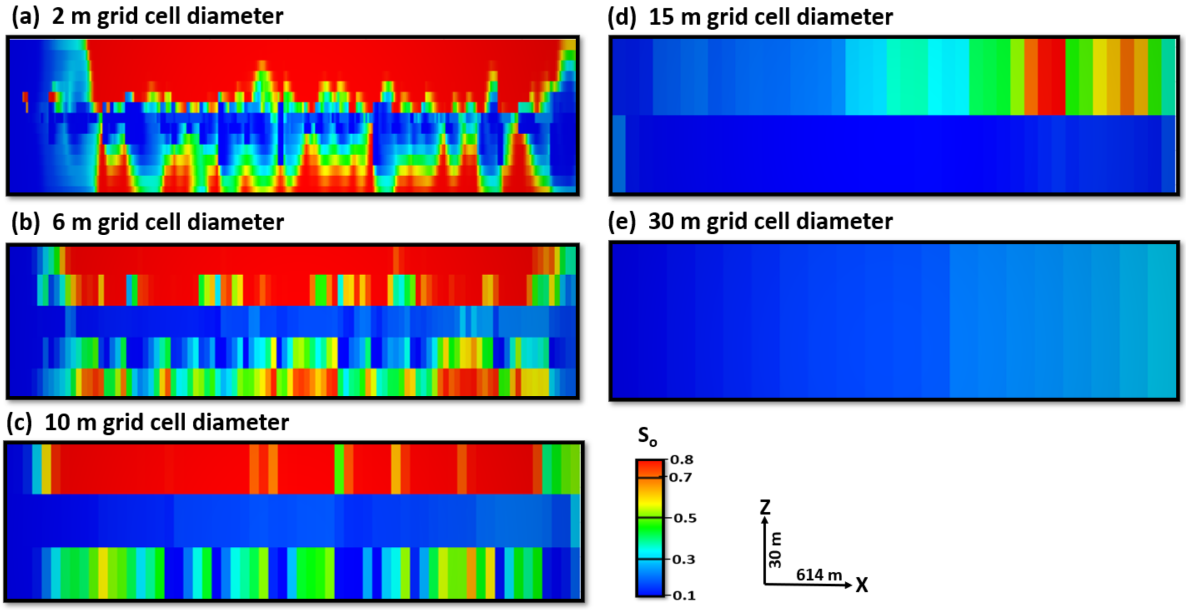

Figure 3.2-4: *Vertical sections showing saturation contrasts of the complex paleokarst model at different scale of upscaling done at (a) 2 m grid cell diameter (b) 6 m grid diameter (c) 10 m grid cell diameter (d) 15 m grid cell diameter (e) 30 m grid cell diameter.*

When the fine paleokarst model with simple cave geometry is upscaled, most of the cave structures and the fluid flow patterns are fairly captured up to a 15-metre grid scale as shown in the horizontal and vertical sections displayed in Figure 3.2-5 and Figure 3.2-6, respectively. Above 15 m, the cave structures and the flow path are smoothened out and becomes homogeneous. This happens because the fine scale version of the model consists of mainly bigger cave passages above 6 metres with only one passage of 2 metres, and with fewer branching networks. On grid coarsening, the resulting grid of the cave system will contain a petrophysical value closer to that of the cave facies than the matrix facies. If the value of the petrophysical property is higher than that of the fine non-cave cells, then the resulting cell captures the petrophysical properties. However, at 30 m grid scale the averaging window contains more of non-facies cells and thus petrophysics values of the cave facies are averaged to a value much lower than the cave facies in the fine grid model.

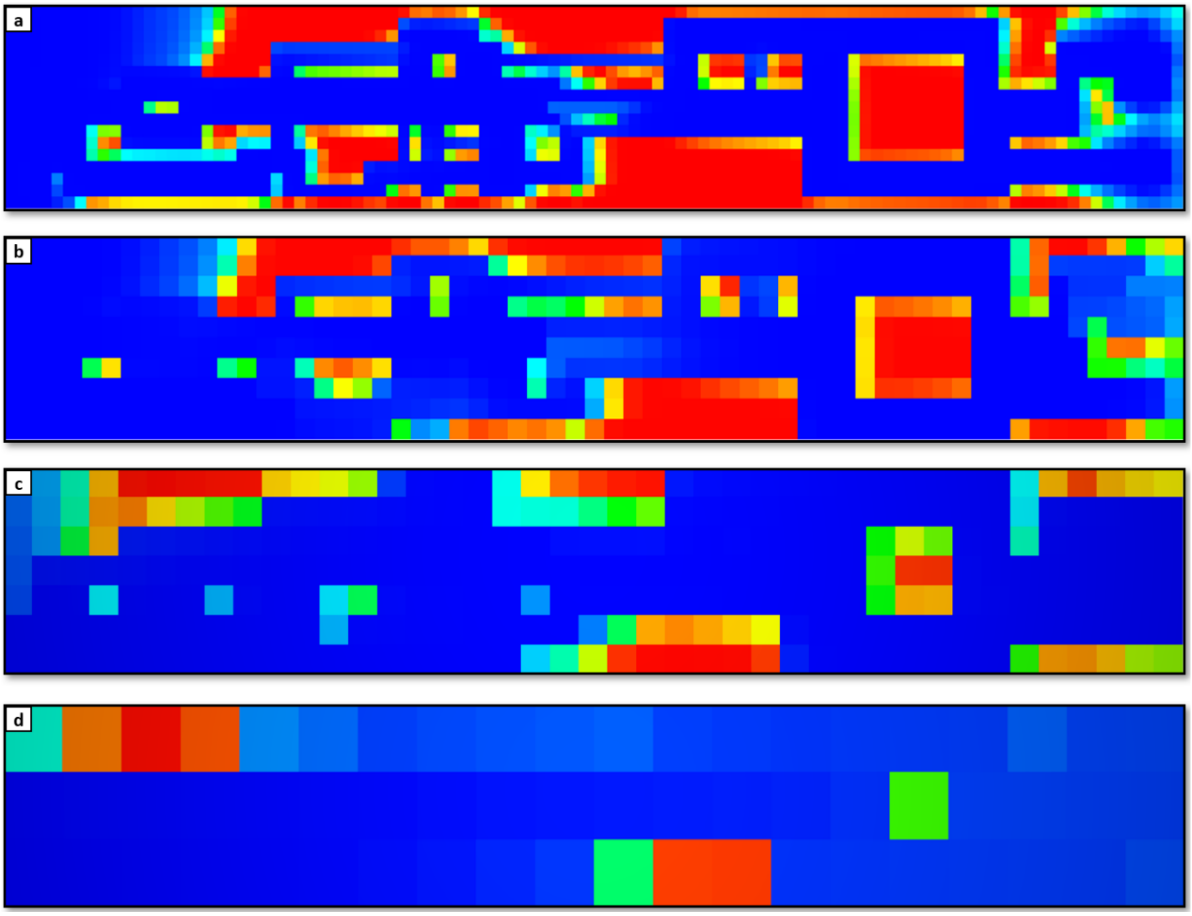

Figure 3.2-5: *Horizontal sections showing saturation contrasts of the simple paleokarst model at different scale of upscaling done at (a) 6 m grid cell diameter (b) 10 m grid diameter (c) 15 m grid cell diameter (d) 30 m grid cell diameter. Note how the cave geometry is smoothened out as the grid diameter is increased.*

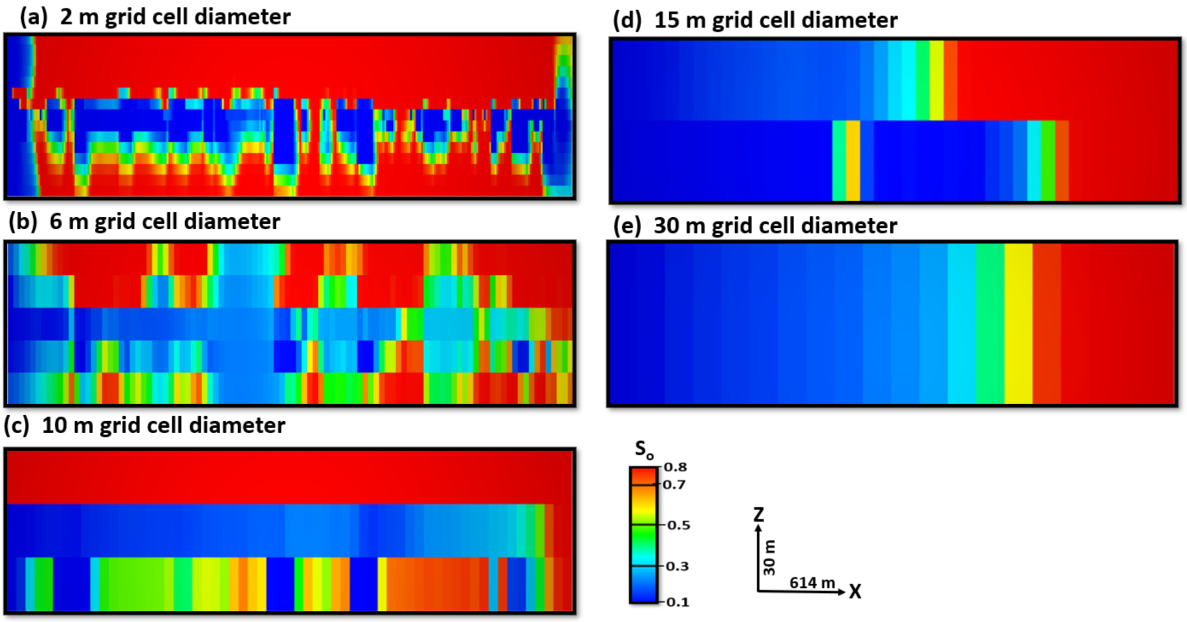

Figure 3.2-6: *Vertical sections showing saturation contrasts of the complex paleokarst model at different scale of upscaling done at (a) 2 m grid cell diameter (b) 6 m grid diameter (c) 10 m grid cell diameter (d) 15 m grid cell diameter (e) 30 m grid cell diameter. Note how the cave geometry is smoothened out as the grid diameter is increased.*

The difficult associated with capturing cave structures during upscaling can influence oil production and water cut forecasting. The total oil production (Figure 3.2-7 and Figure 3.2-8) and total water cut (Figure 3.2-9 and Figure 3.2-10) from the upscaled versions simple and complex paleokarst models is generally overestimated as compared to the fine models. The overestimation is not random but rather observed to increase with the grid coarsening scale. Regardless of the forecasting problem, it is notable that overall, the coarsened versions of the simple paleokarst model give better production results relative to the finer version at a coarsening scale of 6-15 metres than the complex paleokarst model. However, in both cases grid coarsening to 30 metres overestimates the total production by the highest magnitude irrespective of the cave geometry. This happens because 30 metres grid size upscaling averages the entire payzone including the biggest cave passages of size 18 metres. The same trend is observed in the water cut plots. In both cases, the water breakthrough is prolonged as the coarsening scale is increased. This is a false observation and may imply that water break through happens early than expected ceasing production and need to drill new wells or do a different oil recovery technique.

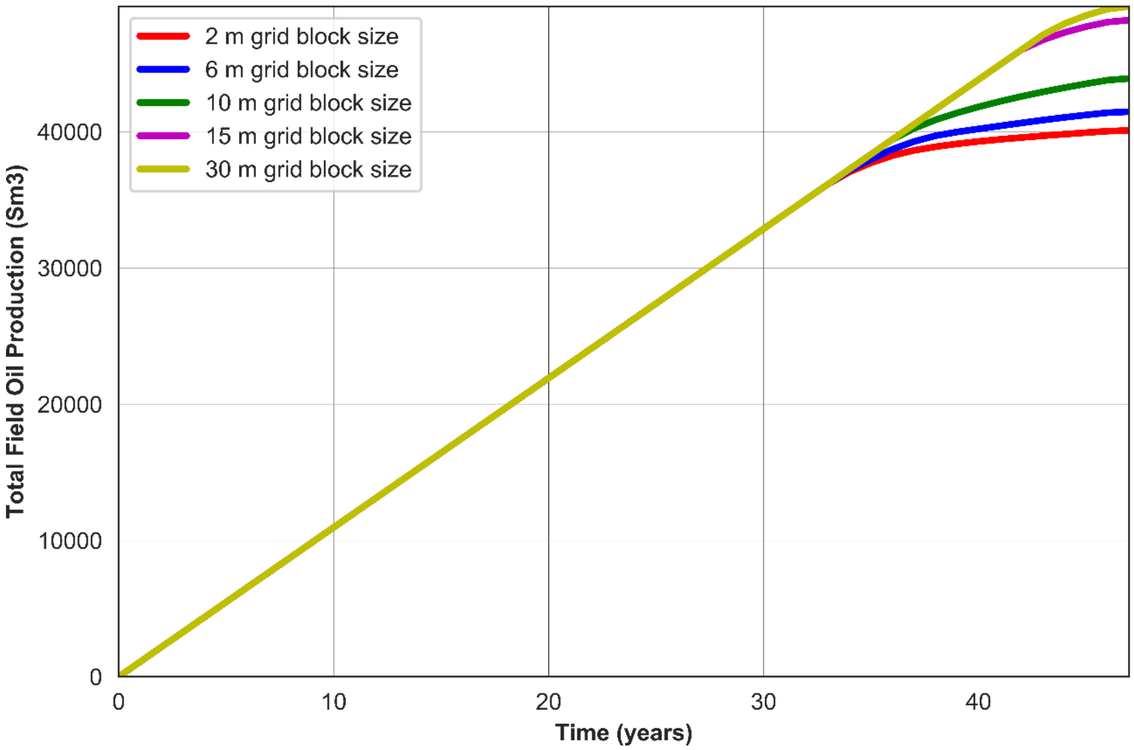

Figure 3.2-7*: Cumulative oil production comparing a fine grid complex paleokarst model and its respective upscaled versions.*

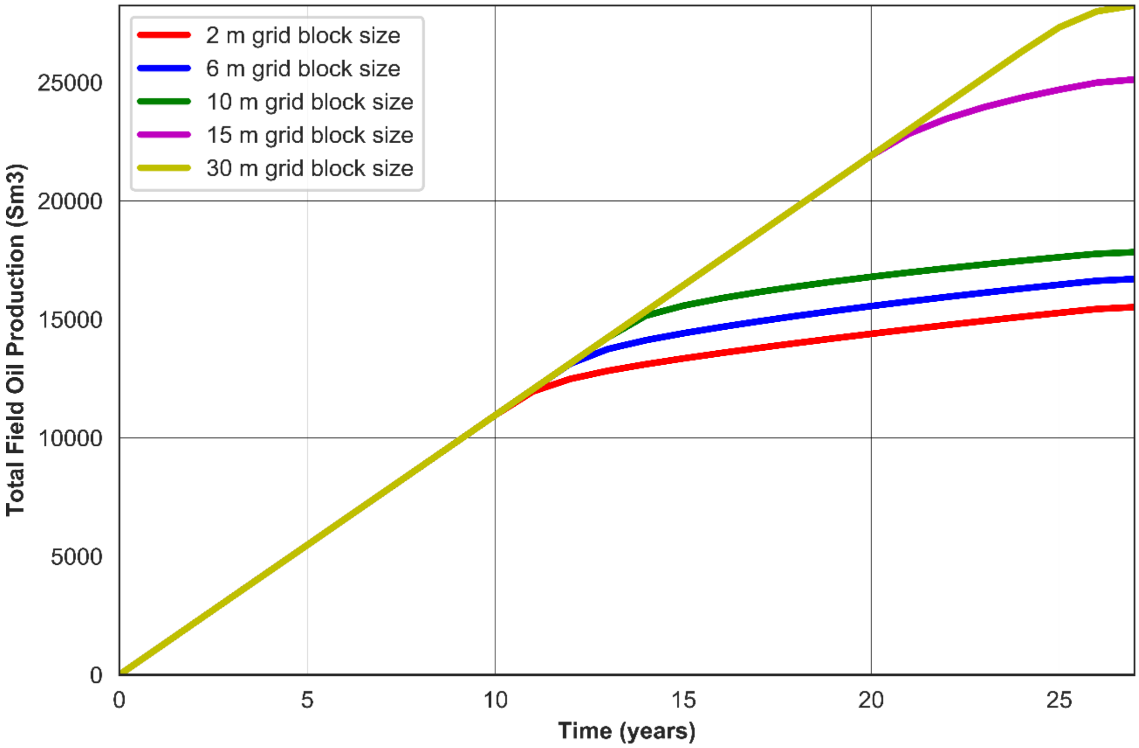

Figure 3.2-8: *Cumulative oil production comparing a fine grid simple paleokarst model and its respective upscaled versions.*

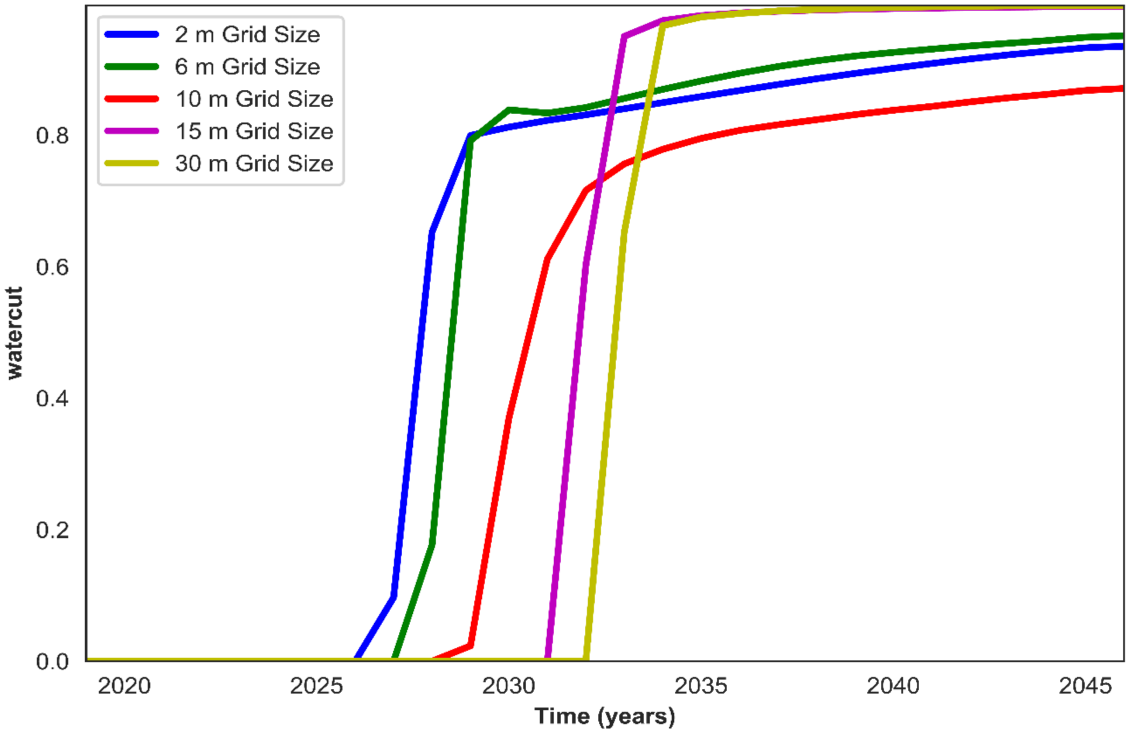

Figure 3.2-9*: A plot showing a comparison of watercut from fine grid and the courser grids of the complex paleokarst model.*

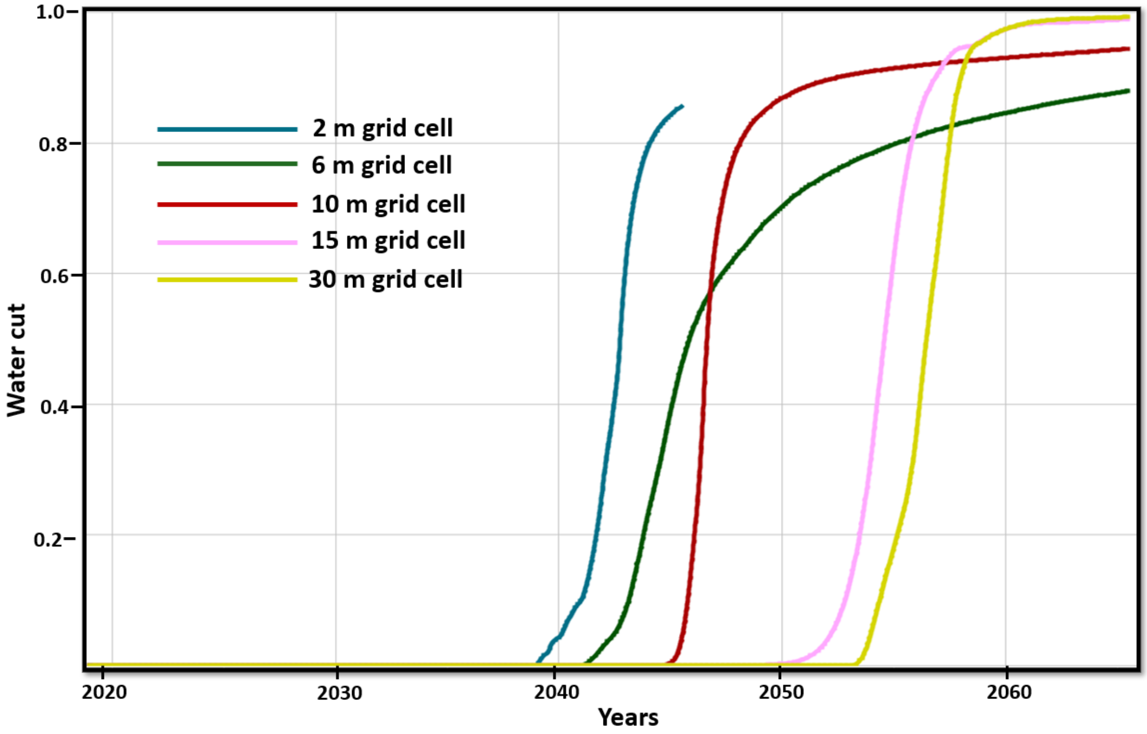

Figure 3.2-10*: A plot showing a comparison of watercut from fine grid and the courser grids of the simple paleokarst model.*

3.3 4D Seismic

This section represents results from steps that were used to model 4D seismic of the simple paleokarst model.

3.3.1 Rock physics modelling

The geological information used to build model the rock properties of the paleokarst model I used were adopted from the Franklin Mountains paleocaves, USA (Målbakken, 2009) and Setergrotta cave, Norway (Johansen, 2018). The rock physics models (Table 3.3-2) convert dynamic reservoir properties such as porosity, pressure, and fluid saturation from the flow simulation model into dynamic elastic properties such as elastic moduli and density. Other properties that are defined are temperature (60^0C), pore pressure (20 GPa) and effective reservoir pressure (20 GPa). The fluid properties are set to depend on the fluid composition, temperature, and salinity. In this study, water and oil were considered as pore fluids. The reservoir is filled with oil of density 0.8762 g/cm^3 while the density of the injected water is 1.0 g/cm^3. The critical porosity is set at 40% and the cement volume at 5% to match properties described by Avseth et al. (2010). Two porosity values of 0.02 and 0.2 are used to differentiate between the non-cave and the cave regions, respectively. The porosities also represent the pore geometry and reflect cave sizes. The rock units in the caves of the paleocave reservoir model consist of either a mixture of dolomite or limestone, and either dolomite or limestone only. The elastic moduli and densities of the solid composite consisting of dolomite and calcite are displayed in Table 3.3-1.

Table 3.3-1: Elastic moduli and densities of a two mineral component adopted in the rock physics models (Johansen, 2018).

Rock	Bulk modulus (GPa)	Shear modulus (GPa)	Density (g/cm^3)
Dolomite	76.8	32.0	2.71
Calcite	76.4	49.7	2.87

Table 3.3-2*: An overview of different rock models used in the rock physics modelling* ***(Johansen, 2018).***

Rock model	Lithology	Depth (m)	Description	Fluid Saturation	Porosity
Model 1	Dolomite	1500-1506	no cave	100% oil	0.02
Model 2	Dolomite/Limestone	1506-1520	cave/no-cave	100% oil	0.02-0.2
Model 4	Limestone	1524-1526	no cave	100% oil	0.02
Model 7	Limestone	1524-1530	no cave	100% oil	0.02

The rock models 1, 2, 4 and 7 are adopted to create density contrasts in the input model in respect to depth so that during wave propagation the different regions are visible in seismic because of change in acoustic impedance. Model 1, 4 and 7 represents homogeneous layers devoid of karst above and below the cave. Model 1 lies above the cave region and comprises 75% dolomite and 25% limestone while Model 4 is a thin layer of 2 m consisting 80% limestone and 20% dolomite below the cave and above Model 7. Model 7 represents lithology below Model 4 and comprises of 80% dolomite and 20% limestone. Model 2 represents the region with both the cave and other background lithology and consists of 50% dolomite and 50% limestone. The criterion for assigning the lithology depends on the relative abundance of one mineral composition over the other in a mixture such as the model takes on the name of a mineral with a composition greater than 50%. Results from rock physics modelling showing how the bulk modulus, shear modulus, density, Vp, and Vs changes with porosity in the 3D simple paleokarst model are displayed in Figure 3.3-1, Figure 3.3-2, Figure 3.3-3, Figure 3.3-4, and Figure 3.3-5, respectively.

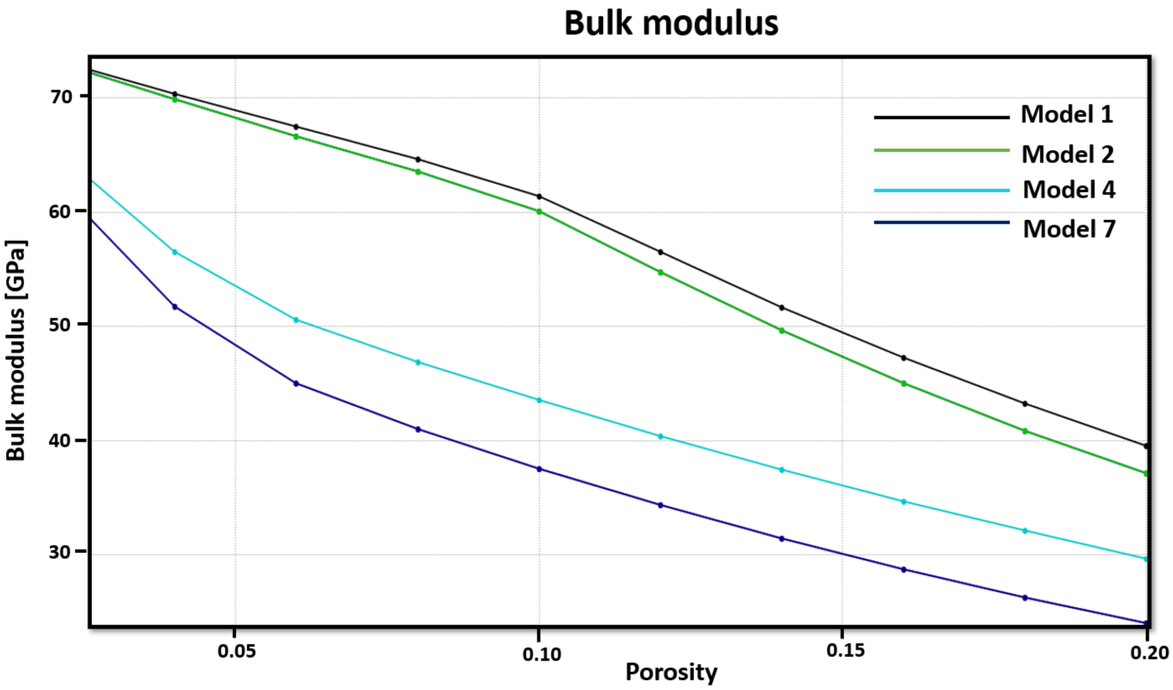

Figure 3.3-1: *A plot of bulk modulus versus porosity for the different rock physics models used to represent the cave region and the non-cave region. The bold lines represent distribution of bulk modulus in the 3D simple paleokarst model. There is a general decrease in bulk modulus as the porosity increases for all the rock models.*

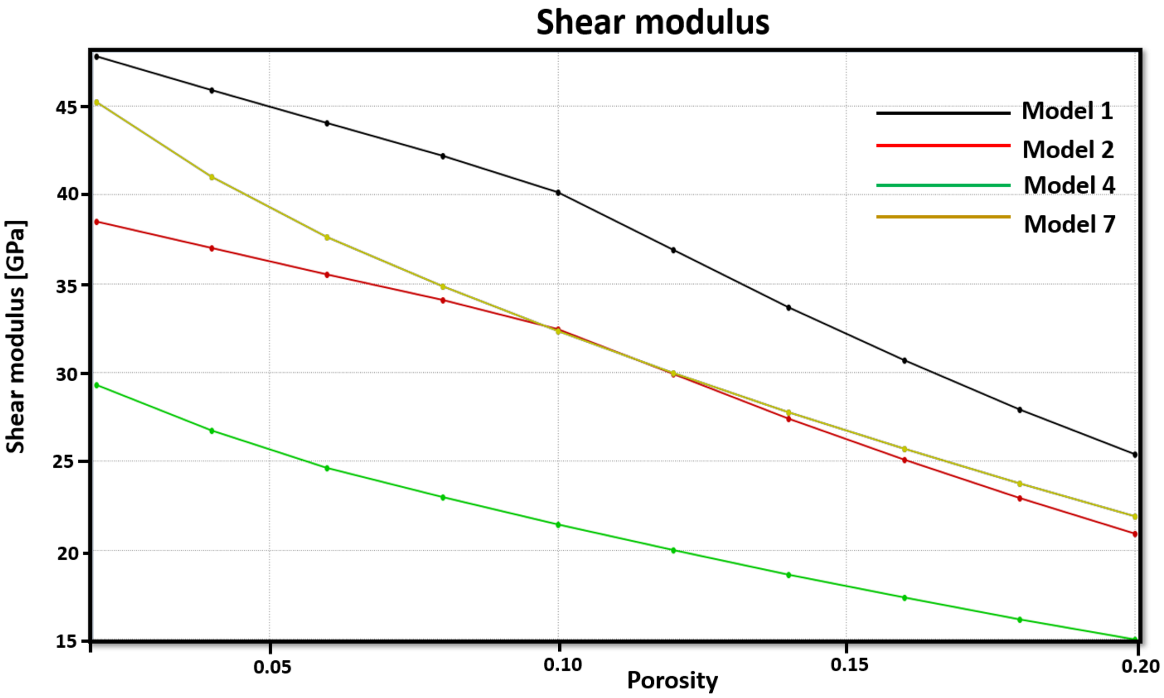

Figure 3.3-2*: A plot of shear modulus versus porosity for the different rock physics models used to represent the cave region and the non-cave region. The bold lines represent distribution of shear modulus in the 3D simple paleokarst model. The trend is similar with that observed in Figure 3.3-2 except that model 2 and model 7 merge shortly and decrease with a small difference after a porosity value of 0.1.*

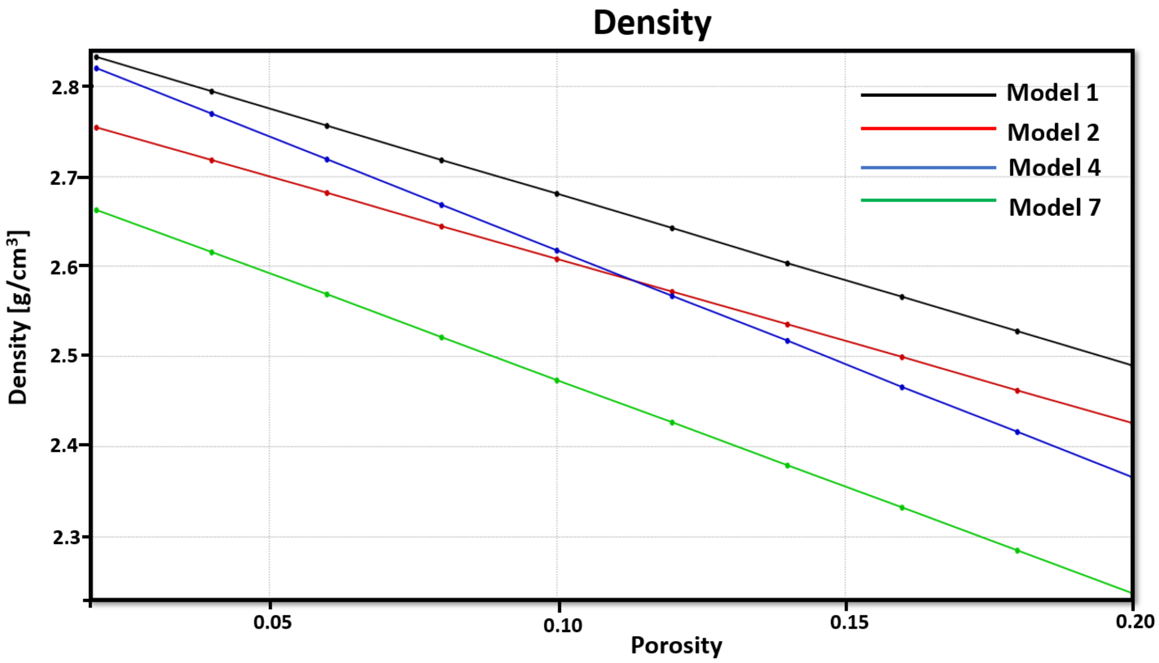

Figure 3.3-3*: A plot of rock density against porosity for the different rock physics models used to represent the cave region and the non-cave region. The bold lines represent distribution of rock density in the 3D simple paleokarst model. There is an overall constant decrease in rock density with increasing porosity.*

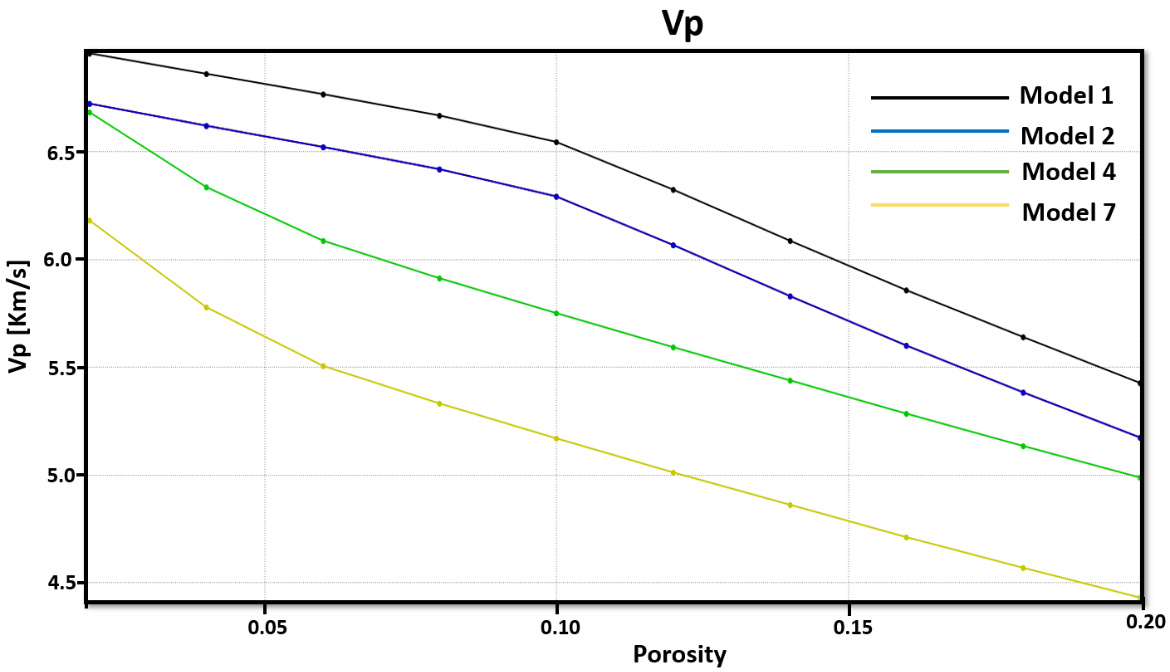

***Figure 3.3-4**: A plot of Vp versus porosity for the different rock physics models used to represent the cave region and the non-cave region. The bold lines represent distribution of bulk modulus in the 3D simple paleokarst model. There is a constant decrease of Vp with increasing porosity expect for model 7 where the decrease is sharp before a porosity value of 0.1.*

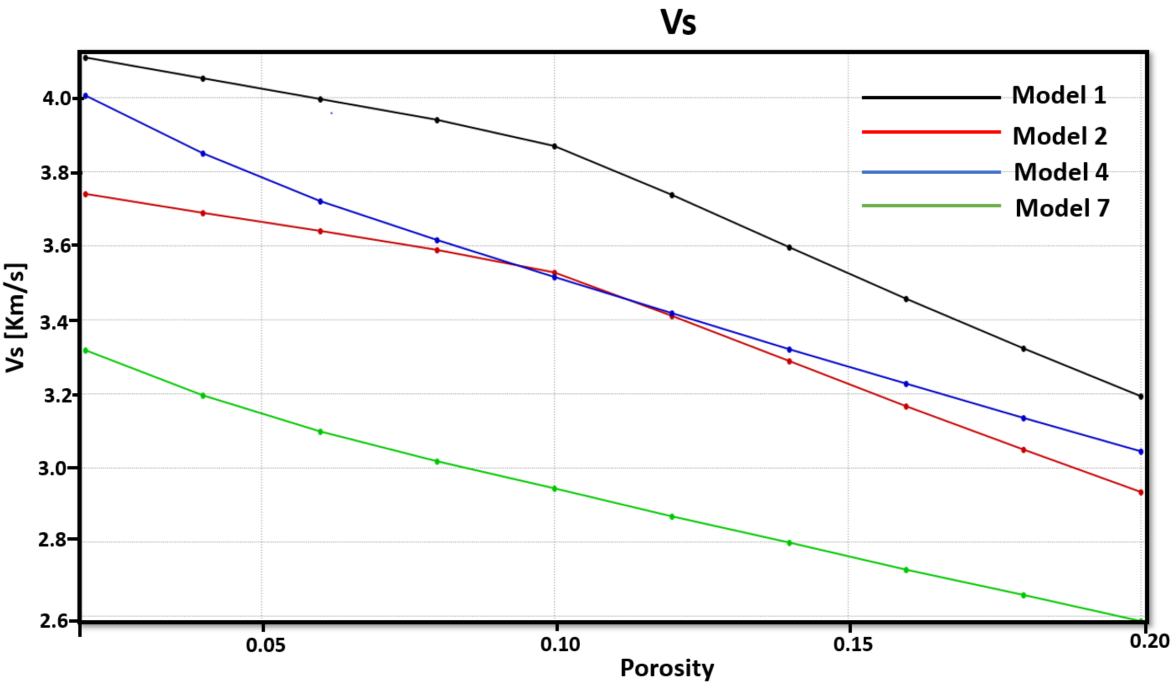

Figure 3.3-5*: A plot of Vs against porosity for the different rock physics models used to represent the cave region and the non-cave region. The bold lines represent distribution of bulk modulus in the 3D simple paleokarst model. There is a constant decrease of Vs with increasing porosity expect for model 2 crossing model 4 towards 0.1 mD before decreasing further to a value lower than that of model 4.*

3.3.2 Seismic modelling

Seismic modelling simulates elastic wave propagation in models of the subsurface using the wave equation and generates seismic wavefield, seismic amplitudes, or seismic travel times. Complex geological structures in both siliciclastic and carbonates can then be studied by analysing and comparing synthetic seismic with actual seismic data. The so-called full-waveform seismic modelling approaches, such as finite-difference solutions of the wave equation, should be adopted to produce complete seismograms whenever possible, if computing cost is not an issue. Other approaches, such as ray-based ones, including convolution methods, can be used instead when flexibility and efficiency are important (Lecomte et al., 2015). The modelling method applied in the present work is a 3D Point-Spread Function (PSF) based convolution (Lecomte et al., 2003; Lecomte et al., 2016). To generate the input models for seismic modelling, rock physics transformations of reservoir parameters yield the necessary elastic parameters as described earlier: In the following, the studied models have a 2 m sampling for the simulation grid. The derived elastic properties are then used to generate synthetic seismic cubes. In the following, the synthetic seismic represents elastic wave responses to acoustic impedance contrasts but in cases with non-zero incident angle, the S-wave velocity matters and it is no longer just an acoustic impedance contrast.

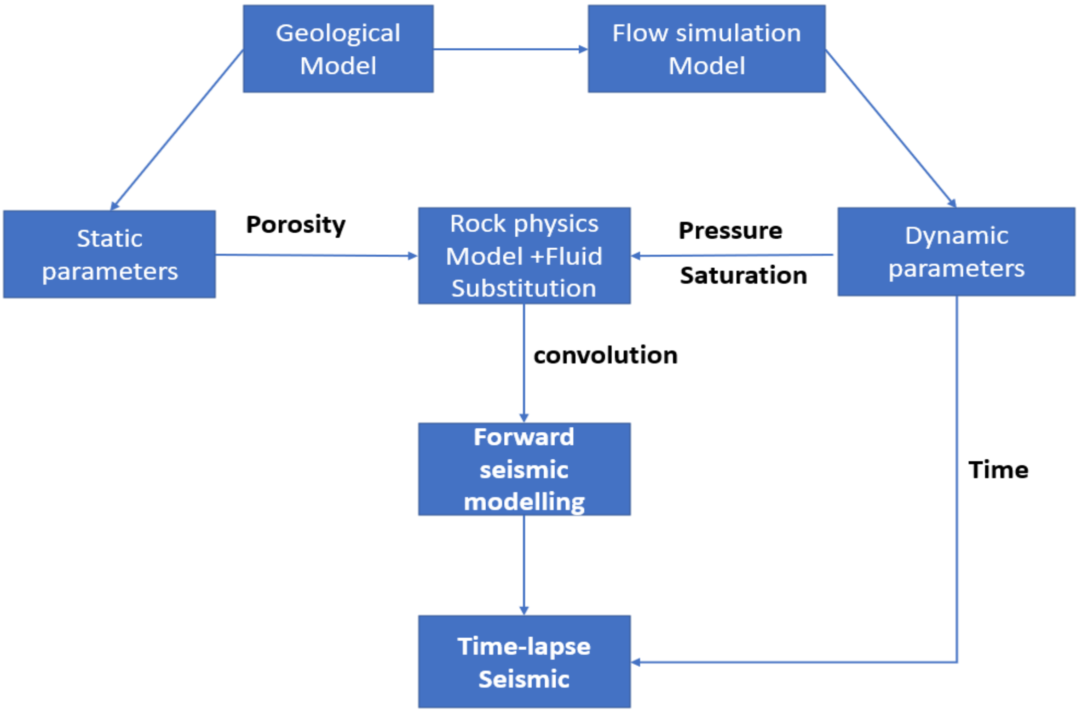

***Figure 3.3-6**: Workflow from flow simulation to seismic modelling of generic paleokarst carbonate reservoirs.*

The first step of synthetic modelling in the workflow (Figure 3.3-6) is to extract a simulation grid, with static parameters from the geomodel and dynamic parameters from the flow simulation model. The parameters are porosity, fluid saturation, pressure, and production time steps. The subsequent step involves rock physics modelling with fluid substitution during water injection. Rock physics modelling and fluid substitution steps converts dynamic reservoir properties such as pressure and saturation to dynamic elastic properties such as density and seismic velocities (both P- and S-wave) as a function of pore pressure and fluid saturation, here based on both Hertz-Mindlin and Gassmann's fluid substitution equations (Johansen, 2018). The Gassmann's equation assumes constant reservoir rock porosity values and is sensitive to fluid substitution, while the Hertz-Mindlin equation models the critical porosity. Critical porosity of carbonates is considered to be higher than 40% and is highly influenced by the mineral type, rock texture, and depositional diagenetic properties (Mavko et al. (2009). Finally, seismic modelling calculates synthetic seismic cubes using a 3D PSF-based convolution. The PSF applied in the present work is just estimated via a few key parameters (wavelet, average velocity, incident angle, and maximum illuminated geological dip angle) as neither a specific overburden model nor a given seismic survey geometry are considered here (Lecomte et al., 2016). Repeating seismic modelling for different time steps produces so-called time-lapse or 4D seismic entailing detecting anomalies corresponding to changes in water saturation and elastic properties during the reservoir simulation. Note that the seismic modelling method used here produces 3D seismic cubes in the depth domain, equivalent to cubes obtained by Pre-Stack Depth Migration (PSDM). Horizontal sections extracted from these cubes will thus be at a given depth.

Fluid substitution

To compute changes in elastic parameters caused by water injection into the paleokarst reservoir formations, fluid substitution modelling is employed. Fluid substitution is based on the Gassmann's equation (8), linking bulk modulus of a saturated rock to the pore, rock frame and fluid properties (Gassmann, 1951):

$$K_{sat(new)} = K_{dry} + \frac{[1-(K_{dry}/K_{m)})]^2}{\left(\frac{\emptyset}{K_{fluid(new)}}\right) + \left(\frac{1-\emptyset}{K_m}\right) + \left(\frac{K_{dry}}{K_m^2}\right)} , \qquad (8)$$

where K_{sat}, K_{dry}, K_m, and K_{fluid} are the bulk moduli of the saturated rock, porous rock frame (drained of any pore-filling fluid), mineral matrix, and pore fluid, respectively, and Is porosity (as fraction). The matrix bulk modulus (K_m) represents the mineral composition of the rock and is calculated by either the Voigt-Reuss-Hill method (Hill, 1952) or using the Hashin-Shtrinkman method (Hashin et al., 1963).

3.3.3 Seismic modelling of the simple generic paleokarst model

The 3D simple generic paleokarst model is a symmetric reservoir model consisting of 15 horizontal layers measuring an area of 614 x 100 m^2 and a total thickness of 30 m. The input parameters considered for the seismic modelling process are displayed in Table 3.3-3. A cube sampling of 2 m, a Ricker wavelet of 45 Hz dominant frequency and an average velocity of 3.5 km/s in the target area were used to model a reasonable seismic response. The maximum reflector dip of 45 degrees corresponds to a more realistic illumination angle where all layers that are flattish or tilted are in seismic up to an inclination of 45 degrees while the incident angle range of 0◦-30◦ represent variation of source-receiver offset with 0◦ representing incident angle at zero offset. Beyond 30◦, the incidence becomes overcritical and cannot be used in reflection seismic (Figure 3.3-7).

Table 3.3-3: Input parameters used for synthetic seismic modelling.

Maximum illuminated reflector dip	45◦
Average velocity in the target model	3.5 km/s
Incident angle	0-30◦
Wavelet	Ricker: 45 Hz
Reflection model	P-P

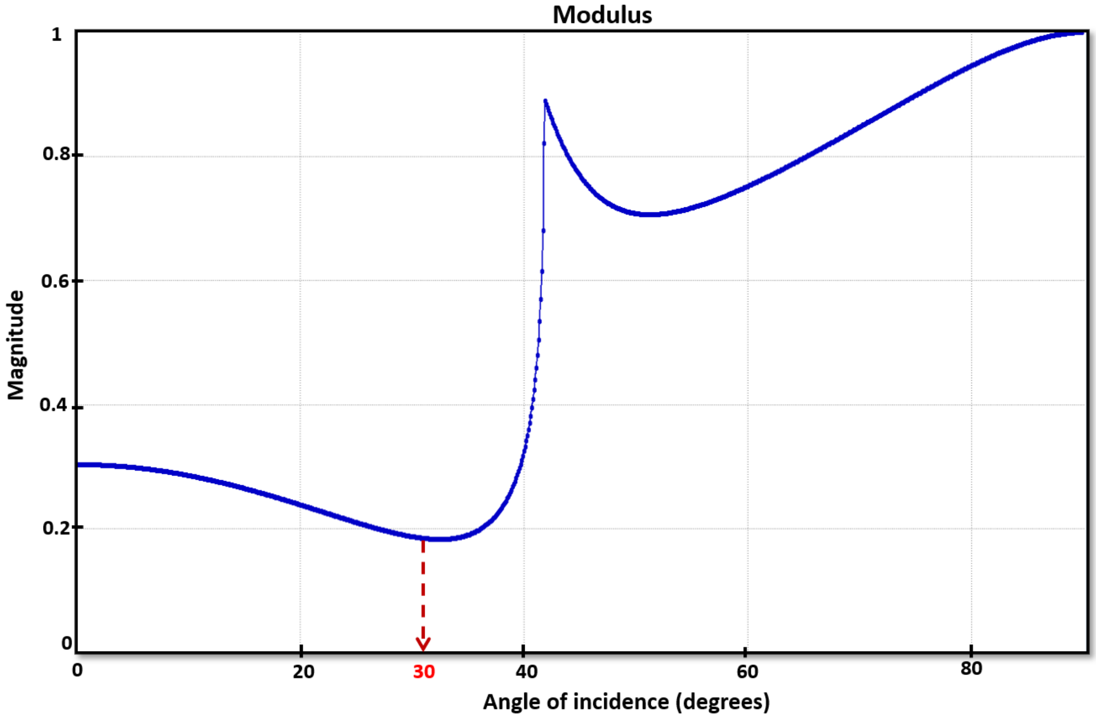

Figure 3.3-7*: A plot showing the modulus of the reflection coefficient from 0 to 30 degrees. The strongest reflection coefficient is at 0 degrees and weakest at 30 degrees (dashed line).*

The reflection coefficient changes with the incident angle, and that it is strongest at the 0-deg incident angle and weakest at the 30-deg. The choice of a seismic slice should therefore be considered at 0-deg and where the seismic amplitude is high (Figure 3.3-8).

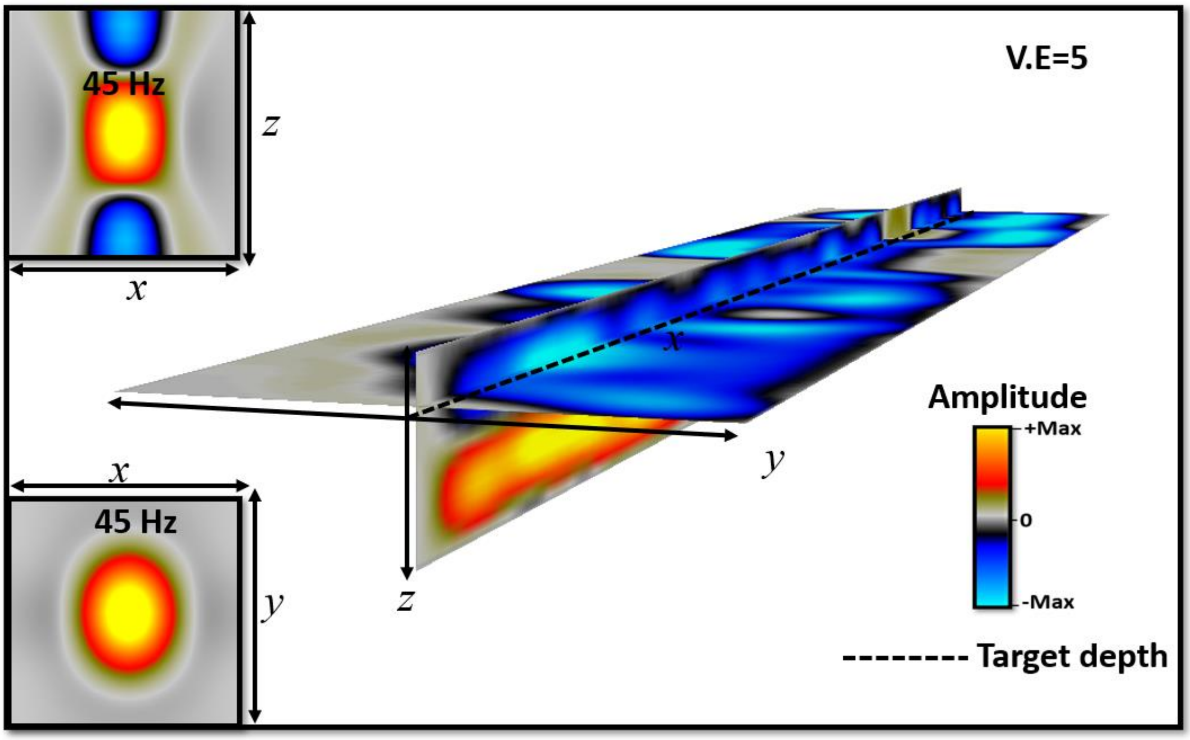

***Figure 3.3-8**: A horizontal slice at depth z=1508 m and vertical slice at y=50 m through 3D volume (614 x 100 x 30 m^3) visualized in XY plane (dashed line). Notice the high negative amplitude at the top of the reservoir. A vertical exaggeration of 5 was used.*

A Further step is therefore taken to compare the relative amplitude is outstanding as shown by seismic sections and overlays of seismic and reflectivity. Different horizontal synthetic seismic section of incident angle ranges taken at 0◦,10◦, and 30◦ degrees are displayed in Figure 3.3-9 while a superimposed vertical section of seismic and reflectivity is displayed in Figure 3.3-10. All these sections are in relative comparations of amplitude or reflectivity with increasing angle of incidence. At zero offset, there is a high negative amplitude at the top of the reservoir, a high negative amplitude is observed at the bottom of the reservoir while very low to zero amplitude is visible in the middle of the cave. When the incident angle is increased to 10◦, the relative seismic amplitude decreases moderately for all cases. At 30◦ incident angle, the seismic resolution is at its poorest. Smearing of the edges of the seismic section also occurs at 30◦ as shown in Figure 3.3-11. There is no smearing of the reflectors at 0◦.

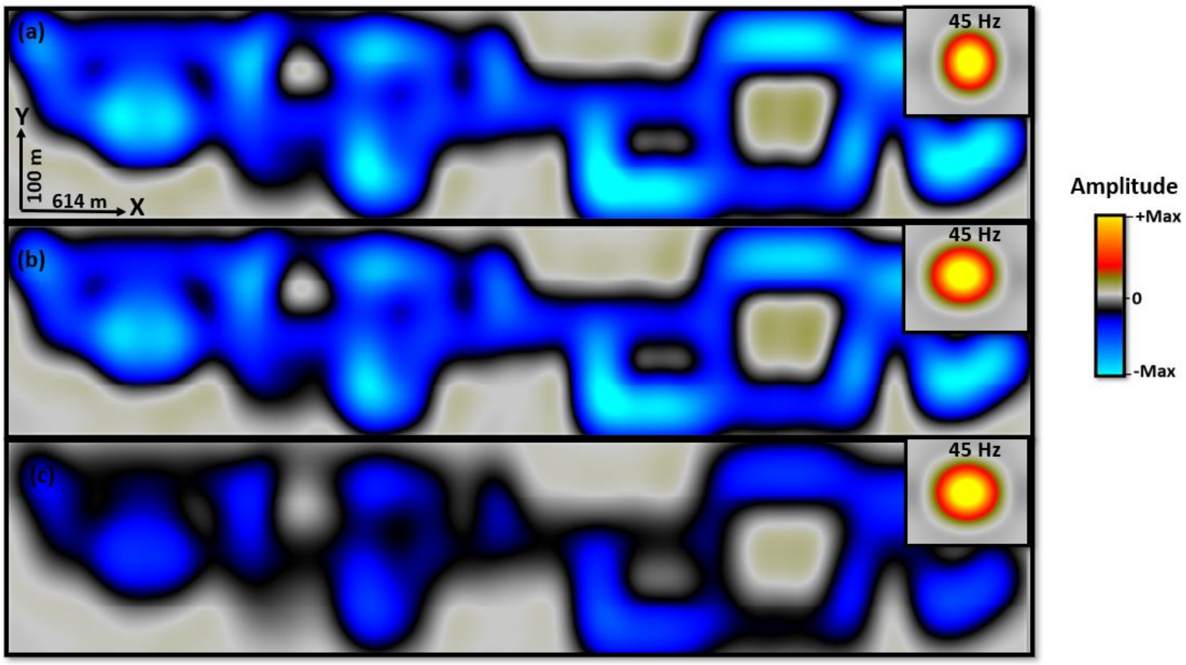

Figure 3.3-9: *Horizontal slices (at z=1508 m) displaying synthetic seismic at the top of the simple paleokarst reservoir at (a) incident angle = 0◦ (b) incident angle = 10◦ (c) incident angle = 30◦. The PSF is displayed on the extreme right-side corner of the individual seismic sections. The PSF is sharpest at the zero-degree incident angle whereas it becomes wider and bigger with increase in the angle of incidence.*

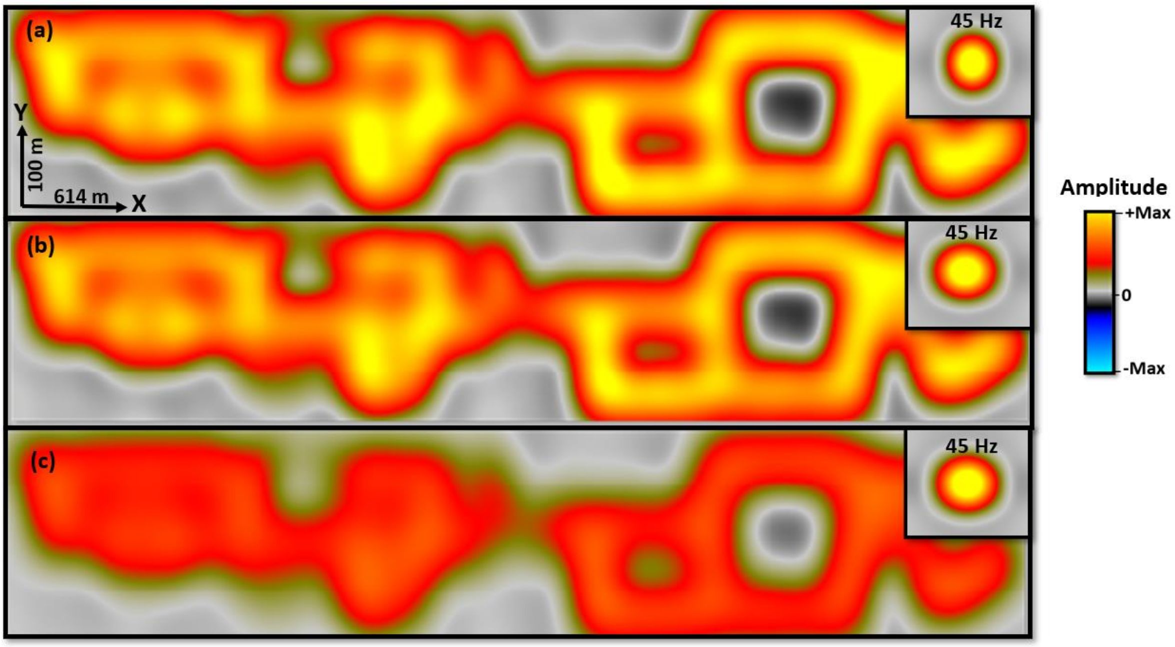

Figure 3.3-10: *Horizontal slices (at z=1524 m) displaying synthetic seismic at the bottom of the simple paleokarst reservoir showing relative amplitudes at (a) incident angle = 0◦ (b) incident angle = 10◦ (c) incident angle = 30◦. The PSF is displayed on the extreme right-side*

corner of the individual seismic sections. The PSF is sharpest at the zero-degree incident angle whereas it becomes wider and bigger with increase in the angle of incidence.

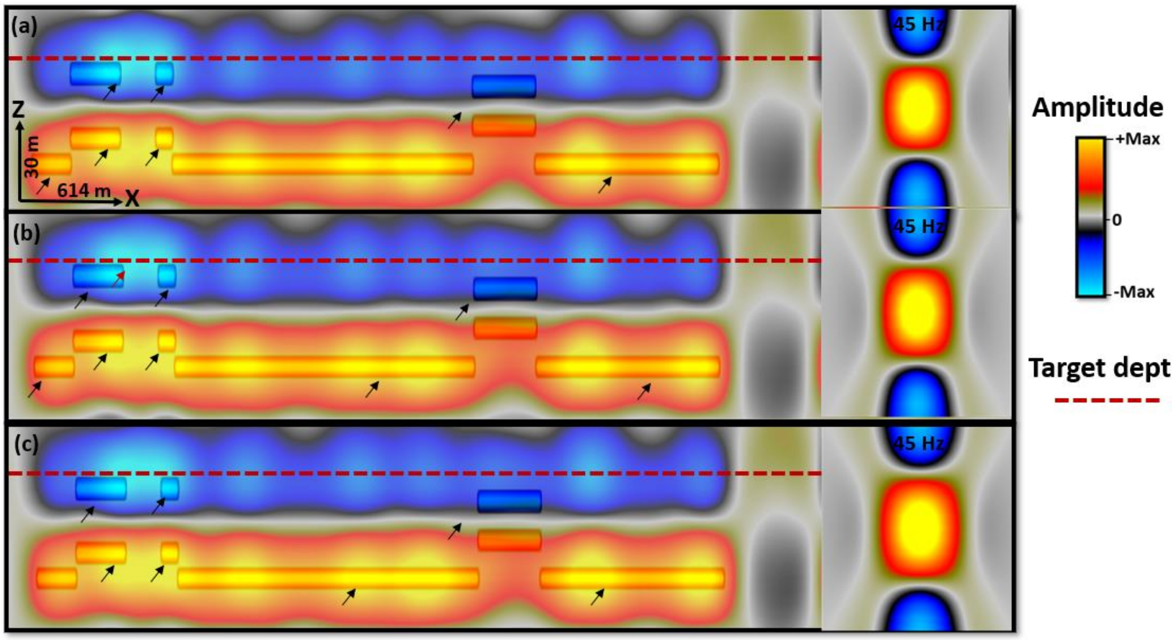

***Figure 3.3-11**: Vertical sections (at y=50 m) displaying superimposed plots of synthetic seismic and reflectivity at the top of the simple paleokarst reservoir at (a) incident angle = 0◦ (b) incident angle = 10◦ (c) incident angle = 30◦. The PSF is displayed on the extreme right-side corner of the individual seismic sections. The black arrows show regions with non-zero reflectivity. Smearing of the seismic is also visible at the top and bottom reflectors when the angle of incidence=30◦.*

To extend the validation of the seismic target, a series of zero offset (incident angle=0◦) horizontal overlays of synthetic seismic models and reflectivity model are taken at 1508 m (target depth) , 1516 m (1 m after the cave centre), and 1524 m (bottom of the largest cave passage) to compare variations in reflectivity with depth. Based on observation from Figure 3.3-12, regions with non-zero reflectivity coincides with both the top of the caves, and the bottom of the cave caves. The seismic coincides with zero amplitude while the top and bottom of the caves do not necessarily coincide with both the high negative and the positive peaks of seismic amplitudes (Figure 3.3-12).

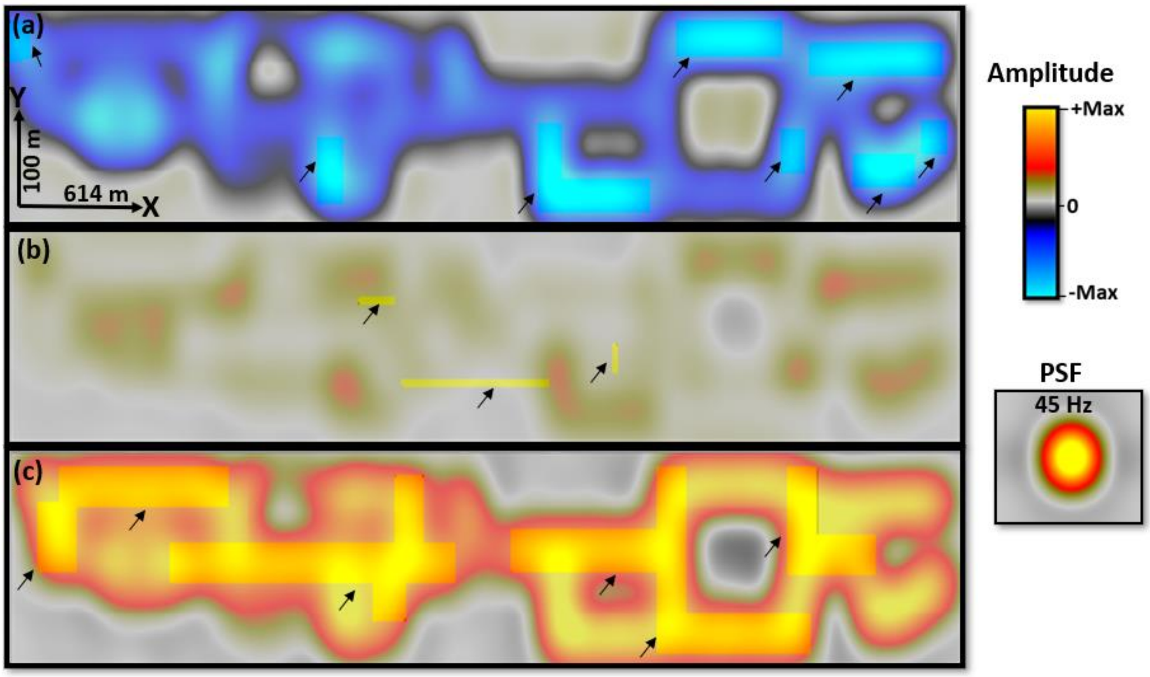

Figure 3.3-12*: An XY plane display of dual plots of synthetic seismic and reflectivity models at (a) z=1508 m (b) z=1516 m, and (c) z=1524 m. The black arrows indicate areas with reflectivity. The amplitude range, and the PSF displayed on the extreme right side apply for all the results.*

3.3 4 4D Seismic as a function of depth

4D seismic in this thesis is based on integration of seismic domain from seismic modelling, rock properties from rock physics models (static properties) and dynamic changes in the reservoir adopted from the flow simulation model aimed at monitoring the response of paleokarst reservoir to changes in pressure and injected fluid saturation during production. The bulk modulus of the rock and the fluid, fluid composition, and density may be affected when dynamic properties (pressure and saturation) change during production or through water injection resulting into seismic anomalies. Seismic anomalies are caused by changes in elastic impedance. Water injection and production are both tuned at a steady rate of 18,250 m^3/year for a period of 46.5 years. The water is injected across the entire width of the central payzone at a subsurface depth of 1515 m using horizontal injector well while the producer (horizontal well) is located 614 m away. Three production time steps at 0, 11 and 46.5 years are considered. An integration of results taken at the bottom of the reservoir (1524 m) from seismic modelling and production are used to flag regions with notable 4D seismic anomalies by looking at changes with significant in pressure and saturation. In a scenario where water saturation changes during production are considered, the 4D anomalies are highly dependent on water injection period (Figure 3.3-13): (a) before the start of water injection, the water saturation is at the lowest (base case), an equivalent of water trapped in the rock pores ($S_w \leq 0.2$). This implies no change in dynamic properties of the reservoir, (b) after 11 years of water injection, the water saturation starts to increase gradually corresponding to mostly a low increase in seismic amplitude (<10%) with exception of one region near the producer with more than 10% change in seismic amplitude, and lastly (c) the end of the water injection phase implies that the reservoir is flooded with high volume of water resulting into high saturation ($S_w \leq 0.8$) in most porous zones which in turn corresponds to a highest change in seismic amplitude as compared to (b), and the base case in (a). The changes in the seismic amplitude as a function of water saturation during production thus give 4D seismic anomalies. These anomalies are quantified as low in the case where the amplitude change is lower than 10% and as higher where the amplitude change is greater than 10%. The areas with the high 4D anomalies reflect reservoir zones with the highest rates of production, and vice versa.

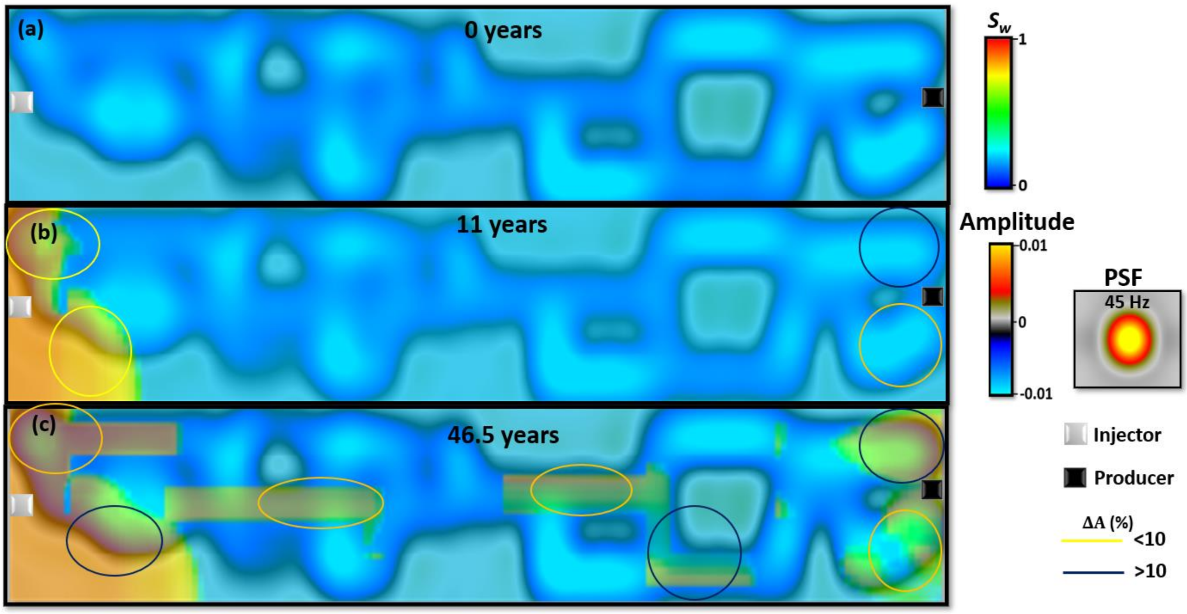

***Figure 3.3-13**: An XY plane (at z=1508 m) of superimposed plots of synthetic seismic and water saturation at the top of the simple generic paleokarst reservoir showing time-lapse anomalies (a) At base year (b) after 11 years (c) after 46.5 years. The blue oval shapes indicate regions with high 4D seismic anomalies while the yellow circles indicate regions of low seismic anomalies.*

A quantification procedure like that used in Figure 3.3-13 is adopted for changes in seismic amplitude due to change in reservoir pressure (Figure 3.3-14). Before the onset of injection, the pressure is at maximum and is equal to the initial reservoir pressure. The reservoir pressure is constant and thus no observe change in seismic amplitude (a). After 11 years of production, the pressure field increase in the vicinity of the injector well because of the advancing waterflood and is low at end with the producer well (b). This creates a pressure gradient (change in pressure with length). The change in pressure corresponds to an increase in seismic amplitude. At the end of the water injection period, more pronounced increase in pressure change occurs resulting into amplitude change relative to the base case (c).

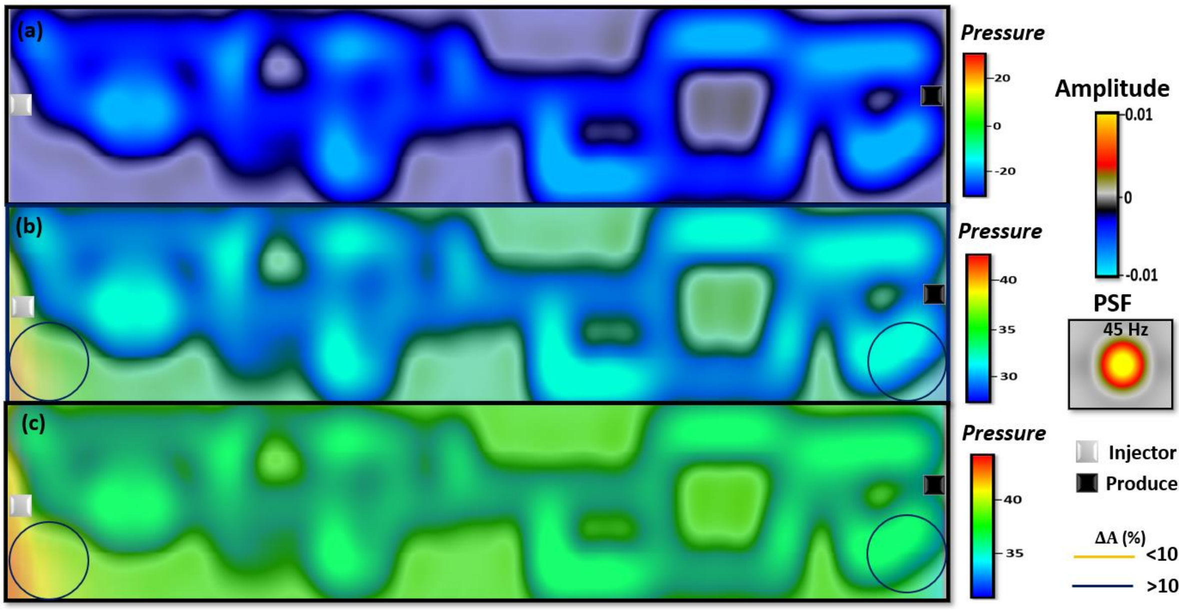

***Figure 3.3-14**: An XY plane (x=614 m, y=100 m) of superimposed plots of synthetic seismic and pore pressure at the bottom of the simple generic paleokarst reservoir model (1524) showing time-lapse anomalies (a) At base year (b) after 11 years (c) after 46.5 years. The blue oval shapes correspond to regions with high 4D seismic anomalies while the yellow circles correspond to regions of low seismic anomalies.*

.

3.4 Fracture modelling

Fracture modelling is done to study the influence of heavily fractured karst system on the flow behaviour in the main cave geometry. In a recent study, fracture swarms and orientations were found to be linked to fluid flow patterns and the development of paleokarst reservoirs (Boersma et al., 2019). There is a lot of uncertainties in predicating fracture networks and their distribution in paleokarst carbonate reservoirs. Fractures used in this study have similar directional trends as the cave network and exists in both the karst and the matrix domains of the porous media. The process for flow simulation of the fractured paleokarst carbonate reservoir is illustrated in Figure 3.4-1. The fractures are open in nature and are stochastically modelled into each layer to inherit new reservoir properties high than those of the host rock. The karsts and the background (matrix) are dominated by two major trends, namely, N-S and E-W. The N-S trend fractures are vertical fractures while the E-W trend fractures are horizontal (see Table 2.6-1 for the input parameters).

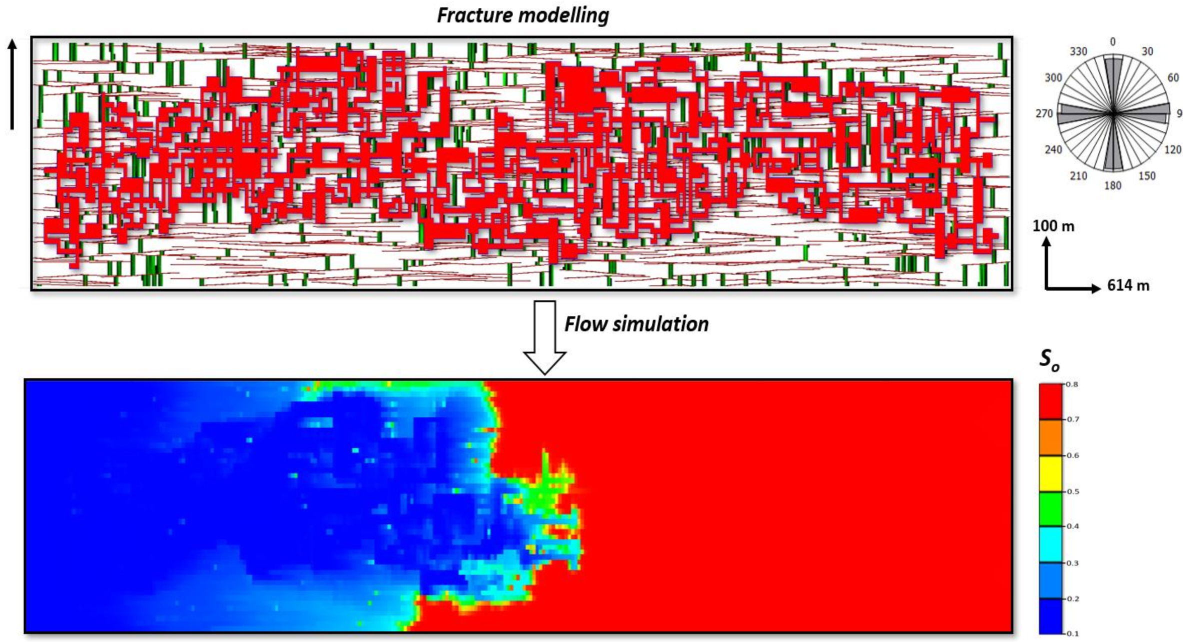

***Figure 3.4-1**: workflow for fracture modelling for generic paleokarst models.*

3.4.1 Modelling scenario 1: fracture sensitivity to fluid flow patterns in a complex karst system

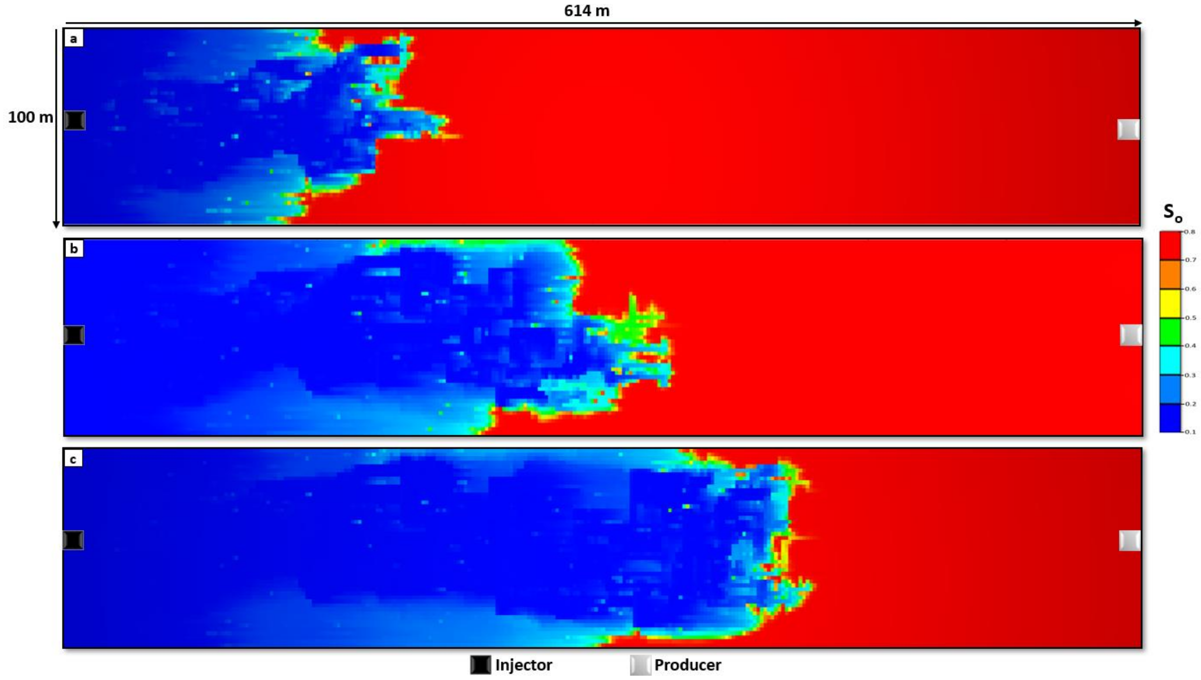

Figure 3.4-2*: Flow pattern in a horizontal section of a fractured complex generic geometric karst model (a) after 5 years of production (b) after 10 years of production (c) after 15 years of production.*

For the model with complex karst geometry, the fracture permeability in the horizontal direction (X and Y direction) is higher than both the karst system and the host rock. Fractures can meet but they cannot intersect. The permeability of the fractures in the z-direction is the same as that of the host rocks because of a software inability to independently model vertical fracture permeability tensor. This may compromise flow in the vertical direction. However, the wells are designed to inject and produce fluids in horizontal direction thus the influence of the vertical fracture permeability to flow patterns is very minimal. The total fracture porosity and fracture permeability is obtained by adding the respective host rock porosities and permeabilities to the individual fracture permeability obtained using dual-porosity method. For a fracture intersecting both the karst and the host rock, the section intersecting the karst has a higher permeability (conductivity) than the section intersecting the host rock.

Studies regarding flow pattern sensitivity to fractures in the karst model are done in three production scenarios, at 5,10 and 15 years of oil production (Figure 3.4-2 (a-c). Horizontal wells are used to increase areal sweep from the central layer at which the reservoir is symmetrical to the rest of the cave system and the host rock. The injector is tuned to continuously increase bottom hole pressure to counter reservoir pressure surges originating from water breakthrough. The oil saturation plot in Figure 3.4-2 (a) shows that the overall flow pattern flows the cave pattern with less channelling into the fractures. This is because the cave and the host rock are heavily fractured causing channelling and spreading of the displacing waterfront into the highly conductive fractures. Also, the fractures are not fully saturated with the incoming waterflood, there by more preference to the karst system. The host rock in the grid cells that are left unswept by the waterflood consist of low permeability matrix and are not intersected by fractures. As the waterfront advances, the fractures become more imbibed with the waterflood causing much diversion from the karst system. The injected water spreads more into the fractures, the flow pattern appears to slightly sweep the reservoir uniformly (Figure 3.4-2(b). The fractures in the background (matrix) exhibit slightly slower flow rates because of the low permeability with respect to the fractures in the karst system. At 5 years of waterflooding, the water moves to nearly half of the reservoir payzone as slightly faster rate invading both the cave, matrix, and the fractures. The fast waterflood movement is due to the presence of many small interconnected networks and fractures. After 5 years, the flow pattern becomes more uniform as observed in Figure 3.4-2 (c). Sweep uniformity in the later stage of production is due to an establishment of favourable path with low resistance to flow in the karsts, fractures and the matrix. From all the Figures, flow pattern is mainly enhanced in the horizontal direction indicating the presence of high permeability fractures in the east-west direction.

3.4.2 Modelling scenario 2: fracture sensitivity to fluid flow patterns in a complex karst system

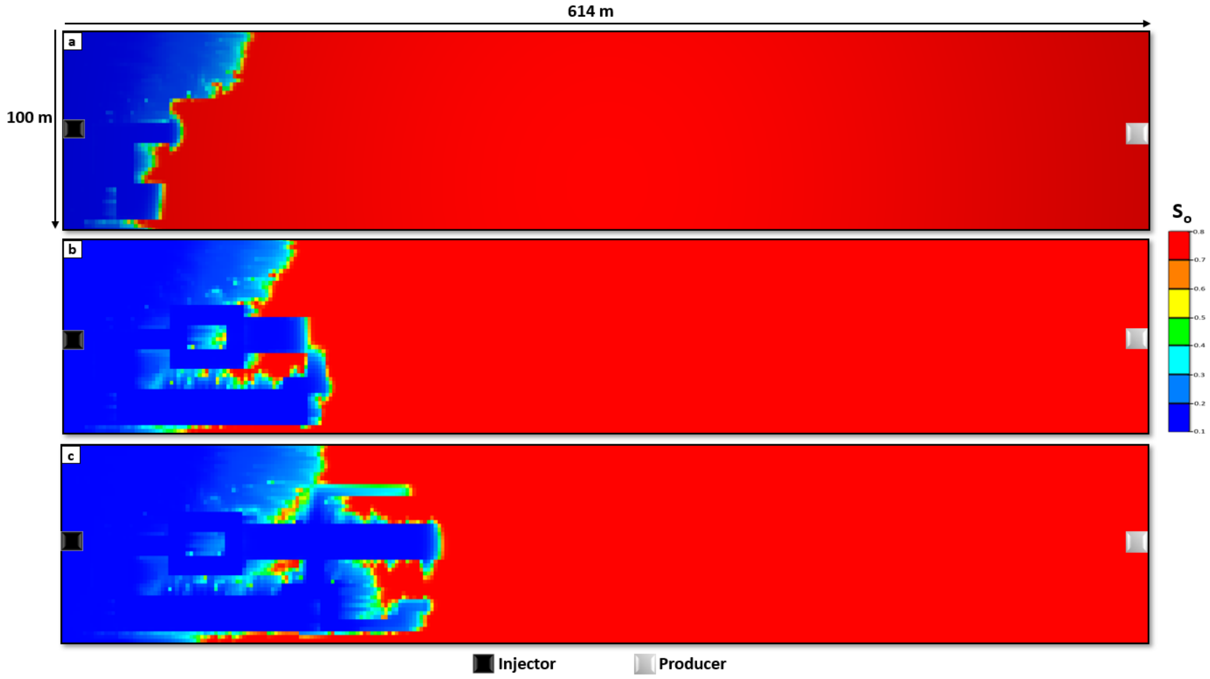

***Figure 3.4-3**: Flow pattern in a horizontal section of a fractured simple generic paleokarst model. (a) after 5 years of production (b) after 10 years of production (c) after 15 years of production.*

For the model with simple karst geometry, the fracture model used is identical to that implemented with the complex geometric karst in Figure 3.4-2. However, the cave geometry is simple with less branching, distant conduits, bigger diameter and very few small passages. For the flow simulation, production scenarios are taken in three steps of 5 years to match the scenario with a complex karst system. Firstly, at five years, the flow pattern is observed to prefer the cave geometry with less flux into the fractures, Figure 3.4-3(a). The fluids flow slower than the equivalent scenario in Figure 3.4-2(a). This is because of the much bigger karst conduits resulting into a karst dominated flow in which the influence of fractures is minimal. As the waterflood advances at later stages of production, flow into the fractured matrix increases [Figure 3.4-3(b-c)]. This further disrupts the flow preference into the cave and the waterfront in both the cave and the background advances at nearly the same rate. It is also evident that the flow velocity in the simple karst model is slower than that in the complex karst (scenario 1). The slow sweep velocity in scenario 2 may attribute to better oil recovery in fractured paleokarst reservoir with larger connected karsts or vugs.

4 CONCLUSIONS

This section contains main findings, conclusions, and recommendations that are not only limited to the challenges in the oil and gas field but may as well be applicable to other fields such as karst hydrogeology, geotechnical engineering, geothermal energy, and environment hazards.

4.1 Main Conclusions

From about 20-40 mD, a threshold is reached where the flow pattern is uniform and linear. The injected waterflood flows through the entire reservoir in a piston-like displacement irrespective of the facies present and the reservoir appears as a homogeneous flow zone. The preference of fluid flow to the cave facies decreases significantly with higher non-cave facies permeability and the cave geometry can no longer be retraced at the threshold value. It should be noted that the threshold value for uniform oil sweep maybe influenced by software artifacts and thus may not exactly match real field observations.

When production and development decisions are made, contributions from non-cave facies with low permeability surrounding the highly permeable paleokarst features should not be ignored. In this study, production rates from non-cave facies with as low as 5 mD were high enough to be economical. These findings can as well be applied to geotechnical engineering fields to study the likelihood of sinkholes occurring on roads or in settlements constructed in karst formation.

During production, wells that are positioned in the cave facies or closer produced at a steady rate maintaining a flow path in the cave geometry. However, in cases where the wells are positioned the non-cave facies or at greater distance from the cave, poor production were encountered as the reservoir pressure reduced to a possible minimum.

Better production rates are observed in karsts with less homogeneous and more permeable sediment infill. The results are valid for generic reservoir models and are yet to be extended to real field models.

The presence of fractures may cause pronounced fluid flow diversion from the cave facies into the fracture aperture or into the non-cave facies connected by the same fracture. The extent of the diversion is dependent on the fracture permeability relative to that of the host rock. The diversion of the flow path into the fractures will only happen if the fracture permeability is high than that of the cave facies it cuts through.

Better production rates are observed in karsts with less homogeneous and more permeable sediment infill. In the bigger cave passages, fluid flow occurs mainly in the cave infills at the bottom of the cave. However, this may be due to a software artifact that causes gravity forces to be more dominant than viscous and capillary forces. Therefore, the results from may not be valid and require use of other flow simulation techniques.

To capture flow in the smallest channels, selective upscaling should be considered so that details are preserved. In this case, the small channels in the karst domain should be embedded in the upscaled matrix without rescaling. Overall, the accuracy in upscaling deteriorates evenly with increase in grid sampling size, geometric complexity, and small sized cave conduits.

4D seismic reservoir monitoring based on saturation changes was possible but limited because of smaller cave features that below the minimal seismic resolution.

To produce a match between the coarse and the fine traditional simulation models, the number of cells containing small cave passages must be reduced and the reservoir properties manipulated by adjusting permeability or transmissibility between the matrix and the karst domain.

4.2 Recommendations for further work

This study mainly focused on study of simple geomodelling and upscaling techniques of generic paleokarst reservoirs with varying geometric complexity. To achieve more realistic results, the workflow used in the thesis should be calibrated with real field petrophysical data from paleocave cores.

Traditional upscaling methods by averaging of petrophysical properties do not fully capture paleokarst features, thus the need to adopt other methods like multiscale integration, numerical based upscaling or use of unstructured grids.

All the paleokarst models used in this thesis were constructed based on the assumption that the cave pores are connected and filled with only porous media to honor the Darcy's equation of flow, but in real paleokarst reservoirs, caves or vugs maybe partly filled and isolated as well. Therefore, numerical flow equations such as the Stokes-Brinkman's equation and the Navier-Stokes equation should be employed especially to study flow behaviour in paleocaves partly filled with sediments of varying composition or modern cave passages with open space.

The findings in this study should be tested for applicability to a wide range of fields such as monitoring water production, and exploring new drill targets in karst aquifers, and predicting the occurrence sinkholes to prevent geohazards.

5 REFERENCES

Afifi, A. M. J. A. S., & Discovery. (2005). Ghawar: The anatomy of the world's largest oil field. *20026*.

Alpak, F. O., Pal, M., & Lie, K.-A. J. S. J. (2012). A multiscale adaptive local-global method for modeling flow in stratigraphically complex reservoirs. *17*(04), 1,056-051,070.

Avseth, P., Mukerji, T., Mavko, G., & Dvorkin, J. J. G. (2010). Rock-physics diagnostics of depositional texture, diagenetic alterations, and reservoir heterogeneity in high-porosity siliciclastic sediments and rocks—A review of selected models and suggested work flows. *75*(5), 75A31-75A47.

Barenblatt, G. I., Zheltov, I. P., Kochina, I. J. J. o. a. m., & mechanics. (1960). Basic concepts in the theory of seepage of homogeneous liquids in fissured rocks [strata]. *24*(5), 1286-1303.

Bathurst, R. G. C. (1975). *Recent Developments in Carbonate Sedimentology*: Elsevier.

Boersma, Q., Prabhakaran, R., Bezerra, F. H., & Bertotti, G. J. P. G. (2019). Linking natural fractures to karst cave development: a case study combining drone imagery, a natural cave network and numerical modelling. *25*(4), 454-469.

Boggs Jr, S. (2014). *Principles of sedimentology and stratigraphy*: Pearson Education.

Boyd, A., Souza, A., Carneiro, G., Machado, V., Trevizan, W., Santos, B., et al. (2015). Presalt carbonate evaluation for Santos Basin, offshore Brazil. *56*(06), 577-591.

Brinkman, H. J. F., Turbulence. (1949). A calculation of the viscous force exerted by a flowing fluid on a dense swarm of particles. *1*(1), 27.

Brinkman, H. J. P. (1947). A calculation of the viscosity and the sedimentation constant for solutions of large chain molecules taking into account the hampered flow of the solvent through these molecules. *13*, 447-448.

Burchette, T. P. J. G. S., London, Special Publications. (2012). Carbonate rocks and petroleum reservoirs: a geological perspective from the industry. *370*(1), 17-37.

Cantrell, D., Swart, P., & Hagerty, R. J. G. (2004). Genesis and characterization of dolomite, Arab-D reservoir, Ghawar field, Saudi Arabia. *9*(2), 11-36.

Chilingar, G. V., Bissell, H. J., & Wolf, K. H. (1967). Diagenesis of carbonate rocks. In *Developments in sedimentology* (Vol. 8, pp. 179-322): Elsevier.

Choquette, P. W., & James, N. P. (1987). Diagenesis# 12. Diagenesis in Limestones-3. The deep burial environment. *Geoscience Canada*, *14*(1).

Choquette, P. W., & Pray, L. C. (1970). Geologic nomenclature and classification of porosity in sedimentary carbonates. *AAPG bulletin, 54*(2), 207-250.

Correia, M., Hohendorff, J., & Schiozer, D. (2019). *Multiscale Integration for Karst Reservoir Flow Simulation Models*. Paper presented at the SPE Europec featured at 81st EAGE Conference and Exhibition, London, England, UK. https://doi.org/10.2118/195545-MS

Correia, M. G., Maschio, C., Schiozer, D. J. J. o. t. B. S. o. M. S., & Engineering. (2017). Development of complex layered and fractured reservoir models for reservoir simulation. *39*(1), 219-233.

Daniel, E. J. A. B. (1954). Fractured reservoirs of middle east. *38*(5), 774-815.

Darcy, H. P. G. (1856). *Les Fontaines publiques de la ville de Dijon. Exposition et application des principes à suivre et des formules à employer dans les questions de distribution d'eau, etc*: V. Dalamont.

Dembicki, E. A., & Machel, H. G. J. A. b. (1996). Recognition and delineation of paleokarst zones by the use of wireline logs in the bitumen-saturated Upper Devonian Grosmont Formation of northeastern Alberta, Canada. *80*(5), 695-712.

Dogru, A. H., Dreiman, W. T., Hemanthkumar, K., & Fung, L. S. (2001). *Simulation of super-k behavior in ghawar by a multi-million cell parallel simulator.* Paper presented at the SPE Middle East Oil Show.

Dunham, R. J. (1962). Classification of carbonate rocks according to depositional textures.

Embry, A. F., & Klovan, J. E. (1971). A late Devonian reef tract on northeastern Banks Island, NWT. *Bulletin of Canadian Petroleum Geology, 19*(4), 730-781.

Folk, R., & Dunham, W. J. A. P. G. M. (1962). Classification of carbonate rocks. (1), 62-84.

Folk, R. L. (1959). Practical petrographic classification of limestones. *AAPG bulletin, 43*(1), 1-38.

Folk, R. L. (1974). The natural history of crystalline calcium carbonate; effect of magnesium content and salinity. *Journal of Sedimentary Research, 44*(1), 40-53.

Fournillon, A., Bellentani, G., Moccia, A., Jumeaucourt, C., Terdich, P., Siliprandi, F., & Peruzzo, F. (2017). Characterization of a paleokarstic oil field (Rospo Mare, Italy): sedimentologic and diagenetic outcomes, and their integration in reservoir simulation. In *EuroKarst 2016, Neuchâtel* (pp. 47-55): Springer.

Frumkin, A., Zaidner, Y., Na'aman, I., Tsatskin, A., Porat, N., & Vulfson, L. (2015). Sagging and collapse sinkholes over hypogenic hydrothermal karst in a carbonate terrain. *Geomorphology, 229*, 45-57.

Furnée, J. P. B. (2015). *Geo-modeling and fluid flow simulation in paleokarst reservoirs.* The University of Bergen,

Gaffney, C. J. R. d. J. A. N. d. P., Gas Natural e Biocombustiveis-ANP. (2010). Review and evaluation of ten selected discoveries and prospects in the pre-salt play of the deepwater Santos Basin, Brazil.

Galdi, G. (2011). *An introduction to the mathematical theory of the Navier-Stokes equations: Steady-state problems*: Springer Science & Business Media.

Gao, S., Killough, J. E., He, J., Fadlelmula, M. M., Wang, F. Y., & Fraim, M. L. (2017). *A new approach for the simulation of fractured vuggy carbonate reservoir with an application to upscaling.* Paper presented at the SPE Reservoir Characterisation and Simulation Conference and Exhibition.

Gassmann, F. J. V. d. N. G. i. Z. (1951). Uber die elastizitat poroser medien. *96*, 1-23.

Gulbransen, A. F., Hauge, V. L., & Lie, K.-A. J. S. J. (2010). A multiscale mixed finite element method for vuggy and naturally fractured reservoirs. *15*(02), 395-403.

Haldorsen, H. H., & Damsleth, E. J. A. b. (1993). Challenges in reservoir characterization: Geohorizons. *77*(4), 541-551.

Hammes, U., Lucia, F., & Kerans, C. J. P.-W. T. G. S. (1996). Reservoir heterogeneity in karst-related reservoirs: Lower Ordovician Ellenburger Group, west Texas. 99-116.

Hanshaw, B. B., & Back, W. (1979). Major geochemical processes in the evolution of carbonate-aquifer systems. In *Developments in Water Science* (Vol. 12, pp. 287-312): Elsevier.

Hardie, L. A. (1984). Evaporites; marine or non-marine? *American Journal of Science, 284*(3), 193-240.

Hashin, Z., Shtrikman, S. J. J. o. t. M., & Solids, P. o. (1963). A variational approach to the theory of the elastic behaviour of multiphase materials. *11*(2), 127-140.

Henrion, V., Pellerin, J., & Caumon, G. (2008). *A stochastic methodology for 3D cave systems modeling.*

Hill, R. J. P. o. t. P. S. S. A. (1952). The elastic behaviour of a crystalline aggregate. *65*(5), 349.

Horn, G. (1947). *Karsthuler i Nordland* (Vol. 165): Aschehoug i komm.

Hróarsson, B., & Jónsson, S. S. (1991). *Lava Caves in the Hallmundarhraun Lava Flow, Western Iceland.* Paper presented at the Proceedings of the 6 th International Symposium on Vulcanospeleology.

Jennings Jr, J. W., & Lucia, F. J. (2001). *Predicting permeability from well logs in carbonates with a link to geology for interwell permeability mapping.* Paper presented at the SPE Annual Technical Conference and Exhibition.

Johansen, M. K. (2018). *A modelling workflow for seismic characterization of paleokarst reservoirs.* The University of Bergen,

Kerans, C. J. A. b. (1988). Karst-controlled reservoir heterogeneity in Ellenburger Group carbonates of west Texas. *72*(10), 1160-1183.

Kippe, V., Aarnes, J. E., & Lie, K.-A. J. C. G. (2008). A comparison of multiscale methods for elliptic problems in porous media flow. *12*(3), 377-398.

Klimchouk, A. (1996). The typology of gypsum karst according to its geological and geomorphological evolution. *International Journal of Speleology, 25*(3), 4.

Laptev, V. (2003). Numerical solution of coupled flow in plain and porous media.

Lauritzen, S.-E., Baastad, L., & Engelien, J. (2018). Ice Caves in Norway, Fennoscandia and the Arctic. In *Ice Caves* (pp. 479-492): Elsevier.

Lecomte, I., Gjøystdal, H., & Drottning, Å. (2003). *Simulated Prestack Local Imaging: a robust and efficient interpretation tool to control illumination, resolution, and time-lapse properties of reservoirs.* Paper presented at the 2003 SEG Annual Meeting.

Lecomte, I., Lavadera, P. L., Anell, I., Buckley, S. J., Schmid, D. W., & Heeremans, M. J. I. (2015). Ray-based seismic modeling of geologic models: Understanding and analyzing seismic images efficiently. *3*(4), SAC71-SAC89.

Lecomte, I., Lavadera, P. L., Botter, C., Anell, I., Buckley, S. J., Eide, C. H., et al. (2016). 2 (3) D convolution modelling of complex geological targets beyond–1D convolution. *First Break, 34*(5).

Ledsaak, K. (2016). *Geo-modelling of paleokarst reservoirs-from cave-survey to geocellular paleokarst model.* The University of Bergen,

Li, J.-y., Jiang, H.-q., Li, J.-j., Chen, M.-f., Tu, X.-w., & REN, W.-b. J. I. M. P. I. (2008). The feasibility study for fractured and cavernous carbonate reservoir by injecting nitrogen [J]. *23*.

Li, J., Zhang, W., Luo, X., & Hu, G. (2008). Paleokarst reservoirs and gas accumulation in the Jingbian field, Ordos Basin. *Marine and Petroleum Geology, 25*(4-5), 401-415.

Li, J. y., Jiang, H.-q., Li, J.-j., Chen, M.-f., Tu, X.-w., & REN, W.-b. J. I. M. P. I. (2008). The feasibility study for fractured and cavernous carbonate reservoir by injecting nitrogen [J]. *23*.

Lønøy, A. (2006). Making sense of carbonate pore systems. *AAPG bulletin, 90*(9), 1381-1405.

Lønøy, B., Pennos, C., Tveranger, J., Fikos, I., Vargemezis, G., & Jensen, S. E. L. K. (2019). Sediment accumulations in paleokarst reservoirs-Analogues from an active cave system.

Loucks, R., & Anderson, J. (1980). Depositional facies and porosity development in Lower Ordovician Ellenburger dolomite, Puckett field, Pecos County, Texas.

Loucks, R. G. (1999). Paleocave carbonate reservoirs: origins, burial-depth modifications, spatial complexity, and reservoir implications. *AAPG bulletin, 83*(11), 1795-1834.

Loucks, R. G., & Handford, C. R. J. P.-W. T. G. S. (1996). Origin and recognition of fractures, breccias and sediment fills in paleocave-reservoir networks. 207-220.

Lucia, F. J. (2007). *Carbonate reservoir characterization: An integrated approach*: Springer Science & Business Media.

Målbakken, T. (2009). Paleo Caves and collapse breccias in the Franklin Mountains; implications for paleokarst reservoirs. Master's thesis, University of Bergen, Department of Earth Science, 147 pp.

Mavko, G., Mukerji, T., & Dvorkin, J. (2009). *The rock physics handbook*: Cambridge university press.

Mazzullo, S., & Chilingarian, G. (1996). Hydrocarbon reservoirs in karsted carbonate rocks. In *Developments in Petroleum Science* (Vol. 44, pp. 797-865): Elsevier.

Mescher, P. K., Schultz, D. J., Hendrick, S., Ward, M., & Schwarz, J. (1993). *Lithology and reservoir development of the Arbuckle dolomite, Wilburton field, Latimer County, Oklahoma.* Paper presented at the Petroleum-reservoir geology in the southern midcontinent, 1991 Symposium: Oklahoma Geological Survey Circular.

Moinfar, A. (2013). Development of an efficient embedded discrete fracture model for 3D compositional reservoir simulation in fractured reservoirs.

Moore, C. (2001). Developments in Sedimentology 55: Carbonate Reservoirs—Porosity Evolution and Diagenesis in a Sequence Stratigraphic Framework. In: Elsevier.

Moore, C. H. (1989). *Carbonate diagenesis and porosity*: Elsevier.

Noetinger, B., Zargar, G. J. O., Science, G., & Technology. (2004). Multiscale description and upscaling of fluid flow in subsurface reservoirs. *59*(2), 119-139.

Nordeide, H. C. (2008). *Spatial distribution and architecture of breccia pipes features at Wordiekammen, Billefjorden, Svalbard.* Master Thesis, Department of Earth Science, University of Bergen,

Nordli, C. J. P. R., Master Thesis, Department of Physics. (2009). Fluid Flow in and around collapsed karst structures; breccia pipes. *Petroleum Reservoirs, Master Thesis, Department of Physics*

Technology/Department of Earth Science, University of Bergen

Palmer, A. N. J. G. S. o. A. B. (1991). Origin and morphology of limestone caves. *103*(1), 1-21.

Pantou, I. (2014). Impact of Stratigraphic Heterogeneity on Hydrocarbon Recovery in Carbonate Reservoirs: Effect of Karst.

Pappas, D. M., & Mark, C. (1993). Behavior of simulated longwall gob material.

Peaceman, D. J. D. i. P. S. (1977). Fundamentals of Numerical Simulation. *6*.

Popov, P., Qin, G., Bi, L., Efendiev, Y., Ewing, R. E., Li, J. J. S. R. E., & Engineering. (2009). Multiphysics and multiscale methods for modeling fluid flow through naturally fractured carbonate karst reservoirs. *12*(02), 218-231.

Riding, R. J. E.-S. R. (2002). Structure and composition of organic reefs and carbonate mud mounds: concepts and categories. *58*(1-2), 163-231.

Ringrose, P., & Bentley, M. (2015). The property model. In *Reservoir Model Design* (pp. 61-113): Springer.

Roxar. (2018). RMS 11.0. 1 User Guide. Roxar Software Solutions. In.

Sangster, D., & Hillary, E. (1998). Sedex lead-zinc deposits; proposed sub-types and their characteristics. *Exploration and Mining Geology, 7*(4), 341-357.

Schmoker, J. W., & Halley, R. B. (1982). Carbonate porosity versus depth: a predictable relation for south Florida. *AAPG bulletin, 66*(12), 2561-2570.

Scholle, P. A., Bebout, D. G., & Moore, C. H. (1983). *Carbonate depositional environments: AAPG Memoir 33*: AAPG.

Skoglund, R. O., Lauritzen, S.-E. J. J. o. C., & Studies, K. (2011). Subglacial maze origin in low-dip marble stripe karst: examples from Norway. *73*(1), 31-43.

Smart, P. L., Palmer, R., Whitaker, F., & Wright, V. P. (1988). Neptunian Dikes and Fissure Fills: An Overview and. In *Paleokarst* (pp. 149-162): Springer.

Stewart, F. H. (1963). *Marine evaporites*: US Government Printing Office.

Tinker, S., & Mruk, D. (1995). Hydrocarbon reservoir characterization, geologic framework and flow-unit modeling.

Trice, R. (2005). *Challenges And Insights In Optimising Oil Production Form Middle Eastern Karst Reservoirs.* Paper presented at the SPE Middle East Oil and Gas Show and Conference.

Uba, M. H., Chiffoleau, Y., Pham, T. R., Divry, V. E., Al-Kaabi, A. U., & Thuwaini, J. (2007). *Application of a hybrid dual porosity dual permeability representation of large scale fractures to the simulation of a giant carbonate reservoir.* Paper presented at the SPE Middle East Oil and Gas Show and Conference.

Voelker, J., & Caers, J. (2004). *A reservoir characterization of Arab-D Super-K as a discrete fracture network flow system, Ghawar Field, Saudi Arabia.* Stanford University,

Waltham, A., & Fookes, P. (2005). Engineering classification of karst ground conditions. QJ Eng. Geol. *Hydrogéologie, 3*(1), 1-20.

Wang, D., & Sun, J. J. S. r. (2019). Oil recovery for fractured-vuggy carbonate reservoirs by cyclic water huff and puff: performance analysis and prediction. *9*.

Warren, J., & Price, H. J. S. o. P. E. J. (1961). Flow in heterogeneous porous media. *1*(03), 153-169.

Wright, V., Esteban, M., & Smart, P. J. P. C. (1991). Paleokarst and Paleokarstic Reservoirs: University of Reading. *152*, 157.

Zhang, K. J. O. G. G. (1999). The discovery of Tahe oilfield and its geologic implication. *20*(2), 120-132.

Zhao, W., Shen, A., Qiao, Z., Zheng, J., & Wang, X. J. I. (2014). Carbonate karst reservoirs of the Tarim Basin, northwest China: Types, features, origins, and implications for hydrocarbon exploration. *2*(3), SF65-SF90.

Zheng, S., Li, Y., & Zhang, H. J. J. o. C. U. o. P. E. o. N. S. (2010). Fracture-cavity network model for fracture cavity carbonate reservoir. *34*(3), 72-75.

6 APPENDICES

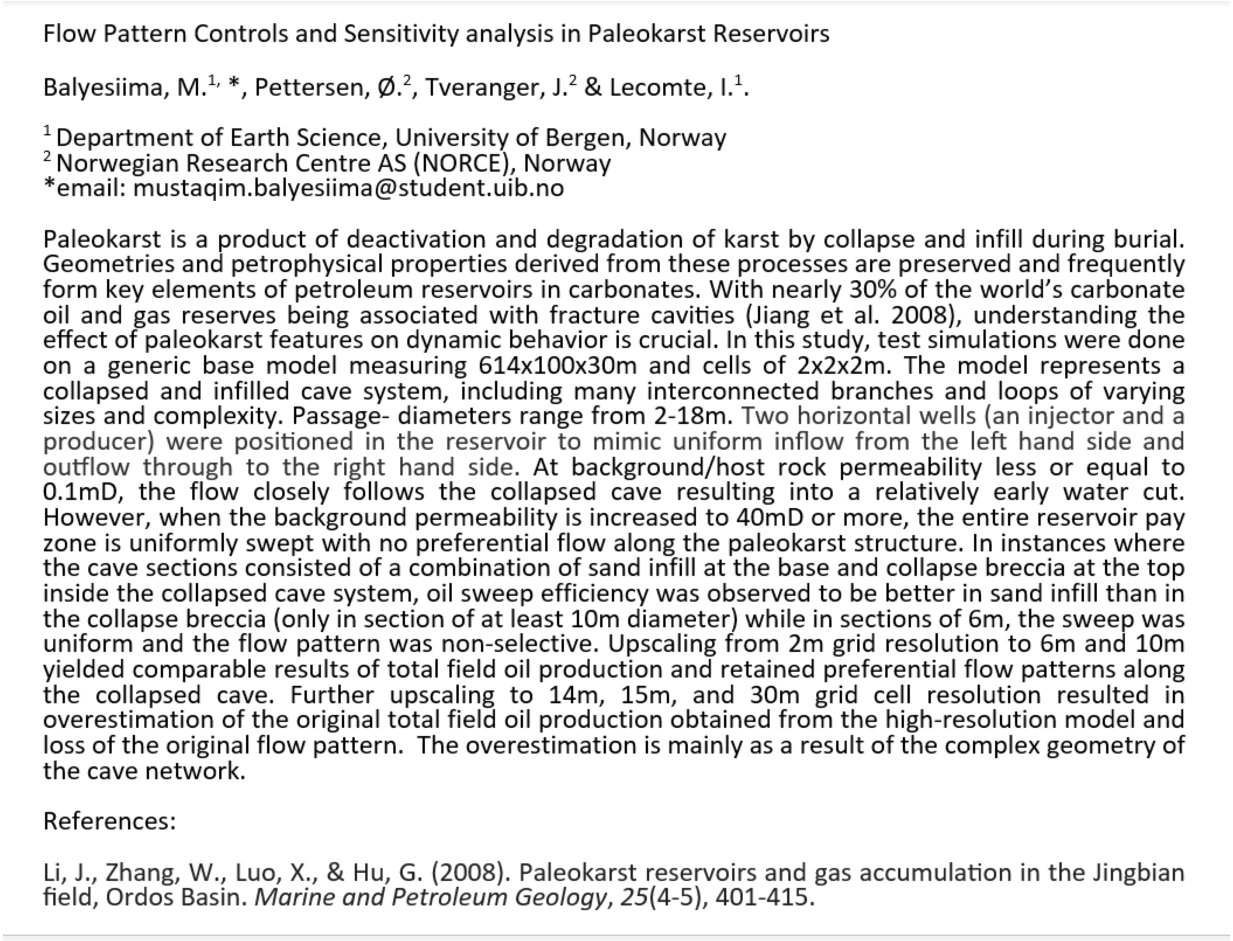

Flow Pattern Controls and Sensitivity analysis in Paleokarst Reservoirs

Balyesiima, M.[1,] *, Pettersen, Ø.[2], Tveranger, J.[2] & Lecomte, I.[1].

[1] Department of Earth Science, University of Bergen, Norway
[2] Norwegian Research Centre AS (NORCE), Norway
*email: mustaqim.balyesiima@student.uib.no

Paleokarst is a product of deactivation and degradation of karst by collapse and infill during burial. Geometries and petrophysical properties derived from these processes are preserved and frequently form key elements of petroleum reservoirs in carbonates. With nearly 30% of the world's carbonate oil and gas reserves being associated with fracture cavities (Jiang et al. 2008), understanding the effect of paleokarst features on dynamic behavior is crucial. In this study, test simulations were done on a generic base model measuring 614x100x30m and cells of 2x2x2m. The model represents a collapsed and infilled cave system, including many interconnected branches and loops of varying sizes and complexity. Passage- diameters range from 2-18m. Two horizontal wells (an injector and a producer) were positioned in the reservoir to mimic uniform inflow from the left hand side and outflow through to the right hand side. At background/host rock permeability less or equal to 0.1mD, the flow closely follows the collapsed cave resulting into a relatively early water cut. However, when the background permeability is increased to 40mD or more, the entire reservoir pay zone is uniformly swept with no preferential flow along the paleokarst structure. In instances where the cave sections consisted of a combination of sand infill at the base and collapse breccia at the top inside the collapsed cave system, oil sweep efficiency was observed to be better in sand infill than in the collapse breccia (only in section of at least 10m diameter) while in sections of 6m, the sweep was uniform and the flow pattern was non-selective. Upscaling from 2m grid resolution to 6m and 10m yielded comparable results of total field oil production and retained preferential flow patterns along the collapsed cave. Further upscaling to 14m, 15m, and 30m grid cell resolution resulted in overestimation of the original total field oil production obtained from the high-resolution model and loss of the original flow pattern. The overestimation is mainly as a result of the complex geometry of the cave network.

References:

Li, J., Zhang, W., Luo, X., & Hu, G. (2008). Paleokarst reservoirs and gas accumulation in the Jingbian field, Ordos Basin. *Marine and Petroleum Geology*, *25*(4-5), 401-415.

Appendix 1: A screenshot of an abstract accepted for poster presentation at the 2020 Nordic Geological Forum Winter Meeting in Oslo.

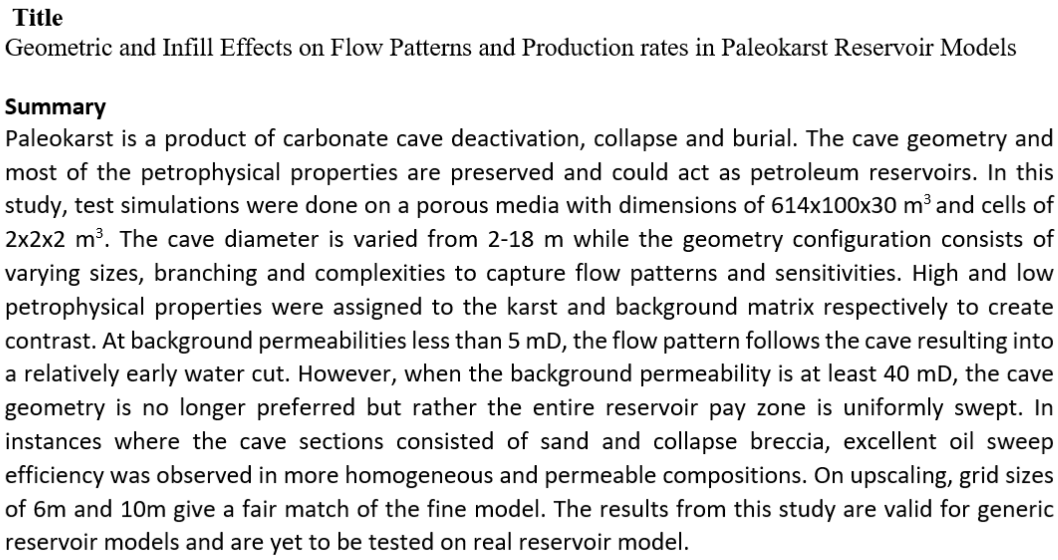

Title

Geometric and Infill Effects on Flow Patterns and Production rates in Paleokarst Reservoir Models

Summary

Paleokarst is a product of carbonate cave deactivation, collapse and burial. The cave geometry and most of the petrophysical properties are preserved and could act as petroleum reservoirs. In this study, test simulations were done on a porous media with dimensions of 614x100x30 m^3 and cells of 2x2x2 m^3. The cave diameter is varied from 2-18 m while the geometry configuration consists of varying sizes, branching and complexities to capture flow patterns and sensitivities. High and low petrophysical properties were assigned to the karst and background matrix respectively to create contrast. At background permeabilities less than 5 mD, the flow pattern follows the cave resulting into a relatively early water cut. However, when the background permeability is at least 40 mD, the cave geometry is no longer preferred but rather the entire reservoir pay zone is uniformly swept. In instances where the cave sections consisted of sand and collapse breccia, excellent oil sweep efficiency was observed in more homogeneous and permeable compositions. On upscaling, grid sizes of 6m and 10m give a fair match of the fine model. The results from this study are valid for generic reservoir models and are yet to be tested on real reservoir model.

Appendix 2: A screenshot of a summary from an extended abstract for oral presentation in a reservoir simulation session at the 82nd EAGE conference and exhibition (due from 8-11 December 2020).

Appendix 3: Main eclipse data file used for paleokarst flow simulation.

```
---------------------------------------------------------------------------------------------------------
RUNSPEC
TITLE
GENERIC BASE MODEL


--Reservoir Grid
-- ------------------------------------------------------------------------------------------------------
DIMENS
307   50   15/


--UNIT SYSTEM
-- -------------------------------------------------------------------------------------------------------
-------
METRIC    -- The metric system is the most widely used unit system in the oil and gas industry.
-- -------------------------------------------------------------------------------------------------------
-------
--PHASES AND COMPONENTS
OIL
WATER
-- The oil phase fills up the reservoir while the water is injected to aid recovery.
-- -------------------------------------------------------------------------------------------------------
---
```

```
--Linear Solver stack size is set to be equal to the LITMAX specified under the tuning parameter section.

NSTACK

58/

--I Increased N stack from the default to fit the LITMAX of the most stable run.

--Note: Increasing the NSTACK after 60 does not increase simulation runs.

------------------------------------------------------------------------------------------------------------------------

-- Number of iterations to update well targets

NUPCOL

10/

--The value was increased from the default (3) to avoid Linear Convergence Failure and severities.

-- -----------------------------------------------------------------------------------------------------------------------

-- Table dimensions

-- The data consists of some or all the following items which describe the sizes of saturation and PVT

tables used in the run, and the number of fluid-in-place regions

TABDIMS

--NTSFUN NTPVT NSSFUN NPPVT NTFIP NRPVT NTENDP

1      1      20     20     2      20 /

--specifies the number of tables used in the Data file.
```

```
--Specifies messages to be printed by the simulator during the simulation run

-- ----------------------------------------------------------------------------------------------------------------------------

MESSAGES

3* 1000 2* 3* 100000 /

--sets the print limit to 1000 and the stop limit for 100000 problems




-- Region dimensions

-- ---------------------------------------------------------------------------------------------------------------

REGDIMS

-- ntfip   nmfipr   nrfreg    ntfreg

2    2/

-- A value of 2 defines both the default reservoir regions and user defined regions of interest.

-- Well dimensions

-- ----------------------------------------------------------------------------------------------------------------

WELLDIMS

--Max#Wells MaxConn/well MaxGrp MaxWell/Grp BS

2          50          1       2 /

-- 2 well heads with 50 connections to represent horizontal wells. Each well horizontally penetrates 25 cells.
```

```
--Grid options

GRIDOPTS

--Alternative Multipliers        NRMULT     NRPINC

NO   2   0 /

-- Specified as 'NO' and assigned a value of 2 because Multipliers where used.

-- ------------------------------------------------------------------------------------------------------------
---

-- Data checking and quick runs only

--NOSIM

--Constrained Pressure Residue

CPR

/

-Linear solver activated to increase run efficiency to about 95% efficiency.

--Recommended for a karst model with a very complex geometry.

-- However, for the simple geometric model, the default linear solver can still be used without
difficulty.



--Output Option

-- ------------------------------------------------------------------------------------------------------------
----------

UNIFOUT

-- Specifies the output options for the time step data files. The format is a UNRST file that can
be exported to a seismic modelling software.

--Simulation start date
```

```
START
1 JAN 2019 /
-- -----------------------------------------------------------------------------------------------------------------------
GRID
NOECHO
-- switches echo output off
-- used to reduce the amount of print out from a run
-- and to avoid output of the large 'INCLUDE' files.
---------------------------------------------------------------------------------------------------------------
-- X-direction grid block sizes
DX
15000*2
15000*2
15000*2
15000*2
15000*2
15000*2
15000*2
15000*2
15000*2
15000*2
15000*2
```

```
15000*2
15000*2
15000*2
15000*2
5250*2/

-- Y-direction grid block sizes
DY
15000*2
15000*2
15000*2
15000*2
15000*2
15000*2
15000*2
15000*2
15000*2
15000*2
15000*2
15000*2
15000*2
15000*2
```

```
15000*2
5250*2/


-- Z-direction grid block sizes
DZ
15000*2
15000*2
15000*2
15000*2
15000*2
15000*2
15000*2
15000*2
15000*2
15000*2
15000*2
15000*2
15000*2
15000*2
15000*2
5250*2/
--Depth of the top face of each grid block
```

```
TOPS
15350*1500
15350*1502
15350*1504
15350*1506
15350*1508
15350*1510
15350*1512
15350*1514
15350*1516
15350*1518
15350*1520
15350*1522
15350*1524
15350*1526
15350*1528/
--The topmost layer is at 1500 m
--layer 8 has a depth of 1514m, which is also what I used in the EQUIL section.
-- The bottom most is at 1530 m
-- ------------------------------------------------------------------------------------------------------------
----------
-- This include file contains 'MULTNUM' keyword for applying inter-region multipliers.
-- Values of 1 and 2 were used to specify non-cave and cave facies respectively.
```

```
INCLUDE
'D:\MAIN\simple_model\simplest_model\regions_section_multnum.DATA'/
-- path to the MULTNUM Data file used to specify the entire reservoir regions.
-- ------------------------------------------------------------------------------------------------------------------------
-- BOX was used to define the petrophysical properties
--This is done in steps by combining the BOX keyword and the 'MULTIREG' keyword
-- Initially the entire reservoir is defined as matrix only
-- then using the MULTIREG keyword, the karst domain (2)
--is created by multiplying the matrix PORO OR PERM by a factor.
BOX
1 307  1 50  1 15/
PORO
230250*0.02/
-- Matrix Porosity

PERMX
230250*0.1/
-- tensor Matrix permeability in the X-direction
PERMY
230250*0.1/
-- tensor Matrix permeability in the Y-direction
PERMZ
```

```
230250*0.1/

--tensor Matrix permeability in the Z-direction

-----------------------------------------------------------------------------------------------------------------
----

-- Region Multiplier

MULTIREG

PORO   10     2/

PERMX  10000  2/

PERMY  10000  2/

PERMZ  10000  2/

/

-- MULTIREG multiplies the MULTNUM flux region by a constant factor to match
petrophysical properties.

--This populates the grid with PORO AND PERM for the karst domain

-- ----------------------------------------------------------------------------------------------------------

--Matrix Fracturing

BOX

1    2      1    50     8    8/

PERMX

100*2/

--Fracture mimic set to 20*PERMX (Non cave) and overwrites the initial matrix perm

-----------------------------------------------------------------------------------------------------------------
-----------
```

```
--Outputs all petrophysical properties

INIT

-- ---------------------------------------------------------------------------------------------------------------
----------

--Contains input data with reservoir pressure and saturation dependent properties of fluids and
rocks.

PROPS

-- ---------------------------------------------------------------------------------------------------------------
----------

ECHO

-- ---------------------------------------------------------------------------------------------------------------
----------

-- Water/oil saturation function vs water saturation

SWOF

-- Sw    krw     kro     Pc

0.20    0.000    0.850    0

0.25    0.006    0.727    0

0.30    0.013    0.613    0

0.35    0.022    0.509    0

0.40    0.032    0.414    0

0.45    0.043    0.330    0

0.50    0.057    0.255    0

0.55    0.071    0.189    0

0.60    0.087    0.133    0
```

```
0.65    0.105    0.087     0
0.70    0.124    0.051     0
0.75    0.144    0.024     0
0.80    0.167    0.007     0
0.85    0.190    0.000     0
0.9     0.215    0.000     0
1       1.000    0.000     0   /

-- PVT properties for water
PVTW
-- Pref    Bw      Cw     ViscW
308.2   1.024   4.64E-5   1*    /
--Rock properties.
ROCK
-- Pref    Cr
1.0    0.000056/
-- Fluid densities at surface conditions.
DENSITY
-- Oil    WAT   Gas
883.0   1038.0   0.660 /
-- P    Bo    viscO
-- PVT properties for dead oil.
```

```
PVDO
227.0    1.2600     1.042
253.4    1.2555     1.072
281.6    1.2507     1.096
311.1    1.2463     1.118
343.8    1.24173    1.151
373.5    1.2377      1.174
395.5    1.2356      1.2    /
-- Dead oil: oil without dissolved gas.
RSCONST
--Rs is the Bubble point
100     180.0/


SOLUTION
--Equilibrium
EQUIL
-- Datum    depth P(DD)   OWC   Pcow(OWC)  {GOC / Pcog / Nlive / RvN / Nacc.
      1514       320.0            2225              0             1400        0        0        0 /
-- I have defined the datum depth as 1514 which is the depth of the central layer (8), and the
OWC is below the bottom most layer so that the reservoir is entirely filled with oil.
RPTSOL
--specify the restart file.
RESTART=2 FIP=3/
```

```
--specifies the number of variables that
SUMMARY
-- Field Oil Production Rate:
FOPR
-- Field Oil Production Total:
FOPT
-- Field WAT Production Rate:
FWPR
-- Field WAT Injection Rate:
FWIR
-- Field WAT Cut:
FWCT
-- Field Pressure (average reservoir pressure):
FPR
-- Field Gas Prod. Rate
FGPR
-- Well WAT Cut for all wells:
WWCT
-- Well Bottom Hole Pressure for all wells:
WBHP

-- Field Oil In Place:
```

```
FOIP
-- Field Oil Efficiency: (Recovery Factor)
FOE
--Total stock tank oil produced by water influx
FORMW
--region production rate.
RPR
/
--Region oil production rate
ROPR
/
-- Region oil flux (Total)
ROFT
1 2/
2 1/
/
-- Region Water Flux (Total)
RWFT
1 2/
2 1/
/
-- Region Water Flux (Total)
```

```
RWPT
/
-- Regional Oil in place
ROIP
/
--Region Oil Efficiency
ROE
/
--total oil produced by water flux from a region
RORMW
/
-- outputs simulation data files
EXCEL
--timestep
TIMESTEP
--Number of newton iterations for each time step
NEWTON
--current CPU usage in seconds
TCPU
--CPU time per time step in seconds
TCPUDAY
--CPU time per day
```

```
TCPUDAY

--Average number of linear iterations per Newtonian iteration, for each time step

NLINEARS/

-- specifies the operations to be simulates (production and injection controls and constraints)

SCHEDULE
===================================================================

--controls the output of data to the restart file

RPTRST

--------------------------------------------------------------------------------------------------------------------------
------------

BASIC=2/

-- A value of 2 creates restart files at every report time and keeps the output.

-- specifies data for wells

WELSPECS

--wname  grp  iwh jwh Z(bhp) prefPhase rPI/II sp.Infl AutoShut X-flow Ptab densCalc FIPnr

INJ1    G  1  25  1*  WAT/

PROD1   G  307  25  1*  OIL/

/

--INJ1 is the a horizontal injector and the PROD1 is a horizontal producer

--------------------------------------------------------------------------------------------------------------------------
---------------------------

--Well completion specification data
```

```
COMPDAT

--wname ic jc k1 k2 open? satnum tfac wdiam  Kh skin Dfac penDir r0

INJ1  1  1  8  8  OPEN  1*  1*  0.31  1*  0  0  Y   /

INJ1  1  2  8  8  OPEN  1*  1*  0.31  1*  0  0  Y   /

INJ1  1  3  8  8  OPEN  1*  1*  0.31  1*  0  0  Y   /

INJ1  1  4  8  8  OPEN  1*  1*  0.31  1*  0  0  Y   /

INJ1  1  5  8  8  OPEN  1*  1*  0.31  1*  0  0  Y   /

INJ1  1  6  8  8  OPEN  1*  1*  0.31  1*  0  0  Y   /

INJ1  1  7  8  8  OPEN  1*  1*  0.31  1*  0  0  Y   /

INJ1  1  8  8  8  OPEN  1*  1*  0.31  1*  0  0  Y   /

INJ1  1  9  8  8  OPEN  1*  1*  0.31  1*  0  0  Y   /

INJ1  1  10  8  8  OPEN  1*  1*  0.31  1*  0  0  Y   /

INJ1  1  11  8  8  OPEN  1*  1*  0.31  1*  0  0  Y   /

INJ1  1  12  8  8  OPEN  1*  1*  0.31  1*  0  0  Y   /

INJ1  1  13  8  8  OPEN  1*  1*  0.31  1*  0  0  Y   /

INJ1  1  14  8  8  OPEN  1*  1*  0.31  1*  0  0  Y   /

INJ1  1  15  8  8  OPEN  1*  1*  0.31  1*  0  0  Y   /

INJ1  1  16  8  8  OPEN  1*  1*  0.31  1*  0  0  Y   /

INJ1  1  17  8  8  OPEN  1*  1*  0.31  1*  0  0  Y   /

INJ1  1  18  8  8  OPEN  1*  1*  0.31  1*  0  0  Y   /

INJ1  1  19  8  8  OPEN  1*  1*  0.31  1*  0  0  Y   /
```

```
INJ1  1  20  8  8  OPEN  1*  1*  0.31  1*  0  0  Y   /

INJ1  1  21  8  8  OPEN  1*  1*  0.31  1*  0  0  Y   /

INJ1  1  22  8  8  OPEN  1*  1*  0.31  1*  0  0  Y   /

INJ1  1  23  8  8  OPEN  1*  1*  0.31  1*  0  0  Y   /

INJ1  1  24  8  8  OPEN  1*  1*  0.31  1*  0  0  Y   /

INJ1  1  25  8  8  OPEN  1*  1*  0.31  1*  0  0  Y   /

INJ1  1  26  8  8  OPEN  1*  1*  0.31  1*  0  0  Y   /

INJ1  1  27  8  8  OPEN  1*  1*  0.31  1*  0  0  Y   /

INJ1  1  28  8  8  OPEN  1*  1*  0.31  1*  0  0  Y   /

INJ1  1  29  8  8  OPEN  1*  1*  0.31  1*  0  0  Y   /

INJ1  1  30  8  8  OPEN  1*  1*  0.31  1*  0  0  Y   /

INJ1  1  31  8  8  OPEN  1*  1*  0.31  1*  0  0  Y   /

INJ1  1  32  8  8  OPEN  1*  1*  0.31  1*  0  0  Y   /

INJ1  1  33  8  8  OPEN  1*  1*  0.31  1*  0  0  Y   /

INJ1  1  34  8  8  OPEN  1*  1*  0.31  1*  0  0  Y   /

INJ1  1  35  8  8  OPEN  1*  1*  0.31  1*  0  0  Y   /

INJ1  1  36  8  8  OPEN  1*  1*  0.31  1*  0  0  Y   /

INJ1  1  37  8  8  OPEN  1*  1*  0.31  1*  0  0  Y   /

INJ1  1  38  8  8  OPEN  1*  1*  0.31  1*  0  0  Y   /

INJ1  1  39  8  8  OPEN  1*  1*  0.31  1*  0  0  Y   /

INJ1  1  40  8  8  OPEN  1*  1*  0.31  1*  0  0  Y   /

INJ1  1  41  8  8  OPEN  1*  1*  0.31  1*  0  0  Y   /
```

```
INJ1  1  42  8  8  OPEN  1*  1*  0.31  1*  0  0  Y   /
INJ1  1  43  8  8  OPEN  1*  1*  0.31  1*  0  0  Y   /
INJ1  1  44  8  8  OPEN  1*  1*  0.31  1*  0  0  Y   /
INJ1  1  45  8  8  OPEN  1*  1*  0.31  1*  0  0  Y   /
INJ1  1  46  8  8  OPEN  1*  1*  0.31  1*  0  0  Y   /
INJ1  1  47  8  8  OPEN  1*  1*  0.31  1*  0  0  Y   /
INJ1  1  48  8  8  OPEN  1*  1*  0.31  1*  0  0  Y   /
INJ1  1  49  8  8  OPEN  1*  1*  0.31  1*  0  0  Y   /
INJ1  1  50  8  8  OPEN  1*  1*  0.31  1*  0  0  Y   /
PROD1  307  1  8  8  OPEN  1*  1*  0.31  1*  0  0  Y   /
PROD1  307  2  8  8  OPEN  1*  1*  0.31  1*  0  0  Y   /
PROD1  307  3  8  8  OPEN  1*  1*  0.31  1*  0  0  Y   /
PROD1  307  4  8  8  OPEN  1*  1*  0.31  1*  0  0  Y   /
PROD1  307  5  8  8  OPEN  1*  1*  0.31  1*  0  0  Y   /
PROD1  307  6  8  8  OPEN  1*  1*  0.31  1*  0  0  Y   /
PROD1  307  7  8  8  OPEN  1*  1*  0.31  1*  0  0  Y   /
PROD1  307  8  8  8  OPEN  1*  1*  0.31  1*  0  0  Y   /
PROD1  307  9  8  8  OPEN  1*  1*  0.31  1*  0  0  Y   /
PROD1  307  10  8  8  OPEN  1*  1*  0.31  1*  0  0  Y   /
PROD1  307  11  8  8  OPEN  1*  1*  0.31  1*  0  0  Y   /
PROD1  307  12  8  8  OPEN  1*  1*  0.31  1*  0  0  Y   /
PROD1  307  13  8  8  OPEN  1*  1*  0.31  1*  0  0  Y   /
```

```
PROD1  307  14  8  8  OPEN  1*  1*  0.31  1*  0  0  Y   /

PROD1  307  15  8  8  OPEN  1*  1*  0.31  1*  0  0  Y   /

PROD1  307  16  8  8  OPEN  1*  1*  0.31  1*  0  0  Y   /

PROD1  307  17  8  8  OPEN  1*  1*  0.31  1*  0  0  Y   /

PROD1  307  18  8  8  OPEN  1*  1*  0.31  1*  0  0  Y   /

PROD1  307  19  8  8  OPEN  1*  1*  0.31  1*  0  0  Y   /

PROD1  307  20  8  8  OPEN  1*  1*  0.31  1*  0  0  Y   /

PROD1  307  21  8  8  OPEN  1*  1*  0.31  1*  0  0  Y   /

PROD1  307  22  8  8  OPEN  1*  1*  0.31  1*  0  0  Y   /

PROD1  307  23  8  8  OPEN  1*  1*  0.31  1*  0  0  Y   /

PROD1  307  24  8  8  OPEN  1*  1*  0.31  1*  0  0  Y   /

PROD1  307  25  8  8  OPEN  1*  1*  0.31  1*  0  0  Y   /

PROD1  307  26  8  8  OPEN  1*  1*  0.31  1*  0  0  Y   /

PROD1  307  27  8  8  OPEN  1*  1*  0.31  1*  0  0  Y   /

PROD1  307  28  8  8  OPEN  1*  1*  0.31  1*  0  0  Y   /

PROD1  307  29  8  8  OPEN  1*  1*  0.31  1*  0  0  Y   /

PROD1  307  30  8  8  OPEN  1*  1*  0.31  1*  0  0  Y   /

PROD1  307  31  8  8  OPEN  1*  1*  0.31  1*  0  0  Y   /

PROD1  307  32  8  8  OPEN  1*  1*  0.31  1*  0  0  Y   /

PROD1  307  33  8  8  OPEN  1*  1*  0.31  1*  0  0  Y   /

PROD1  307  34  8  8  OPEN  1*  1*  0.31  1*  0  0  Y   /

PROD1  307  35  8  8  OPEN  1*  1*  0.31  1*  0  0  Y   /
```

```
PROD1  307  36  8  8  OPEN  1*  1*  0.31  1*  0  0  Y   /
PROD1  307  37  8  8  OPEN  1*  1*  0.31  1*  0  0  Y   /
PROD1  307  38  8  8  OPEN  1*  1*  0.31  1*  0  0  Y   /
PROD1  307  39  8  8  OPEN  1*  1*  0.31  1*  0  0  Y   /
PROD1  307  40  8  8  OPEN  1*  1*  0.31  1*  0  0  Y   /
PROD1  307  41  8  8  OPEN  1*  1*  0.31  1*  0  0  Y   /
PROD1  307  42  8  8  OPEN  1*  1*  0.31  1*  0  0  Y   /
PROD1  307  43  8  8  OPEN  1*  1*  0.31  1*  0  0  Y   /
PROD1  307  44  8  8  OPEN  1*  1*  0.31  1*  0  0  Y   /
PROD1  307  45  8  8  OPEN  1*  1*  0.31  1*  0  0  Y   /
PROD1  307  46  8  8  OPEN  1*  1*  0.31  1*  0  0  Y   /
PROD1  307  47  8  8  OPEN  1*  1*  0.31  1*  0  0  Y   /
PROD1  307  48  8  8  OPEN  1*  1*  0.31  1*  0  0  Y   /
PROD1  307  49  8  8  OPEN  1*  1*  0.31  1*  0  0  Y   /
PROD1  307  50  8  8  OPEN  1*  1*  0.31  1*  0  0  Y   /
/
-- control data for production wells
WCONPROD
--wname open/shut ctrlmode orat wrat grat lrat rvol bhpmin thpmin vfptab artlift ...
PROD1    O      ORAT    3   1*    1*   300  1*    180    0       0      0 /
/
--open horizontal well producing oil at a rate of 300 Rm3/day.
```

```
-- ------------------------------------------------------------------------------------------------------------
-----------------

--Control data for injection wells

WCONINJE

--wname  type   open/shut ctrlmode orat wrat grat lrat rvol bhpmin thpmin vfptab artlift ...

INJ1   WATER   OPEN   RATE   50  1*  500  1*/

/

--open horizontal injector well producing oil at a rate of 500 Rm3/day.

-- Injection rate controls/limits for groups or field

GCONINJE

-- Group Phase CtrlMode RateTrg Rvoltrg ReinjTrg VoidReplFrac (VREP) N/A

FIELD   WAT  VREP     1*       1*       1*      1.0115/

/

--VREP is set to control total reservoir volume injection rate of the water phase.

--------------------------------------------------------------------------------------------------------------
-----------

--sets simulator control parametres

TUNING

-- Record 1: Time stepping controls

--TSINT  TSMAXZ      TSMINZ  TSMCHP  TSFMAX  TSFMIN  TSFCNV  TFDIFF

0.1  5  0.1/

/

--The value assigned involved a try and error process until timestep chopping ceases
```

```
--time chopping is caused by non-linear convergence failure

--I plotted TCPU and simulated time to access simulation stability

-- ---------------------------------------------------------------------------------------------------------------
----------

-- Record 2 is ignored and not applicable.

-- ---------------------------------------------------------------------------------------------------------------
----------

-- Record 3: Control of Newton and linear iterations

--NEWTMX  NEWTMIN    LITMAX  LITMIN  MXWSIT  MXWPIT  DDPLIM DDSLIM

25  1  58  1  30/

--increased NEWTMX from 25, LITMAX to 100 and decreased LITMIN to 1 from 10.

--The dates remained unchanged. I will modify them when we meet

--increase the number of dates



-- ---------------------------------------------------------------------------------------------------------------
----------

-- Dates at which reports are required.

DATES

1 JUL 2019  /

1 JAN 2020  /

1 JUL 2020  /

1 JAN 2021  /

1 JUL 2021  /
```

1 JAN 2022 /

1 JUL 2022 /

1 JAN 2023 /

1 JUL 2023 /

1 JAN 2024 /

1 JUL 2024 /

1 JAN 2025 /

1 JUL 2025 /

1 JAN 2026 /

1 JUL 2026 /

1 JAN 2027 /

1 JUL 2027 /

1 JAN 2028 /

1 JUL 2028 /

1 JAN 2029 /

1 JUL 2029 /

1 JAN 2030 /

1 JUL 2030 /

1 JAN 2031 /

1 JUL 2031 /

1 JAN 2032 /

1 JUL 2032 /

1 JAN 2033 /

1 JUL 2033 /

1 JAN 2034 /

1 JUL 2034 /

1 JAN 2035 /

1 JUL 2035 /

1 JAN 2036 /

1 JUL 2036 /

1 JAN 2037 /

1 JUL 2037 /

1 JAN 2038 /

1 JUL 2038 /

1 JAN 2039 /

1 JUL 2039 /

1 JAN 2040 /

1 JUL 2040 /

1 JAN 2041 /

1 JUL 2041 /

1 JAN 2042 /

1 JUL 2042 /

1 JAN 2043 /

1 JUL 2043 /

1 JAN 2044 /

1 JUL 2044 /

1 JAN 2045 /

1 JUL 2045 /

1 JAN 2046 /

1 JUL 2046 /

1 JAN 2047 /

1 JUL 2047 /

1 JAN 2048 /

1 JUL 2048 /

1 JAN 2049 /

1 JUL 2049 /

1 JAN 2050 /

1 JUL 2050 /

1 JAN 2051 /

1 JUL 2051 /

1 JAN 2052 /

1 JUL 2052 /

1 JAN 2053 /

1 JUL 2053 /

1 JAN 2054 /

1 JUL 2054 /

1 JAN 2055 /

1 JUL 2055 /

1 JAN 2056 /

1 JUL 2056 /

1 JAN 2057 /

1 JUL 2057 /

1 JAN 2058 /

1 JUL 2058 /

1 JAN 2059 /

1 JUL 2059 /

1 JAN 2060 /

1 JUL 2060 /

1 JAN 2061 /

1 JUL 2061 /

1 JAN 2062 /

1 JUL 2062 /

1 JAN 2063 /

1 JUL 2063 /

1 JAN 2064 /

1 JUL 2064 /

1 JAN 2065 /

1 JUL 2065 /

```
/

END
```